Politecnico di Torino

Master’s Degree in Biomedical Engineering
A.a. 2022/2023
Graduation Session July 2023

GLIOBLASTOMA MULTIFORME: NEW INSIGHTS ON ITS THREE-DIMENSIONAL *IN VITRO* MODELLING FOR A RELIABLE DRUG AND NANOMEDICINE SCREENING

Supervisors:	Candidate:
Prof. Gianluca Ciardelli	Sara Muccio
Prof. Clara Mattu	
Dott. Andrea Bezze	

Abstract

Glioblastoma multiforme (GBM) is the most common malignant, primary brain tumour with a median overall survival of only 15 months. The major challenges in treating GBM are the self-renewal capability of GBM cells and GBM stem cells (GSCs) which drive the development of treatment-resistant tumour variants; the heterogeneous composition, consisting of different cell types and of tumour cells at different stages of mutation; and the presence of the blood brain barrier (BBB), which acts as a protective boundary between the circulatory system and the brain parenchyma, hampering drug access to the central nervous systems (CNS). Therefore, treatment options for GBM are extremely limited, highlighting the need for newer and more efficient therapies able to address the above challenges. In this contest, nanomedicine-based therapies are extremely interesting as they have the potential to bypass the BBB, thereby extending drug accumulation in the CNS, and to efficiently target different cell populations composing the GBM microenvironment (TME). Unfortunately, nanomedicine require extensive testing, which is unfeasible with traditional animal models. Therefore, three-dimensional (3D) models of GBM representing a powerful and versatile alternative to animal testing, are needed for efficient validation of nanomedicine and, more in general, of other therapeutic options. The primary goal of this thesis was to develop and characterize different in vitro 3D GBM models, focusing on the preparation of multicellular tumour spheroids (MTS), and to apply them for the testing of core-shell drug-loaded nanoparticles (NPs). For this purpose, different cell lines were used, namely, GBM cells (U87-MG), GSCs (GBM-8), microglia (HMC3), and astrocytes (HASTR-ci35). MTS with different compositions were successfully obtained and used to test NPs loaded with the proteasome inhibitor, Bortezomib (BTZ), using the unencapsulated drug as control. Results confirmed that NPs treatment was overall less cytotoxic, proving the importance of the encapsulation of drug for a better targeting and for minimal adverse effects. Moreover, the inclusion of different cell lines provides better mimicry of the heterogenous cell composition of GBM TME resulting in chemoresistance. The invasion mechanism of GBM was studied by embedding MTS in two different hydrogels, simulating the extracellular matrix (ECM), to identify the effect of matrix stiffness on tumour invasion. Moreover, since the BBB is one of the main actors of the GBM progression, MTS of the BBB were successfully created, by mixing brain vascular endothelial cells (HBEC-5i), pericytes (HVBPC) and astrocytes. Lastly, the GBM model complexity was increased by adopting a microfluidic platform (OrganoPlate® Graft, MIMETAS), composed by a central chamber housing the MTS within an ECM gel and two lateral perfusion channels. The latter were seeded with HBEC-5i to mimic brain blood vessels. Thus, an in vitro brain capillary network was obtained with dense homogenous vessel and well-branched sprouts. Thanks to this, the infiltration capabilities of HMC3 and NPs towards the tumour mass in the host chamber was assessed. These promising results pave the way to the possibility of increasing the model complexity, for instance, by varying the properties of the hydrogel matrix or introducing 3D-bioprinting approaches. Moreover, the microfluidic model could be used to investigate nanocarrier- and cell-mediated transport through the BBB to ensure targeted and effective drug delivery.

List Of Figures

Table of Contents

1 Introduction

Glioblastoma multiforme (GBM) is one of the most lethal and aggressive human cancers; it is classified by the WHO (World Health Organization) as a grade IV glioma and is the most common malignant, primary brain tumour in adults, with a median overall survival of only 15 months. [1] GBM represents approximately 57% of all gliomas and 48% of all primary malignant central nervous system (CNS) tumours. [2] This tumour generally arises from the glial cells, astrocytes, which serve supporting roles within the nervous system. [3]

The most common symptoms of GBM include headaches, ataxia, vertigo, vision alterations and sometimes syncope. [4] Due to these unspecific symptoms, glioma is often misdiagnosed. [5]

GBM has been described as a low-metastatic tumour, mostly located in the supratentorial region (frontal, temporal parietal, and occipital lobes). [6] GBM is rarely located in the cerebellum and is very rare in the spinal cord, with different tumour behaviour found at these locations. Although tumour cells are already disseminated far in the surrounding parenchyma at time of diagnosis, it is generally a single mass, while true multifocal glioblastoma usually have distinct histological appearance and are most likely polyclonal, usually presenting as simultaneous infra and supratentorial masses. Most GBMs are intraparenchymal with an epicentre in the white matter, some are largely superficial, in contact with the leptomeninges and dura, but without invading the subarachnoid space. [7]

To date, the factors leading to GBM development are still unknown, although evidence indicates that exposure to ionizing radiation is strongly associated with an increased risk. [8]

The standard-of-care (SOC) treatment relies on maximal surgical resection, followed by chemotherapy (most commonly with Temozolomide - TMZ) and radiotherapy. Unfortunately, this approach is associated with side effects and tumour recurrence, resulting in an overall survival of less than 15 months. [2] Therefore GBM has become a crucial public health issue due to the high hospitalization cost and poor quality of life of patients. [8]

There are several factors that actively participate in the unfavourable outcome of this disease. Firstly, the DNA repair capabilities and self-renewing potential of glioblastoma cells and *glioma stem cells* (*GSCs*) are thought to be responsible for the development of resistance against all current available treatment modalities. [8] Moreover, GBM is also characterized by a highly heterogeneous cellular milieu, consisting not only in different types of cells, but also in cells at different stages of differentiation, a phenomenon referred to as “Intratumoural Heterogeneity”.[9]

To make matters worse, drug delivery to the CNS is hampered by the presence of the blood brain barrier (BBB), which acts as a protective barrier in between the circulatory system and the extracellular matrix of the nervous system. Another major challenge is represented by the immunosuppressive microenvironment, which is responsible for GBM classification a “cold tumour”. [10]

Therefore, there is a strong need for better treatment modalities for this tumour and of faster and reliable strategies for their screening, testing, and validation. In this scenario, the availability of reliable systems that reproduce the GBM microenvironment and its development *in vitro* is expected to be groundbreaking, as it will allow the design of newer and more efficient therapies, virtually patient-specific, shading light on the molecular mechanisms leading to invasion and development of drug resistance in GBM.

1.1 Genetic GBM classification

In 95% of cases, GBM arises *de novo* as primary GBM, but may also develop from preexisting low-grade astrocytomas, as secondary GBM, in 5% of cases, largely in the pro-neural subgroup. [11] Indeed, primary (*pGBM*) and secondary (*sGBM*) glioblastomas develop through different genetic pathways but are histologically similar, showing the morphological criteria of anaplasia, astrocytic tumour cells, prominent microvascular proliferation, and necrosis. [12] The pGBM is generally associated with elderly patients, with an overall higher occurrence, while sGBM generally presents in younger patients, it's rarer and linked to a more favourable prognosis. pGBM is characterized by an overexpression or amplification of the Endothelial Growth Factor Receptor (EGFR), loss of heterozygosity (LOH), and mutations in 10q, p16INK4A and phosphate and tensin homolog (PTEN). While secondary GBM shows mutations in protein 53 (TP53), not common in pGBM. Another crucial classification criterion is mutation of *IDH1 gene*, which is generally found in secondary GBM. This mutation is also preferentially found in tumours harbouring TP53 mutations.

Using transcriptional profiling data, The Cancer Genome Atlas (TCGA) was able to provide a molecular GBM classification into four subgroups, named as classical, neural, pro-neural and mesenchymal, classification which is strictly linked to a different prognostic outcome. [13]

For what concerns **Classical subtype**, high level of EGFR amplification is observed, infrequent in other subtypes, as well as loss of heterozygosity in chromosome 10 (LOH10). EGFR can activate pathways essential for GBM cells to flourish, such as the receptor tyrosine kinase/Ras/phosphoinositide3-kinase (RTK/RAS/PI3K) pathways. [14] EGFR can also be altered; in particular, EGFRvIII mutation is associated with lower survival. [15] This can be explained by the fact that one of the proposed mechanisms of tumorigenesis, due to EGFR activation (EGFRvIII), is the remodelling of the landscape of GBM tumour cells through activation of pathways such as FOXG1 and SOX9, other than the commonly observed RTK/RAS/PI3K pathway. [16] In tandem with high rates of EGFR alteration, there is a distinct lack of TP53 mutations, even though TP53 is the most frequently mutated gene in GBM. Finally, another common biomarker is the chromosome 7 amplification which is, generally expressed in all GBMs, but with a much higher rate here. [17]

The **Neural subtype** is heavily associated with TP53 mutation, EGFR amplification and CDKN2A gene deletion. [18]

The **Pro-neural subtype** relies in the amplification of platelet-derived growth factor alpha receptor (PDGFRA), resulting in abnormal and uncontrolled cell growth. [19]. [[19] Also, mutated IDH1 is abundant, and this explains why sGBM are only of the pro-neural subtype. Moreover, a high expression of OLIG2, responsible for the down regulation of the tumour suppressor gene p21, is observed. [20]

The **Mesenchymal subtype** presents focal hemizygous deletions (or lower lever of expression) of the gene NF1, a tumour suppressor gene. Moreover, high expression of chitinases 3 and1, as well as MET predominantly occurs in the mesenchymal subtype. [21]

1.2 Morphological features of GBM

Morphologically, GBM consists of polymorphic and anaplastic small cells. Cells are polygonal to spindle-shaped with acidophilic cytoplasm and indistinct cellular borders. Their nuclei are oval or elongated with multiple distinct nucleoli located centrally or peri-centrally. Multinucleated cells, as well as neutrophils, macrophages, and necrotic cells, can be also recognized. [22]

Another important feature is that vascularization of GBM is extremely high. [23] Vessels are characterized by endothelial cells which are phenotypically different from regular endothelial cells since they are overlapped and heterogenous in size and shape.[24]

Necrotic foci are another typical morphological feature of GBM, which differs depending on the site and size of the necrotic area. One consists of large zones of necrosis within the centre of the tumour, probably due to an insufficient blood supply in all primary GBM, while the other one consists of small necrotic foci surrounded by pseudopalisading areas. These areas are formed by radially oriented glial cells, observed in both primary and secondary GBM. [25]

Pseudopalisades can range from dozens to thousands of µm in the internal diameter and can be classified into three main types. The small ones are less than hundreds of µm wide with hypercellular zones surrounding internal fibrillarity. Medium ones show central necrosis and single dying cells but are characterized from having a peripheral zone of fibrillarity inside the pseudopalisades. Last, the largest ones have extended necrotic zones with central vessels. The cell population found in pseudopalisades may be represent by proliferating neoplastic cells that out-grow their blood supply and suffered central necrosis, which are resistant to apoptosis, as well as tumour and inflammatory cells adjacent to necrotic areas. [26].

1.3 The Tumour microenvironment and its role in GBM progression.

The behaviour of a tumour, as well as its progression, does not only rely on the tumour cells, e.g., the highly proliferative cells and GSCs, but depends on the synergistic action of several factors and cellular components, collectively identified as the Tumour Microenvironment (TME). [27] Soluble mediators (such as cytokines), or extracellular matrix (ECM) components (e.g., collagen, glycoproteins), tumour-resident cell types (e.g., neurons, astrocytes, endothelial cells, pericytes), as well as resident immune cells (e.g., microglia), all comprise the GBM microenvironment. These components influence and determine the proliferation, invasion, and reaction of the tumour to treatments.

These continue interdependent interactions, also include a continual struggle between the growing tumour and the host immune system.

As stated before, GBM is considered a "*cold tumour*" due to its high immunosuppressive TME, where "cold tumour" refers to the lack of T-cell infiltrate within the TME as well as the reduced response to immunotherapy. [28] Recent discoveries showed that a lymphatic vasculature is present in the brain, and that pathological stimuli, such as tumour growth, may induce changes in the permeability of the BBB. As a result, immune infiltrate of T lymphocytes, dendritic cells, natural killer (NK) cells, and microglia/macrophages can be found in brain tumours, suggesting that these cells may be exploited to induce tumour-specific immune responses. [29]

Despite the presence of this immune infiltrate, a highly immunosuppressive tumour microenvironment is present in GBM, which explains the high recurrence rate and immune escape ability of this tumour. Immunosuppression in GBM is achieved by:

- ✓ secretion of immunosuppressive factors, like cytokine, chemokines, growth factors (to mention a few, IL-6, IL-10, IL-1, TGF-β, prostaglandin E2, bFGF) by tumour cells and microglia. [30]

✓ recruiting of different immunosuppressive inflammatory cells to the TME. The concurrent result of these mechanisms leads to suppressing NK activity and T-cell activation and proliferation, inducing T-cell apoptosis. [31]

✓ expression of immunosuppressive cell-surface factors or programmed cell death protein-1 ligand (PD-L1). [32]

Therefore, understanding the role of the immune system and its interaction with the different molecular subtypes of GBM, is a major knowledge gap which needs to be filled to drive rational design of more efficient therapies against this tumour. [33]

To summarize, the GBM microenvironment contains a large variety of cell types (**Figure 1**), such as:

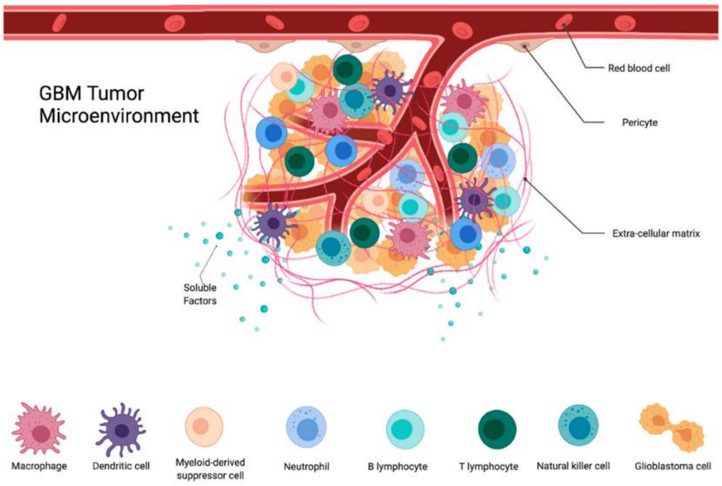

Figure 1: Visual schematization of GBM tumour microenvironment and its components. Image extrapolated from an article by Dapash et all. [34].

- Immune cells:
    - *myeloid cells:* such as tumour-associated macrophages (TAMs)—resident microglia and bone marrow-derived macrophages (BMDMs), dendritic cells (DCs), neutrophils/tumour-associated neutrophils (TANs).
    - *lymphoid cells—T cells*: such as, for instance, CD8+ cytotoxic T cells, CD4+ helper T (Th) cells, and regulatory T cells (T-regs).
- Non-immune cells: these are mainly tissue-resident cells, such as neurons, astrocytes, endothelial cells, and pericytes.
- Tumour cells and glioma stem cells (GSCs). [30]

GBM-associated microglia and macrophages (GAMMs)

A major role in GBM heterogeneity is played by microglia and macrophages. These cells tend to accumulate within and around the tumour mass. GAMMs present considerable diversity and plasticity, and display a unique phenotype, only partially ascribable to inflammatory (M1) or alternative (M2) polarization expression patterns [53]. In fact, these types of cells alter inflammation, by secreting TGF β1 and interleukin 10 (IL-10), induce angiogenesis through vascular endothelial growth factor (VEGF), and matrix metalloproteases (MP); and induce the production of some pro-inflammatory molecules, such as IL-1, tumour necrosis factor, IL-6, and IL-12). [29]

Myeloid-Derived Suppressor Cells

Myeloid-derived suppressor cells (MDSCs) are a heterogeneous group of cells defined by their myeloid lineage, immature state, and the ability to potently suppress T-cell responses. MDSCs contribute to tumour immune evasion in different ways, such as suppressing the first-line defence, by inhibiting the NK cell activation receptor *NKG2D* and preventing *IFNγ* production by NK cells in the presence of TGF-β. [29]

MDSCs decrease immune response by reducing the antitumour activity of cytotoxic T cell [80], suppressing NK cells [81], suppressing macrophage and dendritic cell function, and inducing production of Tregs (regulatory T cells) and B-regs (regulatory B cells). In MDSCs exposed to hypoxia, an up-regulation of CD45 tyrosine phosphatase activity and a down-regulation of STAT3 transcription factor activity was reported, a fact which facilitates the differentiation of MDSCs into TAMs [84]. MDCSs promote tumour growth by favouring angiogenesis and vasculo-genesis and correlate with poor outcomes in patients with solid tumours. It was recently shown that MDSCs within brain tumours undergo upregulation of *transmembrane protein programmed death ligand 1* (PD-L1), while tumour-derived CD4+ T cells express high levels of PD-1. The PD-1/PD-L1 interaction results in T-cell exhaustion, inhibiting antitumor immune responses.

1.3.1 Cancer stem cells in GBM

Tumour maintenance and progression, as well as resistance to therapies and the ability of self-renewal, are attributable to a small subpopulation of cells: GBM stem cells (GSCs) or Cancer stem cells (CSCs), which are phenotypically different from cancer cells, sharing functional similarities with normal Neural Stem cells (NSCs). It is known that GSCs express many of the characteristic markers of NSCs, including CD133, SOX2, and Nestin. Despite this similarity, it is still unclear whether GSCs originate from mutated NSCs or if they derive from mature glial cells that gained a self-renew ability. [27]

CD133, a transmembrane glycoprotein, is the most widely recognized and reliable stemness biomarker. CD133-positive cells show higher resistance to radiation and chemotherapy, a reduced level of apoptosis, and an increased colony-forming efficiency when compared to CD133-negative cells. Other factors may collaborate with CD133 to increase stemness of GSCs, for instance experimental evidence demonstrated that *SOX2* expression contributes to GBM stem-cell potency by regulating CD133 levels in CD133-positive GBM cells. Increased levels of Nestin expression are found in higher-grade gliomas and in patients with lower survival rates. Nevertheless, the quest for a universal GSC marker is still open.

GSCs are placed in a specific microenvironment referred as to the "tumour niche", where their stemness can be maintained. The cell composition of these niches varies greatly, making them look morphologically distinct from each other (**Figure 2**). [35]

A niche, to be considered such, must respect two main characteristics: the presence of GCSs and their direct contact with endothelial cells (ECs), since the presence of a brain vessel is another fundamental feature. These characteristics are only fully respected by the perivascular niches, however, in a broader sense, the definition can be applied to perinecrotic niches. [36]

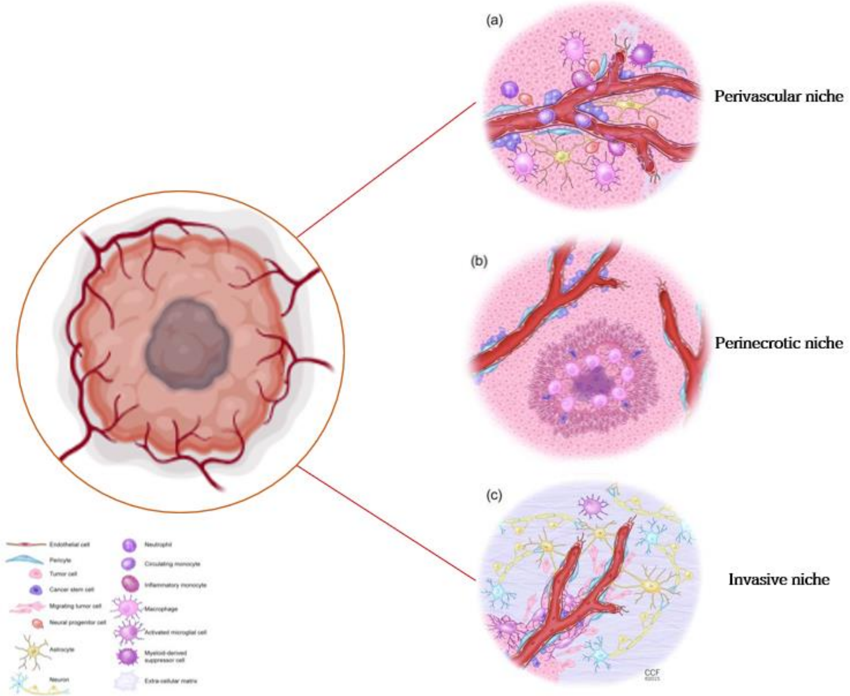

Figure 2: Illustrations of the different Glioblastoma (GBM) niches, reworked from "Glioblastoma: Defining Tumour Niches". [37] (a) The perivascular GBM niche. (b) The perinecrotic/hypoxic GBM niche. (c) The invasive GBM niche.

The *perivascular niches* are represented by zones in which ECs of capillaries or arterioles are in strict contact with stem cells. According to this definition, larger vessels with defined layers cannot be described as niches, since ECs are not in strict contact with GSCs. [36] This type of niches drastically influences the behaviour of resident GSCs. Indeed, ECs can interact specifically with nestin-CD133-positive GSCs located in the proximity of capillaries and produce a variety of growth factors participating in the maintenance of GSC self-renewing and undifferentiated state. GSCs, in turn, produce VEGF and a variety of cytokines and chemokines, some of which are known to activate ECs, suggesting that GSCs may regulate tumour angiogenesis (**Figure 2**). [29]

The perinecrotic (also named hypoxic) niches are characterized by the occurrence of GSCs around necrotic foci, surrounded by a row of hypoxic palisading tumour cells, induced by hypoxia-inducible factor (HIF)-1/2 activated by hypoxia. In these areas, necrosis develops as consequence of imbalance between the high proliferation rate of tumour cells and the low proliferation rate of ECs. Hypoxia triggers different signalling pathways that influence GSCs self-renewal, proliferation, and invasion. Moreover, drug resistance is also induced by hypoxia through the attenuation of mismatch repair genes and activation of Multidrug Resistance gene 1 (MDR1), which encodes for P-glycoprotein (**Figure 2**). [35]

The *invasive niches* on the other hand are mainly found in infiltration and invasive areas of the tumour. In these areas tumour cells generally infiltrates normal tissue as single cells and grow besides the basal lamina of vessels. [36] In addition, recent studies showed that GSCs may transdifferentiate into ECs or pericytes, creating their own vascular niches (Figure 2**)**. [38]

1.4 The importance of the healthy BBB and brain tumour-induced BBB remodelling

Another major challenge when treating brain tumours is the presence of the Blood Brain Barrier (BBB). The BBB is composed a continuous capillary endothelium with tight junctions (TJs) between cells and an intact basement membrane, pericytes, microglia, and glial membrane, which is surrounded by astrocytes. The BBB differs from the other endothelial tissues in the human body because ECs are overlapped, forming a tightly connected structure, displaying up-regulated expression of junctional proteins, reduced paracellular and transcellular transport, [39] and absence of fenestrations. [40] The BBB is surrounded by a basement membrane, containing astrocytes on its outer surface [40]

As already mentioned, besides ECs, that are several leading actors, contributing to the correct functioning of the BBB.

Pericytes, which are localized along capillaries, play a crucial role in maintaining the correct physical structure of the barrier. Their localization between ECs and astrocytes, make them dynamically and synergistically interactive with adjacent cells to maintain homeostasis, such as regulating blood flow. [41]

Astrocytes are the most abundant cell type in the brain; they are metabolic sensors and play an integral role in BBB development and function. Astrocytes encircle their end-feet to cover the majority of the abluminal surface area of the BBB and regulate signalling pathways that maintain junctional complexes and produce additional basal lamina. By connecting via gap junctions and TJs, astrocytes can form an additional barrier in the CNS called the glia limitans. [42] ,[41]

Microglia represents the majority of innate immune cells in the brain parenchyma and contribute to early vasculogenesis in the brain. Microglia activation can cause BBB disruption or repair. Indeed, during inflammation, microglia and other immune cells can increase BBB permeability through interleukin-1β (IL-1β) secretion. [42] However, these same features that are essential to protect the brain, also hinder the delivery of systemic therapies to brain tumours, therefore resulting in one of the main causes for the failure of current therapies.

During the tumour progression, the BBB is partly disrupted and is often referred to as the blood–tumour barrier (BTB) [43]. Tumour vessels often display an irregular basal lamina, high permeability, larger diameter, as well as an abnormal distribution throughout the tumour mass. This dysfunctional brain vasculature is essential for gliomagenesis [43].

Nevertheless, changes in BBB happen slowly and the early phases of tumour genesis are not characterized by visible disruption of the BBB. [44] [45] As a highly invasive tumour, GBM, metastasizes along other existing brain structures, such as blood vessels, meninges, and white matter tracks. Before the angiogenesis phase starts, GBM cells will surround the vessels by invasion mechanisms, invading also outer space. This phenomenon blocks the interaction between the end-feet of astrocytes and the ECs, leading to the breakdown of the BBB. [43] This is also accompanied by the degradation of the basement membrane and the loss of the TJs, resulting in serum leakage into the parenchyma. This behaviour also leads to hypoxia and necrosis, which are two phenomena related to GBM progression. Indeed, both hypoxia and necrosis activate the secretion of growth factors, such as VEGF, BFGF, IL-8 and stromal cell-derived factor-1 (SDF1), which all together participate in the stimulation of the angiogenesis processes. GBM therefore creates its own dysfunctional vasculature network, which in turn results in reduce oxygen pressure and increased interstitial fluid pressure in the microenvironment, leading to increased patient morbidity and mortality. [40]

1.5 The ECM of GBM differs from normal brain ECM.

The brain ECM, which makes up for about 20% of all brain volume, can be considered as a complex network, mainly composed by a structural organization of GAGs (glycosaminoglycans), including hyaluronic acid (HA), proteoglycans, and glycoproteins (such as tenascins), all organized in a tissue specific manner. The role of collagen is restricted to blood vessels and the glia limitans. [46] The limited amount of fibrillary collage, as well as other matrix components gives a softer consistency to the brain, compared to other organs. [47]

However, the composition of ECM changes in gliomas. [46]; in particular, the ECM can influence the way cancer cells become aggressive and invasive.

Basically, all common components of ECM, comprising proteoglycans and proteins (laminin, tenascins, and fibronectin and collagens (I, II and IV)) have a supporting role in GBM [9]. In turn, glioma cells overexpress ECM components, such as HA, brevican, tenascins, and fibronectin. GBM cells also overexpress specific integrins and other receptors, which can interact with ECM components, promoting adhesion and migration through a two-way communication. [46]

One of the main differences that can be noticed in GBM ECM is an increase of HA levels, which is strictly correlated with tumour progression. In turn, HA with fibronectin can promote the mobility and invasiveness of glioma cells, through its two cellular receptors, CD44 and RHAMM.[48] Moreover, HA also stimulates the expression of several other molecules related to migration, such as CD44, Pgp-1, phagocytic glycoprotein-1, PTEN (phosphatase and tensin homolog) and MMPs (matrix metalloproteinases). [49] Another important role is played by Tenascin-C, which is thought to be involved in angiogenesis, therefore making it a potential target for anti-angiogenic therapies. [48]

As previously mentioned, GBM can induce the synthesis of proteins (such as proteases) that degrade the ECM, thereby extending the invasive front of the tumour. [49] In GBM TME, metalloproteinases (especially MMP-2 and MMP-9) are critical for cell invasion. [49] However, glioma cells are not the only source of proteases in the tumour, since also endothelial cells in GBM are responsible for a part of the extracellular matrix-degrading activity. [49]

Similarly, GBM cells can induce the expression of ECM components in the proximity of the tumour mass. This results in reduced nutrients and oxygen, causing hypoxic zones and metabolic stress and leading to GBM resistance to therapies. [46]

Integrins also play a role in ECM remodelling[48] In GBM, integrin α6 (a receptor for the ECM protein laminin) is overexpressed. This overexpression can regulate GSC distributions and maintenance. Another example is represented by integrin α3, also highly expressed by glioma CSCs, which can interact with fibronectin and laminin. It is generally localized in the GBM niches, and its role is to promote glioma invasion via ERK pathway. Integrin α7 has been correlated with negative outcome of the disease. Its major role is thought to be related to tumour growth and spreading via AKT. [50] Furthermore, integrins present at the edge of cells induce the recruitment of surface proteases, which can in turn degrade the ECM, therefore leading to migration into the newly created space. [48]

Recent studies highlighted the role of the mechanical properties of ECM in tumour progression. Indeed, the mechanotransduction can trigger several biochemical pathways, including cell mitosis, cytoskeleton contraction, and cell motility. [51] [52] Indeed, cell shape and size can be influenced by a process known as *Physical Compaction* in which cells gather and pack together, causing subsequent changes in expression and structure of collagen, which may contribute to tumour angiogenesis and GBM progression. Indeed, compaction of GBM cells changes collagen expression and structure, resulting in increased VEGF expression in vitro. [52]

ECM composition affects the stiffness of the matrix [50], therefore, it is not surprising that GBM matrix is progressively stiffer when compared to non-tumour brain ECM. On rigid ECMs, tumour cells can spread freely, forming prominent stress fibres and mature focal adhesions, and migrate rapidly. Likewise, cell proliferation is also strongly dependent on ECM rigidity, with cells proliferating much more rapidly on rigid ECM. [53]

Indeed, on average, normal brain stiffness is lower than 200 Pa while glioma stiffness increases with GBM progression, ranging from 100 to 10,000 Pa. These differences in tumour stiffness are due to overexpression of collagen IV and HA. [50],

2 In vitro GBM models: current state of the art

Over the past years a vast set of methodologies have been used in the study of GBM. [54]

As stated above, GBM is an extremely complex tumour, where intra-tumoral heterogeneity, composition of the TME, structure and mechanical properties of the ECM, all contribute to tumour development, dissemination, and response to treatment. These complex interactions are still not fully understood, and extensive investigation is still needed to shed light on the mechanisms leading to GBM aggressiveness. Unfortunately, the available technologies and models, still fail to fully recapitulate all the key features of GBM, hampering successful in vitro screening of newly developed drugs which mostly end up in unsuccessful outcome when translated to the *in vivo* trials.

In this scenario, reliable systems that truly reproduce the GBM microenvironment and its development *in vitro* are expected to be groundbreaking, as they will allow the design of newer and more efficient therapies, virtually patient-specific, shading light on the molecular mechanisms leading to invasion and development of drug resistance in GBM. In this optic, nanomedicine treatments may represent a powerful tool, because of their capabilities of active targeting.

To truly understand and predict how drug transport takes places across the BBB, these new predictive *in vitro* models, must include an accurate mimic of the human BBB and its function, given the fundamental role of this barrier in GBM. This section describes the available technologies and methodologies commonly adopted for the modelling of GBM, including innovative strategies that may pave the way for personalized medicine.

The first and simpler models are the 2D-cultures of cells, which can be composed by single or multi-cells. This type of experimental platform is compatible with all traditional assays but is poorly informative because of as the non-physiological cell signalling, drug response, and phenotype, due to their total lack of a 3D-*in vivo* like environment, both in terms of composition and mechanical properties. [55]

3D models can be engineered to achieve a three-dimensional environment, including different cell types, to reproduce the physiological fluid exchange, etc. In general, these models (summarized in **Figure 3**) can be divided in:

- *Spheroids*, which comprises cell aggregates, neurospheres (tumourspheres), multicellular tumour spheroids, organotypic multicellular spheroids and organoids.
- *Scaffolds,* in which cells are embedded in a hydrogel matrix.
- Microfluidic Devices/ Organ-on-a-chip. [50]

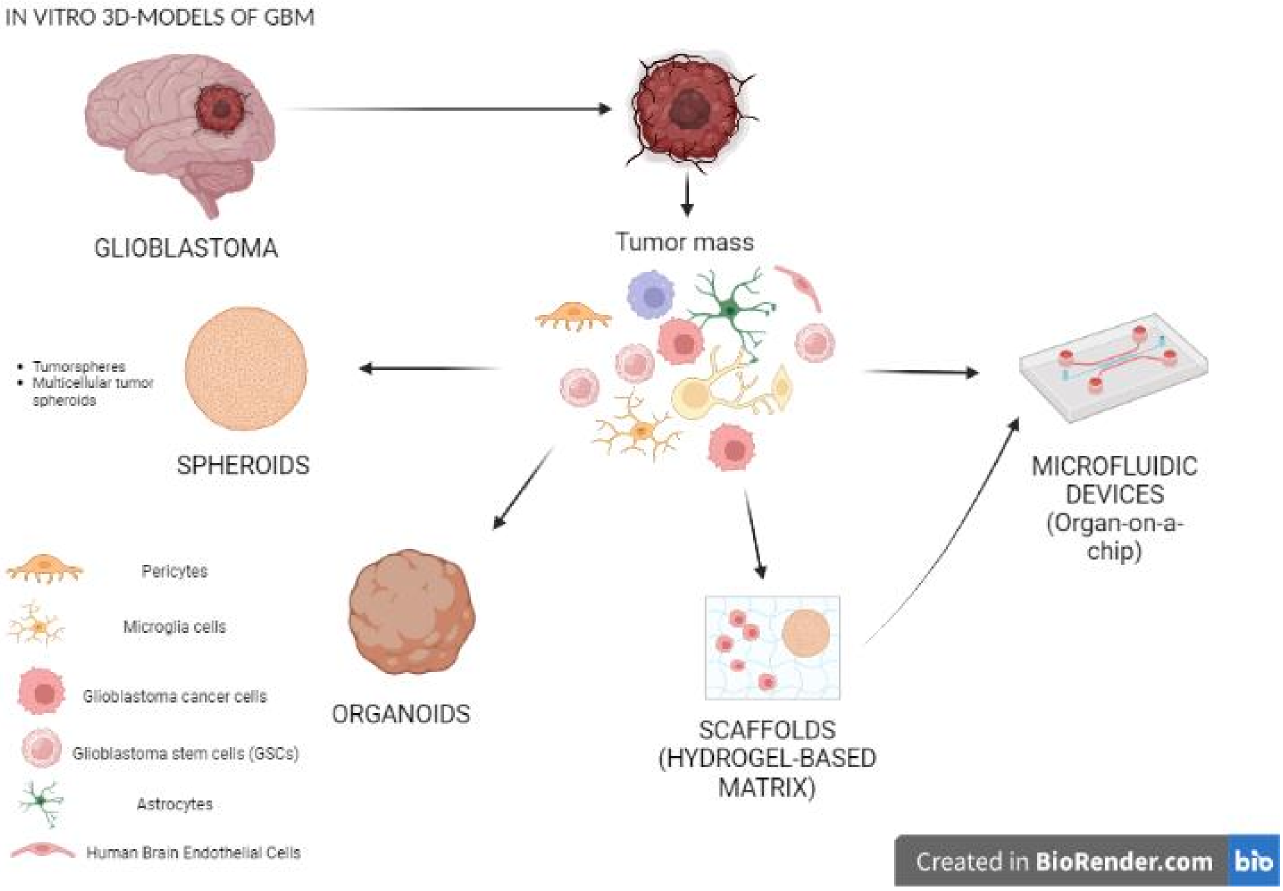

Figure 3: Schematic representations of in vitro 3D models suitable for GBM mimicking. Created with BioRender.com

2.1 2D models and their limitations

In standard 2D cultures, cells are usually layered on a rigid plastic substrate, such as culture flask or a petri dish, where they are maintained in a medium supplemented with ECM proteins. In similar models, cells are deposited on an ECM mixture or laminin/gelatin/collagen coated substrate until their growth in a confluent monolayer. [56]

This type of culture is useful when it comes to monitoring cell morphology, acquiring different types of imaging, performing antibody staining, and running functional assays. [57]

To date, 2D cultures are the fastest way to obtain preliminary results and test or screen drugs.

Standard 2D cultures can be modified to better represent some GBM features. For example, GBM cells have been cocultured with different cell types, such as astrocytes [58] or endothelial cells to stimulate malignant phenotypes.[59]

One of the commonly used methodologies to establish cocultures is by using transwells, in which cells are separated by a semi-permeable membrane. This membrane can allow direct contact to signalling factors secreted by separated cell populations. Results using these coculture systems have confirmed that supporting cells are extremely capable of guiding the behaviour of tumour cells.[58]

For instance, Leite et all [60], established a 2D co-culture including different ratios of U87-GBM (human glioblastoma cells) and microglial cells (MG), followed by a 3D culture in a hyaluronic acid hydrogel to mimic the GBM microenvironment. Co-cultures were treated with drugs, such as Temozolomide (TMZ), clomipramine (CLM), and Vincristine (VCR)). Interestingly, the GBM cells growing in close contact with MG revealed a modest increase in proliferation but revealed a greater migration. On the other hand, when GBM cells were treated with cytotoxic agents, they showed an increase in proliferation. These studies demonstrated that even a low amount of MG (10%-20%) was able to confer resistance of GBM to cytotoxins.

Similarly, in another study, a co-culture was created using human astrocytes in combination with GBM cells to investigate the protective mechanisms of astrocytes. In response to TMZ and VCR, glioma cell apoptosis induced by these drugs was reduced in the presence of astrocytes. [61]

2D cell cultures have been extensively used and have been fundamental to understand GBM biology [62]. Nevertheless, 2D cell culture has intrinsic limitations, such as the absence of physiological gradients, different cell density, unphysiological oxygen levels, lack of interaction with ECM, which all play major roles in tumour progression, as well as disruption of the original spatial context, and lack of other non-tumour cells present in the GBM microenvironment. [63]

In addition, repetitive cell passages only select cells with the highest proliferative potential, therefore leading to a decrease in the genetic heterogeneity e, characteristic of the tumour. Presumably, this selection results in accumulation of chromosomal aberrations and phenotypic alterations in cell lines [64], thus complicating the already complicated landscape of glioma genotype. Another fundamental aspect to consider, when developing a reliable model of GBM is its immunosuppressive environment, which comprises different immune system components that contribute to the definition of “cold tumour” and that totally lack in 2D cultures. [65]

2.2 Three-dimensional models: from spherical models to microfluidic devices

Three-dimensional (3D) models, derived completely from patient tissues or incorporating biomaterials, are a new, powerful, and versatile, tool to recapitulate TME dynamics, therefore leading to more predictive drug screening. [50]
3D models can be divided into three classes:

- Spheroid models
- Scaffolds (with particular attention to hydrogel-based matrix)
- Microfluidic Devices

2.2.1 Spheroid Models

Cell Aggregates

Aggregates are spherical models, in which cells have a less compact arrangement as compared to traditional spheroids. Therefore, their spatial configuration does not reproduce the cell-cell and cell-matrix interactions. [66]

Tumorspheres

These models are formed by proliferation of single-cell suspension of GSC (glioma stem cells), which can come from tumour samples (tissue-derived) or from established cancer cell lines. Cells are grown as free-floating spheres under low-attachment conditions in a serum-free (no FBS, Fetal Bovine Serum) medium, often enriched with EGF (Epidermal Growth factor)/bFGF (fibroblast growth factor), which are stem cell medium factors. These conditions are chosen to maintain the GSC population, in terms of genotypic and phenotypic features of the original tumour. [67] Moreover, inhibition of adhesion induces death of non-tumoral, differentiated cells. Under these conditions, undifferentiated tumour cells proliferate and grow as floating clusters termed tumourspheres. [68]

Multicellular Tumour Spheroids (MCTS)

Spheroids are generally formed by heterogenous aggregates of different cell types, which are not attached to any surface for support. [69]

MCTS, also referred to as tumour spheroids, grow from an aggregation of single-cell suspension from established cancer cell lines. Sometimes they can also come from single-cell suspension of tissue-derived cancer cells. Otherwise, when spheroids are composed of different types of cells, they are referred to as Heterotypic MCTS which can include both, cancerous and not cancerous, cells. They are typically cultured in a serum supplemented medium, with no additional growth factors. Typically, they are grown in non-adhesive well plates, dishes of flasks, to promote aggregation of cells. [68]

One of the most important features of these models is their intrinsic capability to recreate a physiologically relevant spatial configuration of GBM, as well as the possibility to fine-tune their composition, thereby providing a more realistic drug screening platform. [70] Indeed, spheroids have largely been used in cancer research because they are able to maintain gene expression and genomic patterns similarly to the original tumour. Their architecture allows the study of reciprocal relationships and mechanisms of interaction among GSCs and the other different cell types in the ITH of the TME, such as immune, stromal, and endothelial cells. [71] Moreover, the presence of hypoxic and necrotic regions can be replicated. Indeed, limited diffusion within the spheroids leads to the formation of three different areas: i) the outer part characterized by proliferating cells that are freely exposed to oxygen, nutrients, and signals; ii) the necrotic zone, characterized by lack nutrients and oxygen; and iii) a quiescent zone between the two. These layers are all present in physiological conditions. [72]

Several different protocols can be found to create spheroids, such as the *hanging drop method*, the *use non-adherent well-plates*, and *dynamic methods*. [70]

All the above methods are based on the principle that spheroid formation proceeds through two main phases. First, single cells form loose cellular aggregates, followed by an up-regulation of cell–cell adhesion molecules (e.g., E-cadherins) that result in the formation of cohesive cellular aggregates. During this process, cells also produce and organize their own 3D ECM, creating a completely endogenous matrix. [73] Citated methods are represented in **Figure 4.**

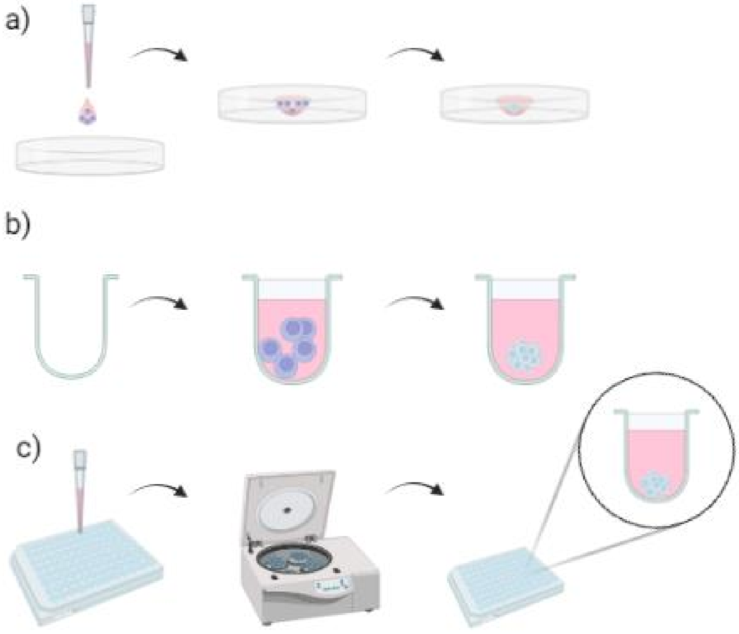

Figure 4: 3D GBM MCTS formation methods. a) Visual representation of the step needed for the Hanging Drop method. b) Visual representation of the steps needed for the non-adherent surface method, generally performed using a U-Shaped-Bottom 96-wells plate. c) Visual representation of the needed steps for the Dynamic Centrifugation Method. Created in BioRender.com

One of the major advantages of these models is the possibility to maintain the spheroids for a longer period of investigation, thus allowing a long-term and high throughput monitoring of treatments, as well as the study of tumour progression, invasion, and angiogenesis. [68]

Indeed, it has been reported that in spheroid configuration, U87-MG cells were able to upregulate stem cell markers. This is particularly important, since GSCs are responsible for drug resistance and their presence ensured a more reliable evaluation of drug efficacy *in vitro*. [74]

Other reports have shown that the inclusion of different cell types also allows to maintain the expression of stemness markers in GBM. For instance, multicellular spheroids were used to analyse how drug treatment would impact stemness of GBM cells. [75] To do so, co- and tri-culture MCTS were created using U87-MG GBM cells, astrocytes and/or endothelial cells. Once spheroids were mature, after 7 days, 5uM of lonafarnib (LNF), 100 µM of temozolomide (TMZ) or the combination of both were administered to spheroids. The authors showed that, 48-hour post treatment with LNF alone or in combination with TMZ, the size of spheroids significantly decreased, in co-culture with astrocytes. On the other hand, spheroids treated with TMZ did not show a significant decrease in size or cell viability. Co-culture with ECs resulted in higher sensitivity of the MCTS, also to TMZ alone. The GBM-astrocytes-EC triculture (obtained with a ratio of 1:4:9) showed the same reduction in size after 48h of LNF of around 1.1-fold compared to the untreated control. Similarly, 48h post TMZ treatment, the reduction was the same. For the combinational treatment, a slightly higher decrease in tumour size was noticed, reaching the 1.2-fold, compared to the untreated control. As well, the expression of stemness markers, such as NESTIN, SOX2, CD133, NANOG, and OCT4- significantly increased in response to LNF + TMZ treatment in all conditions (GBM-astrocytes, GBM-EC and triculture MCTS). In particular, the expression of some of these markers significantly increased after TMZ treatment, especially in GBM-EC and triculture MCTS. This work further confirmed the importance of including GSCs in models of drug screening, due to their implication in drug resistance.[75]

In another study, gene expression patterns of GBM spheroids were analysed, and compared to 2D adherent cells, for different cell lines. Some of the representative GSC markers, such as PDGFRA, SOX2, and NANOG, CD44, ECM markers, chemokines, chemokine receptors, NK cell activation receptor ligands and NK cell inhibitory receptor ligands were analysed. Results showed that SOX2, ECM markers, COL4A6, LUM, MMP16, and SNED1 was upregulated in the spheroid culture as compared to 2D conditions. [76] In other words, results indicated enhanced cell–cell physical interaction. The authors claimed that these findings are consistent with the fact that spheroids show enhanced production of tumour ECM proteins, in comparison with 2D culture. [77] Spheroid models also displayed resistance to anticancer drugs, similarly to *in vivo* observations. Upregulation of chemokines and their receptors was reported in 3D cultures. This is a promising finding, since it seems to replicate the [79] the CCL2–CCR2 axis, which is known to promote tumour progression by recruiting suppressive myeloid-derived suppressor cells. [78]

Sarisozen et al. [79] developed 3D MCTSs of GBM to test a co-delivery platform of a chemotherapeutic agent (doxorubicin) and a multidrug resistance modulator (curcumin) incorporated into 1,2-dioleoyl-sn-glycero-3-phosphoethanolamine (DOPE), 1,2-distearoyl-sn-glycerol-3–phosphoethanolamine-N-[methoxy(polyethylene glycol) (PEG-PE)- micelles, decorated with GLUT1 antibody.

They used this micellar system to treat U87MG 2D cell monolayers and U87-MG spheroids. They observed that free drugs (40 µM CUR and 0.8 µM DOX), both as single agents and in combination, were not cytotoxic on spheroids, while the same concentrations were lethal on monolayers (**Figure** 5).

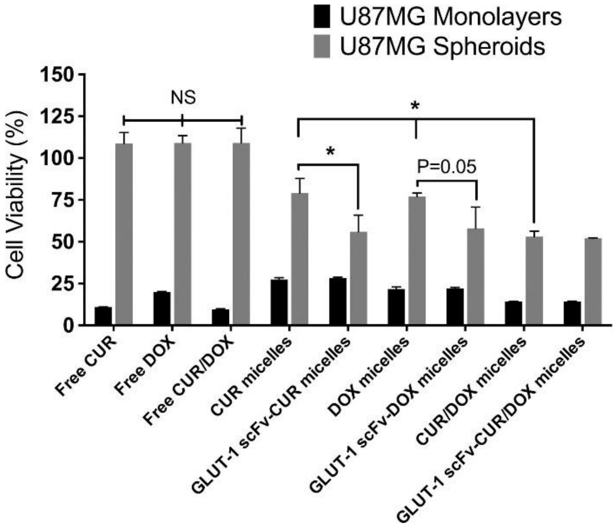

Figure 5: Evaluation of cytotoxicity on U87MG spheroids in vitro post 48-h treatment with DOX/CUR and DOX/CUR micelles. The spheroids were treated with 40 µM CUR and 0.8 µM DOX. The viability values obtained by CellTiter-Glo® assay.

Using the micellar formulation, the cytotoxicity was increased by 20%, and further improved with GLUT-1 targeting. [80]

This work highlights that 3D spheroid cultures have a different response to treatments, compared to conventional 2D monolayered cell cultures, confirming their importance in drug screening.[79]

These results proved once more the limitations of 2D cultures on drug testing.

Despite their advantages, spheroids present some limitations. For instance, their production must be optimized to reduce costs, large-scale production is still limited, their formation is not compatible with all cancer cell lines, and reproducibility is poor. [82] Another drawback is the lack of simple and standardized assays for acquiring spheroids functional images, analysis, quantification, and automation for drug screening purposes. [81]

Moreover, most of GBM spheroid models lack other microenvironmental non-tumour cells, the presence of a biomimetic ECM, as well as the presence of a BBB mimic, which are fundamental elements for GBM progression and invasiveness, as well as for drug resistance. [45]

Organotypic multicellular spheroids (OMS)

OMS are derived by the grounding of non-dissociated ex vivo fragments directly derived from surgical resections (from 0.3 to 0.5mm for glioma tissue). This procedure allows to maintain stromal components, such as macrophages and tumour vessels. They are generally cultured with liquid overlay method until their rounding, which can take from 2 to 5 days. The TME can be maintained for up to 70 days of culture. [82]

Organoids

Organoids are self-organizing structures, on a microscopic scale, derived from individual stem cells, which enable to recreate histoarchitecture and cellular composition of the native tissue. They are more often obtained from pluripotent stem cells (PSCs), such as induced PSCs (iPCSs).

Organoids can be obtained following three different procedures. First one involves the use of genetic bioengineering of brain organoids to introduce the oncogene through CRISPR/Cas9 Sleeping Beauty method. Another way is to incept tumour material into brain organoids; in this case, brain organoids are cocultured with glioma CSCs or neurospheres to obtain a newly developed glioma. Lastly, they can come from tissue derived tumour, where these pieces of tissue are compacted by using Shaker or spinner into Organoid medium Matrigel pearls. [50]

2.2.2 Scaffolds

Scaffold-based models can consist of different materials, from synthetic to natural ones, such as hydrogels, solid scaffolds, or microbeads. [83] These models can harbour either single cells or MCTS. [83] Their principal function is to give support to cells, or spheroids, while mimicking biochemical and mechanical properties of the ECM. Moreover, polymers may apply mechanical forces on the cells, inducing changes in gene expression through a process known as mechanotransduction. [84]

A common approach is that scaffolds are first created, and then cells are subsequentially cultured on them. Alternatively, can be embedded MCTS inside the matrix of the scaffold itself. This embedding has also been used to help the progression of MCTS, since matrix-free MCTS are easily disrupted during culture manipulation [83]

Depending on the 3D structure of the scaffold, these models can be divided into hydrogels, fibrous scaffolds, and porous scaffolds. [85]

Hydrogels are microporous polymer networks that have high water absorption capacity. Physical or chemical cross-linking of liquid precursors leads to the creation of solid scaffolds. This permits the encapsulation of the cells within the scaffold at the beginning of the fabrication process. As hydrogels are rich in water, the transport of oxygen, nutrients and growth factors is facilitated. Depending on their composition, hydrogels can have similar biophysical and biochemical characteristics to the ECM, hence representing a more realistic in vitro model and the most frequently used one. [86]

Of particular interest are natural polymers, such as collagen and collagen-derivatives (for instance, gelatin), hyaluronic acid, alginate, chitosan, and commercial hydrogels, such as Matrigel®. This is due mainly to their bioactivity, biodegradability by enzymatic or hydrolytic mechanisms, and the interaction with cells through specific and established biochemical pathways, as well as the possibility to be easily remodelled by cells. These biomaterials have been used alone and in combination with proteins, RGD peptides, or matrix metalloproteinase-cleavable peptides.[87]

Among these, collagen, hyaluronic acid (HA) and Matrigel® are of extreme interest, since they contribute to the composition of the brain ECM. However, one important drawback is the lack of experimental reproducibility, as different batches can vary, negatively impacting on experimental results. [88] Recently, collagen has gained importance also in MCTS formation inside microfluidic devices [84]. For instance, Donglai Lv et all. [89], proposed a 3D structure of bovine collagen from spongy bone, to culture U87 and primary glioma cells, and compared their behaviour with the standard 2D culture. They observed that GBM cells in 3D collagen scaffolds displayed a high degree of morphological similarity with primary tumour tissue, as well as primary tumour cells. Moreover, the embedding of cells resulted in decreased proliferation and increased quiescence, compared to the 2D culture. They also evaluated the response to chemotherapeutic drugs, treating cells with either cisplatin (DDP), lomustine (CCNU) and TMZ, common anti-cancer drugs. U87 and primary glioma cells in 3D collagen structure demonstrated greater resistance to the drugs, as compared to the cell monolayer culture, demonstrating that the 3D setups increased resistance to therapies.

An important feature to obtain reliable MCTS in hydrogels, are the mechanical properties of the hydrogel Indeed, only recent studies began to investigate the effect of biophysical cues, such as the matrix stiffness in modulating GBM cell fates, since GBM progression has been correlated with altered tissue stiffness. Danqing Zhu et all. [90] analysed the behaviour of cells embedded in matrices of different stiffness. To do so, they prepared a polyethylene glycol (PEG)-based gradient hydrogel platform with brain-mimicking stiffness range (40–1,300 Pa), supplemented with HA, to incorporate a biochemical cue of the brain ECM. They used patient derived xenograft (PDTX) GBM cells. They observed that, areas of lower stiffness promoted cellular proliferation and spreading. Indeed, as shown in figure 6, after 7 days, cells in softer zones (zone 1, 2, and 3) began to spread with long protrusions. Instead, cells in stiffer zones (zone 4 and 5) formed spheroids, which grew up to day 21, with minimal protrusions. Cells in zone 3 were able to form large spheroids by day 14 and exhibited an intermediate spreading behaviour., The results suggested that hydrogel matrix with stiffness above ~900 Pa can block GBM cell spreading in 3D cultures (**Figure 6**).

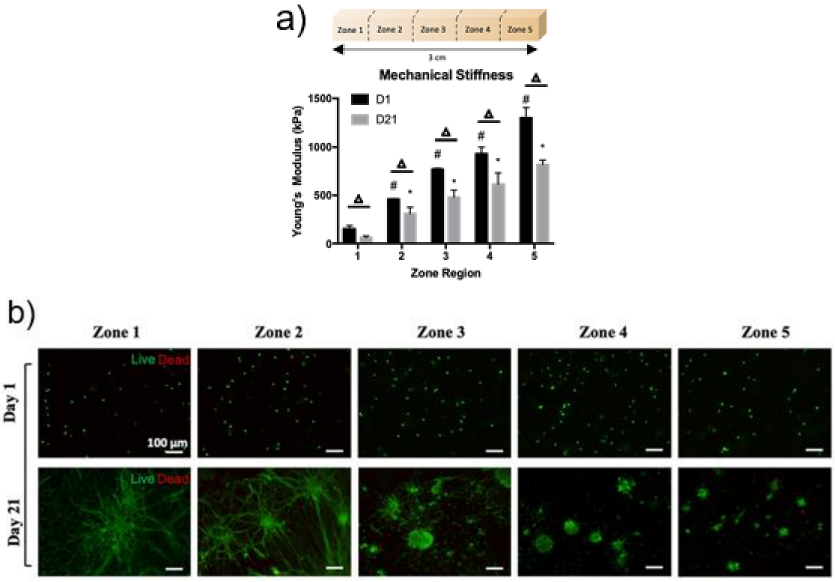

Figure 6: a) Mechanical characterization of gradient-stiffness PEG matrix, after day 1 and day 21, by compression test. b) Live/dead assay performed on cells on day 1 and day 21 after encapsulation in gradient hydrogels. Live: green; dead: red. Scale bar = 100 µm.

Furthermore, after 21 days in gradient hydrogel matrix culture, cells were subjected to TMZ for 72 hours. A decrease in cell viability was observed in all zones, compared to the non-treated ones (**Figure 7**). However, cells in the softest zone (e.g., zone 1) showed a 25% higher reduction of viability, when compared to cells in the stiffest zone, suggesting that high stiffness enhances drug resistance.

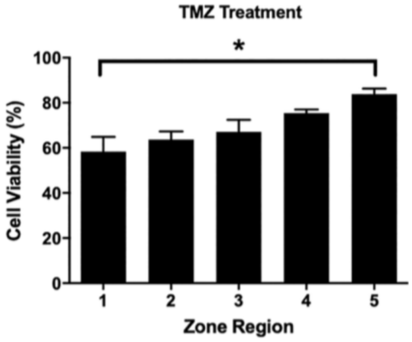

Figure 7: Drug response of GBM cells to a concentration of 30 µM of TMZ. Cells were culture in gel matrix for 21 days before being subjected to drug treatment. After 72 h, cells were subjected to a cell viability assay to quantify live cells percentage. Results suggest an increase in chemoresistance in stiffer matrix, leading to a higher percentage of live cells. Cell-containing hydrogels without TMZ treatment was used as a control for normalizing percentage of cell viability.

In addition, the capability of cells to release MMPs was evaluated. Results highlighted a 10-fold higher MMP-1 and MMP-2 expression in soft zone 1, compared to zone 5. Researchers concluded that that the softer matrix promotes ECM remodelling by GBM PDTX. (**Figure 8**).

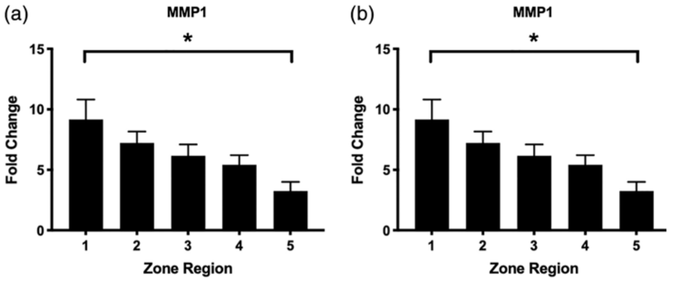

Figure 8: Graphs show the effects of the different hydrogel stiffness on PDTX GBM's MMPs gene expressions. The increase in matrix stiffness decreased expression of both MMP-1 and MMP-2 at day 7. On the other hand, their expressions were upregulated in softer matrixes. Fold of changes were calculated by normalizing day 7 to day 1.

In a similar study, spheroids of primary GBM cell lines or patient-derived spheroids, were encapsulated in a polyethylene glycol-based hydrogel[10].

To achieve spheroid embedding, the spheroid suspension was added to the gel precursor solution (∼50-75 spheroids per 100 µL). Then, 20 µL of hydrogel precursor droplets containing ∼10-15 spheroids were pipetted between two glass plates separated by 1 mm silicone spacers. After gelation, gels were placed into a 24-well plate. For drug screening, U87 cell spheroids were first incubated with 0.02 µg/mL DiOC for 24 h to stain all cells prior to spheroid formation. Spheroids were encapsulated in soft, stiff, and dual hydrogels and cultured in a 24-well plate for 3 days (**Figure 9**).

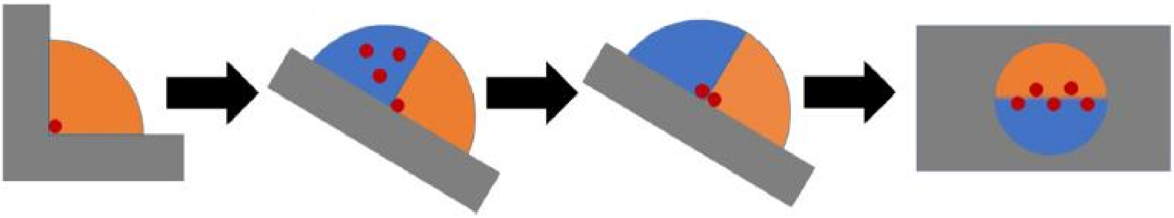

Figure 9: Schematic representation of PEG-based hydrogel formation (dual stiffness setup). Red dots representing spheroids encapsulation, where the orange colour represents soft gel, while the blue colour represents the stiff section.

On day 3, spheroids were treated with 2 mM TMZ (in 2% DMSO) and incubated for 48 h. [10]

Spheroids were able to infiltrate the hydrogel, resulting in an overall increase in their diameter and area. The spheroid core remained of the same size for the first 7 days, with only peripheral growth. Spheroids infiltrated the soft hydrogels earlier and to a higher extent. In soft hydrogels the spheroid diameter increased by 2.63-fold from day 1 to day 7, as compared to a 2.24-fold increase in the stiff hydrogel. (**Figure 10**).

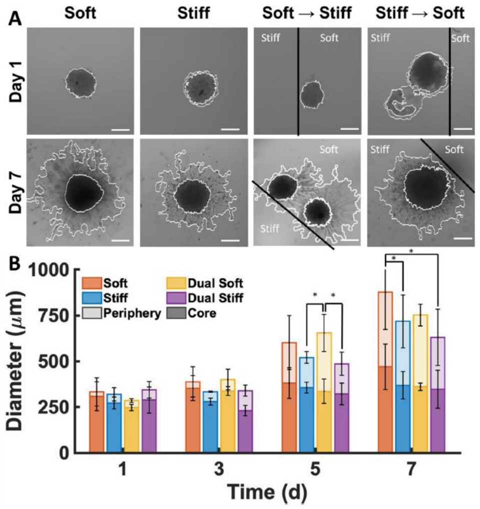

Figure 10: Size and infiltration of GBM spheroids, encapsulated in PEG hydrogels. A) acquired images of all hydrogel types for days 1, 3, 5 and 7. For ease of analysis, the core and the periphery of spheroids were outlined in white, while the borders between soft and stiff gels were marked with a black line. Scale bar= 200 µm. B) Graph representing changes in diameter of core and periphery as function of time for all hydrogel types.

Spheroids were treated with TMZ (2 mM on day 3) and incubated for 48 hours. TMZ exposure caused a decrease in spheroid diameter for all hydrogel conditions, with the higher effect on the spheroid periphery compared to the core. The decrease was significant for the soft (1.25-fold), stiff (1.14-fold) and dual-soft (1.37-fold) matrices (**Figure 11**).

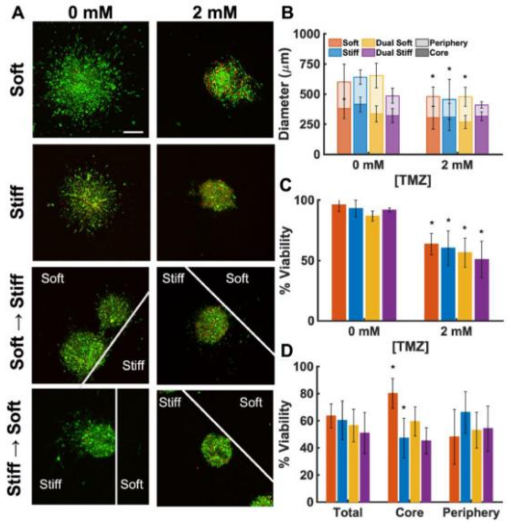

Figure 11: GBM spheroid response to treatment with a 2 mM of TMZ. A) representative fluorescence confocal microscopy images of spheroids in all hydrogel types undergoing treatment. All cells were stained with DiOC (green), and dead cells were stained with PI (red). Scale bar = 200 µm. Diameter (B) and cell viability (C) of spheroids in all hydrogel types as a function of TMZ exposure. D) Cell viability in the spheroids core and periphery upon exposure to 2 mM TMZ.

Similarly, drug resistance was also reported for spheroids cultured in synthetic hydrogels. [91] For instance, PEG hydrogels were used to tune matrix degradability, where degradability was induced with an enzymatically degradable crosslinker, as well as adhesiveness, where cell adhesion was boosted by the adding of an integrin ligand. Spheroids were embedded in a 1) non-degradable and non-adhesive (ND-NA), 2) degradable and non-adhesive (D-NA) and lastly degradable and adhesive (D-A) hydrogel, with a Young's modulus of around 1.75 kPa (resembling the brain tissue stiffness).

To conclude, in another article, it was demonstrated how the hydrogel matrix presence and composition significantly affected drug response of embedded GBM spheroids.

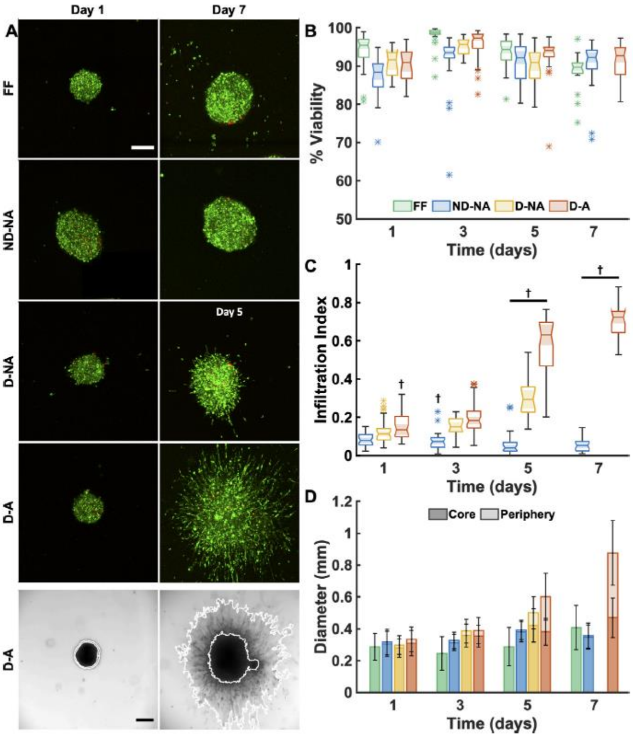

Figure 12: Cell viability and infiltration of FF and hydrogel embedded U87 spheroids. A) Images obtained by performing a Live/Dead assay of U87, cultured as FF, ND-NA, D-NA and D-A, for up to 7 days (5 days for D-NA hydrogels). Brightfield images at the bottom show how core and periphery spheroids diameters were considered for analysis (marked in white outlines). Scale bar= 200µm. B) Cell viability for all spheroids conditions, for up to 7 days. C) Infiltration index of spheroids for all conditions. D) Spheroid diameter for both core and periphery. (n=3).

With reference to **Figure 12**, when spheroids were maintained in free floating conditions, their size increased significantly from day 1 to 7. For ND-NA spheroids the diameters did not change significantly. Overall, increase in core spheroid diameter was similar in all gels and comparable with free floating spheroids. On the other hand, peripheral diameters of D-NA and D-A were significantly higher, showing a remarkable difference between the two conditions on day 5. This phenomenon was also evaluated in terms of a variable, defined "Infiltration index", with 0 indicating no invasion while 1 standing for complete infiltration. ND-NA showed no change in infiltration while, degradable gels showed an increase in infiltration index, from day 1 to 5, especially for D-A conditions. Therefore, degradability, which was associated with a lower Young's modulus, was a fundamental pre-requisite for infiltration. After treatment with TMZ, (2mM.) the spheroid viability was higher for D-NA spheroids, followed by D-A ones. This indicated that gel infiltration resulted in a lower susceptibility to the drug. Moreover, more dead cells were found in the spheroid periphery, compared to the core in all gel conditions, specifically peripheral viability was higher for D-A gels than ND-NA.

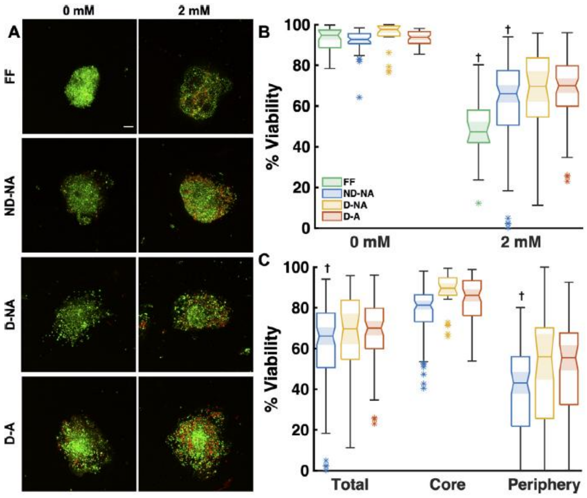

Figure 13: Cell viability and infiltration of FF and hydrogel embedded U87 spheroids, after 2mM TMZ treatment. A) Images obtained by performing a Live/Dead assay of U87, cultured as FF, ND-NA, D-NA and D-A, for up to 7 days (5 days for D-NA hydrogels). Scale bar= 200µm. B) Cell viability for all spheroids conditions, for up to 7 days, upon TMZ treatment. C) Cell viability for all spheroids conditions, for up to 7 days, upon TMZ treatment, separately showing results from the total, core, and periphery area. (n=3).

To determine whether the different drug response was due to a reduced drug diffusion, rather than to acquired resistance, a fluorophore of similar size to TMZ was used and permeability calculated. As expected, the diffusion coefficient was significantly higher in media compared to all hydrogel conditions. However, there was no difference in diffusivity between all hydrogel conditions, proving that the material properties, such as degradability and adhesiveness, are fundamental to better recapitulate the response of GBM models in vitro (**Figure 13**). [91]

2.2.3 Microfluidic Devices

Microfluidic devices, also referred to as “Organ/Tumour-on-a-chip” represent a promising testing tool for drugs and nanomedicines. Indeed, these devices can be produced at low-cost with a customizable design and allow to preserve cells phenotype. They allow control on physical and biochemical properties of the tumour microenvironment as well as the inclusion of a well-defined vessel endothelium, functioning as a BBB. These systems are often dynamic, with tuneable fluid gradients allowing to set also hydrodynamic parameters. Moreover, these systems allow real-time monitoring, while being microscopy compatible.[92] [93] For GBM replication, these systems allow to include a functional BBB, which is a fundamental parameter, as it also reproduces tumour angiogenesis, a critical step in GBM development. [94]

Suyeong Seo et all [95] used a microfluidic device to coculture BBB within a 3D hydrogel matrix (**Figure 14**).

Firstly, the vessels were created and characterized by measuring the expression of BBB-specific markers and by measuring vascular permeability. Then, to mimic the tumour, they used U87 and T98G GBM cell lines, to form spheroids to be included inside the chip.

The design of the chip consisted of a rectangular PDMS chamber, within which three different channels were created by inserting three microneedles inside a solution of collagen type I (3mg/ml), human brain vascular pericyte (PC) and human astrocyte (AC), which was allowed to gel before the removal of needles.

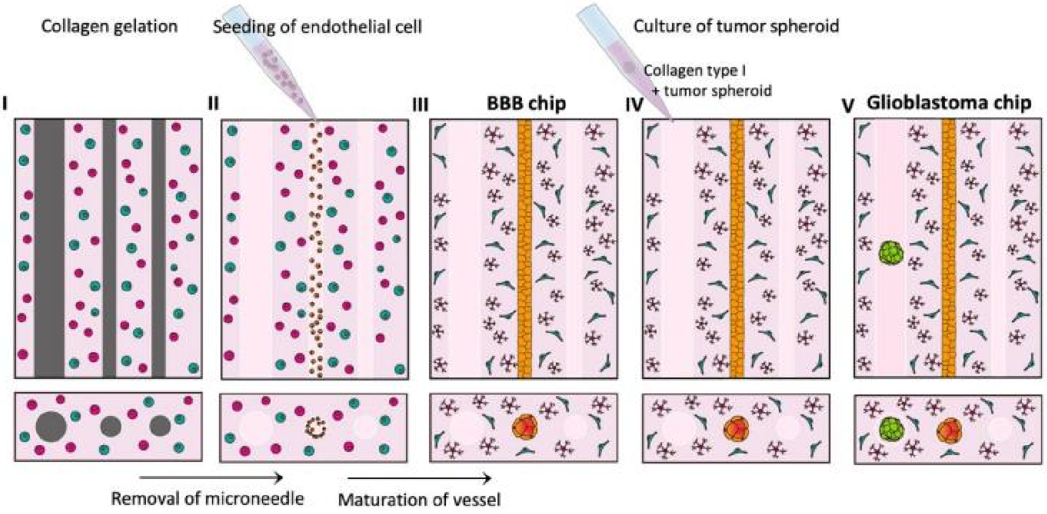

Figure 14: Representative schematic visual of the device’s design, with the three channels created by the removal of the needles, after gelification. The scheme also shows the different step that needs to be followed to create the Glioblastoma chip. Image obtained from [95].

Once the hollow cylindrical channels were created, a suspension of endothelial cells was injected to form matured vessels, after 5 days of culture. The chips were maintained under gravity-driven flow.

Confocal images confirmed that pericytes closely distributed around the blood vessels, in direct contact. Moreover, AC encircled the endothelium by spreading their end feet. The presence of typical junctional proteins (ZO-1 and Claudin-5), basement membrane proteins, such as collagen (COL4) and laminin, as well as specific transporters (GLUT1 and P-glycoprotein), was detected along the entire vessel length (**Figure 15**).

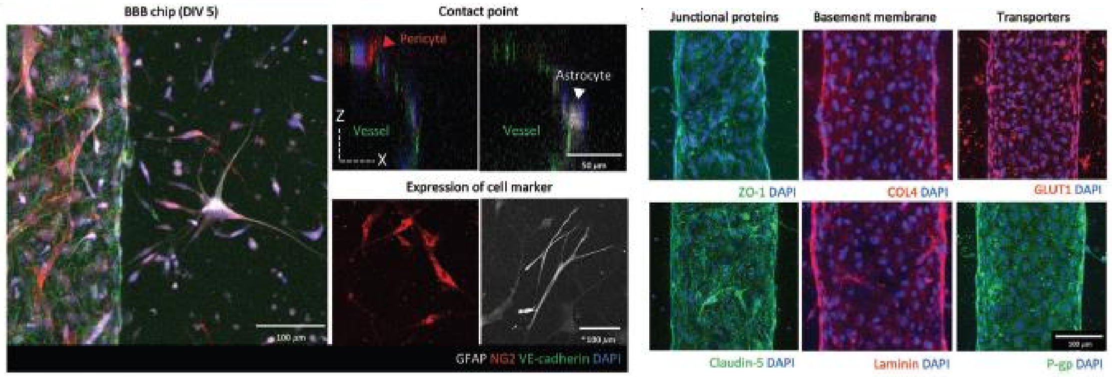

Figure 15: Left: confocal images of the BBB chip showing the staining of the specific markers of cells on day 5 of culture. Right: Physical barrier of the blood vessel confirmed by the staining of tight junctions, basement membrane and specific transporters on the endothelial cells. Scale bar= 100µm.

The trans-endothelial permeability of the obtained BBB was verified by injecting different molecular weight fluorescent molecules, such as 376 Da, 4 kDa and 40 kDa. The authors showed a decrease in permeability with increasing maturation, proving that vessels matured over time until the formation of a well *integra* BBB with physiological permeability. The obtained permeability in triculture for 4 kDa fluorescein isothiocyanate (FITC)-dextran on day 5 of maturation was about $1.83 \times 10^{-8} \pm 1.60 \times 10^{-8}$ cm/ s, comparable to in vivo values ($\approx 10^{-7}$ cm/s) (**Figure 16**).

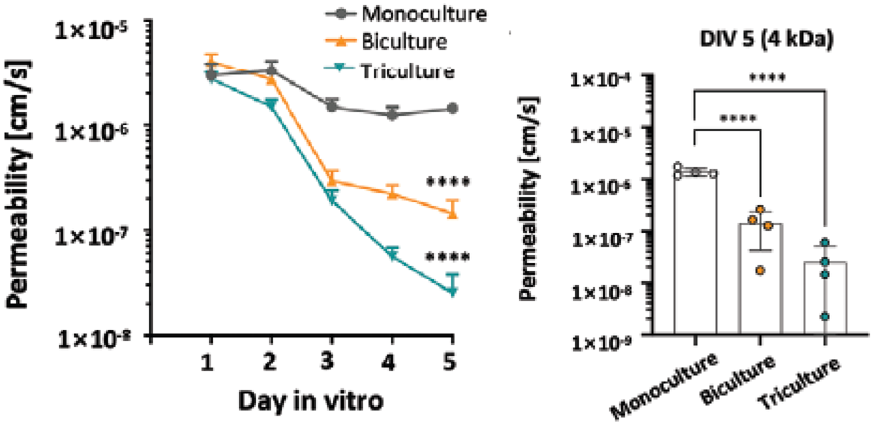

Figure 16: Evaluation of the functionality of the engineered BBB chip for 4 kDa fluorescein isothiocyanate (FITC)-dextran. First graph shows the changes in vascular permeability over the culture period, proving that increasing time of culture leaded to a more mature vessel, lowering the permeability, most of all when refering to the triculture condition (lowest value on day 5). The right graph shows the measurment of vascular permeability of the matured BBB chip on day 5. The permeability was in the range of $_{P40\ kDa}$, tri = $1.83 \times 10^{-8} \pm 1.60 \times 10^{-8}$ cm/ s).

GBM Spheroids were njected into one of the channel near the new generated vessel.

The presence of the tumour caused evident changes in the BBB, causing endothelial sprouting, preferentially toward the spheroid. This was accompanied by a vasodilatation of the blood vessel (**Figure 17**). The authors hypotized that cytokines associated with tumour angiogenesis, such as IL-34 and Heparing binding epidermal growth factor were released from the GBM spheroid.

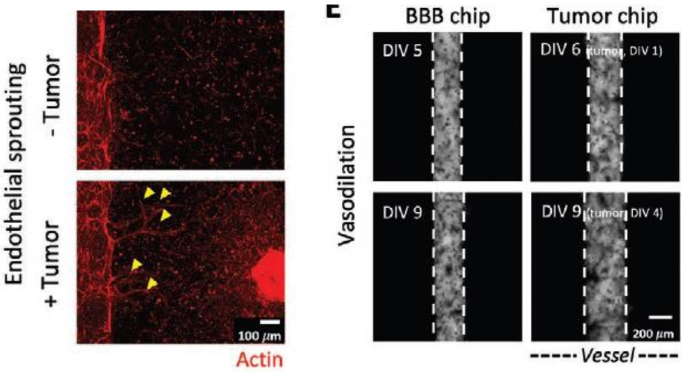

Figure 17: Left image shows the staining of Actin for analysing the formation of new vessels from pre-existing vessels toward the GBM spheroid. Second image shows the vasodilation induced by tumour, after the insertion of the spheroid.

After that, spheroids were treated by injecting either a solution of doxurubicin (DOX, 50 nM) or vincristine (VCR, 10 μM) through the luminal structure, simulating an in vivo administration. They noticed that the drug was correcty administered to the sferoid, causing a inhibition of growth and a reduction of the migratory area. Indeed, there was a decrease in the size of tumour spheroids after 4 days of treatment (**Figure 18**).

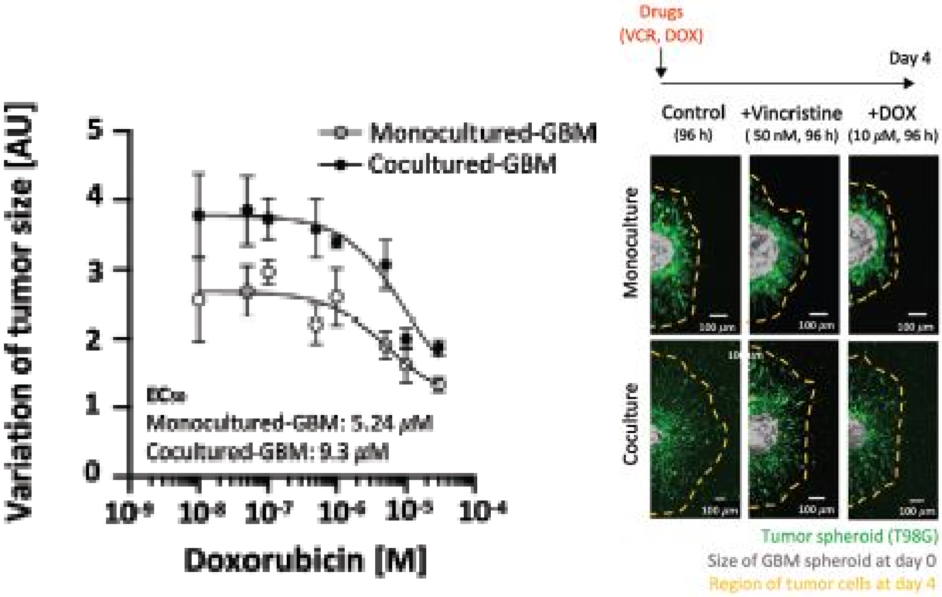

Figure 18: First graph shows the variation in tumour size, on day 4 of adminitstation, due to the treatment with DOX, with different concentrations. Second graph otherwise shows the trend in invasion distance from initial area.

Moreover, dynamic interactions with the BBB caused morphological changes in the GBM spheroid. Indeed, the spheroid had a longer invasive front when cultured in the chip. Thus, this platform allowed to reproduce changes in the BBB structure and function in response to GBM, as well as performing reliable drug screening.

In a similar work, Shi et all., [39] developed an in vitro BBB microfluidic chip model, containing primary human brain endothelial cells, pericytes, astrocytes and glioma cells. Six potential compounds were tested in this model.

The design of the chip comprised four different channels, made of PDMS. One was for the construction of the blood channel, one for the brain parenchyma channel, one for the tumour channel and the last one for the medium (**Figure 19**).

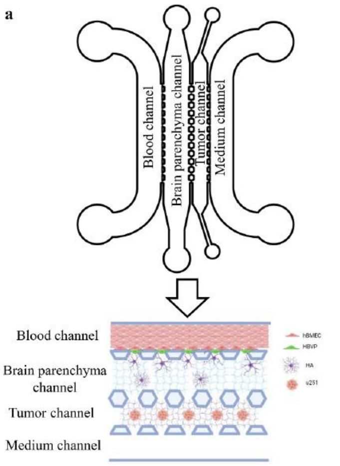

Figure 19: Schematic representation of BBB-U251 chip. The four different channels are shown in this figure showing their position. Images obtained from [39].

For the brain parenchyma channel, a mix of Astrocytes in a fibrin gel was selected and polymerized in a cell incubator for 15 minutes. This step was immediately followed by the injection of astrocytes culture medium. For the blood vessel, after an incubation with Matrigel for 40 minutes, primary human brain vascular pericytes (HBVP) and primary human brain microvascular endothelial cells (hBMECs) were sequentially injected into the blood vessel. The device was then connected to a peristaltic pump. After 1 days of culture, a mixture of U251 cells in Matrigel was injected into the tumour channel and left in the incubator for 20 minutes. Cells were verified to be alive through a Live/dead staining (**Figure 20**).

The barrier function of the BBB unit was first assessed without U251 cells using various-sized FITC-dextrans (4, 40, and 70 kDa), as well as three model drugs. A functional and highly selective BBB unit was established in this microfluidic model and was suitable for further drug transport experiments.

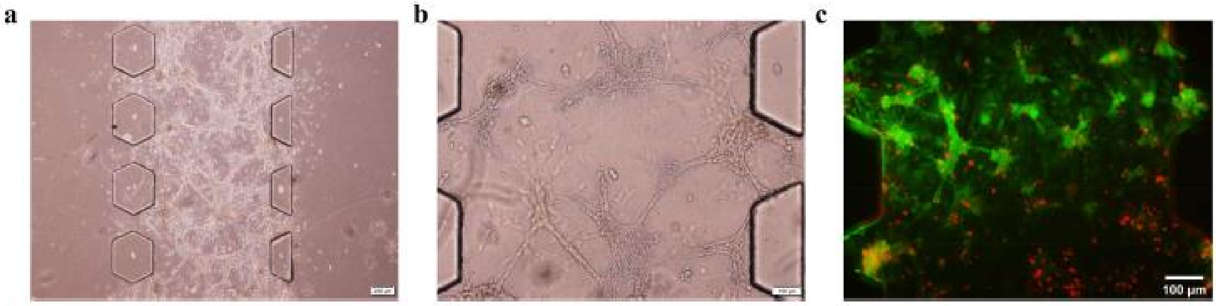

Figure 20: (A-B) Brightfield images of U251 multicellular spheroids on the chip. (C) Live/dead staining of U251 on microfluidic chip.

Two anti-tumour drugs (Docetaxel and Temozolomide) were administered at a concentration of 2.5 µM and 400 µM, respectively, through the vessel channel. The authors showed that TMZ can actually penetrate the BBB and induce U251 cell apoptosis. (**Figure 21)**

On the other hand, Docetaxel was not able to bypass the BBB, which is consistent with published reports. [96]

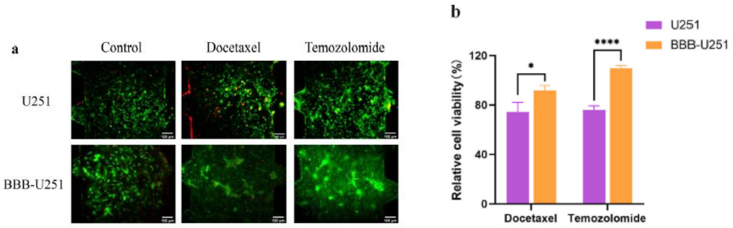

Figure 21: (A) Live/dead cell staining of U251, with the different treatment. (B) confrontation of the toxicity results of docetaxel and temozolomide on U251 cells in BBB-U251 chip and U251 chip.

3 Aim of the work

The primary goal of this thesis is the development and characterization of different in vitro three-dimensional (3D) GBM models. For this purpose, different cell lines will be used to recreate the heterogeneous cellular milieu that characterizes GBM. GBM cells (U87 MG), and GBM-8 (a human GSCs model) will be used to reproduce the heterogeneity of the tumoral component in GBM. Non-tumours cells, which are part of the TME, such as human microglia (HMC3), and human brain astrocytes cell lines (HASTR/ci35) will be included. Moreover, considering the key role played by the BBB in GBM progression and drug response [97], two additional cell lines will be included, i.e., human endothelial brain cells (HBEC-5i) and human brain vascular pericytes (HBVPC/ci37).

Once MCTS will be obtained, drug screening tests will be performed using Bortezomib (BTZ), an FDA-approved anti-tumour drug, which showed promising results after intra-cranial injection in GBM models. [98] Since it has been demonstrated that this drug is not able to penetrate through the BBB, a drug transport system based on nanoparticles (NPs) or cellular transporters (such as microglia) will be designed. [99] ,[100]. Before testing, NPs will be characterized in terms of yield, encapsulation efficiency and drug release kinetics.

Different spheroid compositions will be analysed. The simplest spheroids will be composed of monocultures of the above-mentioned cell lines, to understand their single contribution to drug resistance. Then, more complex models will be obtained by co-culturing U87 with HMC3, in two different ratios, 30% and 50%. [101]. Coculture of U87 and GMB-8 (10%), referred to as “Tumour Mix”, will also be tested, alone or in combination with HMC3 (30% or 50%). This composition will allow the integration of GSCs in the model, which is a crucial aspect considering their role in drug resistance. [102] Furthermore, human brain astrocytes, in different *ratios* with Tumour Mix, will be added. All drug tests will be performed at increasing concentrations of drug, either in free form or encapsulated in NPs.

Proliferation and infiltration inside a gel matrix, mimicking the tumour ECM will also be investigated. This will be obtained by embedding spheroids in two different hydrogels matrices: a Collagen-I (4mg/mL) hydrogel and a polysaccharide hydrogel (VitroGel® 3D High Concentration). Since GBM ECM is composed by varying concentration of Collagen, proteins, and GAGs [46], that contribute to the variations of the Young’s Modulus [51], testing the behaviour of spheroids in matrices of different mechanical properties is fundamental. Furthermore, VitroGel® represents an animal-free option that needs to be investigated.

The effect of HMC3 in the gel matrix will also be considered, when analysing the spheroid response to drug treatment. HMC3 migration through the gel matrix will be investigated using different testing configurations, in the presence or absence of the tumour spheroid. This will allow to study whether the presence of the tumour mass can influence the migration of HMC3 cells.

I*n vitro* three-dimensional models of the BBB will also be created in the form of spheroids, by coculturing HBEc-5i and HBVPC, ì HASTR and HBVPC (1:1), and HBEC-5i, HASTR and HBVPCs, or by using a commercial microfluidic platform (MIMETAS Organo Plate® Graft). The microfluidic device allows to replicate angiogenesis, which can be stimulated to induce vascularization of the spheroid. BBB model will be characterized in terms of characteristic protein markers (ZO-1, CD31) and microglia circulation and tissue infiltration ability will be tested in the microfluidic device.

4 Materials And Methods

4.1 Materials

4.1.1 Nanoparticles

A proprietary poly-caprolactone (PCL)-based polyurethane (NS-HC2000) was used to synthesize the core structure for the nanoparticles (NPs). The lipidic outer shell of the NPs was formed by a mix of L-α- phosphatidylglycerol (Egg, Chicken) (sodium salt) (EGG-PG) and 1, 2-Distearoyl-sn-glycero-3-phosphoethanolamine-Poly (ethylene glycol) (DSPEPEG), both purchased from Avanti® Polar Lipids.

A fluorophore-labelled lipid, l-α-phosphatidylethanolamine N-(lissaminerhodamineB-sulfonyl) (Egg-Liss-Rhod PEDSPE-PEG, Avanti® Polar Lipids), was added during the formation of the shell to create fluorescent NPs. The proteasome inhibitor Bortezomib (BTZ, Selleck Chemicals), was encapsulated inside the NPs polymeric core. All solvents were of analytical grade.

4.1.2 Cell cultures

All cell lines (except for Human Brain Pericytes and Astrocytes) were incubated at 37°C, in a 5% CO_2 atmosphere. For the detachment of cells, Trypsin (Gibco™) was used. Cells were generally cultured on T75 flask and split approximately every three days or when needed.

1. GBM-8, cancer stem cells (CSCs) derived from Human Brain Cancer Tissue, were provided by a collaborator (Houston Methodist Research Institute) and cultured in non-adhesive flask using Neurobasal Medium (Gibco™), with the addition of Heparin in the concentration of 2 mg/ml, 0.2% B27 supplement, 0.5% N2 supplement, 20 mg/ml of Epidermal Growth Factor (EGF) and Fibroblast Growth Factor (FGF) and 1.4% L-Glutamine (all purchased by Gibco™).
2. Differentiated human GBM cells U87 MG, supplied by American Type Culture Collection, ATCC® HTB14TM, and their fluorescent version obtained by transfection with Green Fluorescent Protein (GFP) were cultured in Minimal essential medium (MEM), added with 10% Fetal Bovine Serum (FBS, Gibco™) and with 1% Penicillin/Streptomycin (1% P/S) (Gibco™).
3. HMC-3 (HMC3, ATCC® CRL3304TM) human microglia cells, were cultured in the same medium of U87 cell lines, with 12 % FBS.
4. HBEC-5i (Human Cerebral microvascular endothelial cells, ATCC® CRL3245TM, collected from the cerebral cortex) were cultured using a DMEM: F12 medium, 40 µg/ml Endothelial cell growth supplement (ECGS, Sigma Aldrich), 10% FBS and 1% P/S.
   To allow the adhesion of cells, flask surface was coated with 1.0 ml of 1% gelatin (ATCC) and incubated with the solution at 37°C for 45 minutes. The solution was removed before the dispensing of cells into the flask.
5. HBVPC/ci37 (Human Brain Vascular Pericytes, conditionally immortalized, clone 37, developed by the Tokyo University of Pharmacy and Life Sciences) [103]. Pericytes were cultured in Pericyte Growth Medium 2 (PromoCell®), antibiotics (1% P/S) and blasticidin S (4 µg/mL) (Blasticidin S Hydrochloride (From Streptomyces Griseochromogenes), Fisher BioReagents).
6. HASTR/ci35 (Human Astrocytes conditionally immortalized, clone 35 developed by the Tokyo University of Pharmacy and Life Sciences). These cells were cultured in Gibco Astrocyte medium (Life Technologies, Cat# A1261301) with supplements, antibiotics (1% P/S) and Blasticidin S Hydrochloride (Fisher BioReagents).

For the embedding of cells or spheroids inside a G-ECM mimic, two different hydrogels were used:

- Collagen-I hydrogel 4mg/mL, (AMSbio Cultrex® 3D collagen I rat tail, 5 mg/mL, #3447-020-01), mixed with 1 M HEPES (ThermoFisher 15630-122, pH 7.2-7.5) and 37 g/L $NaHCO3$ (Sigma S5761-500G), in 8:1:1 ratio.
- VitroGel® 3D High Concentration, TheWell Bioscience, Inc)

To achieve the vascularization of the spheroids, a commercial culture device, MIMETAS OrganoPlate® Graft (MIMETAS, 6401-400-B), was employed. This device presents 64 microfluidic chips (**Figure 22**), each characterized by an open graft chamber, able to house the selected tissue model, two side perfusion channels, which simulate the vasculature, and a central upper channel, allowing the injection of the G-ECM gel. For this platform, there is no need for pumps, indeed the design allows the flow of medium all around the device, using a rocker shaker, supplied by the producer (OrganoFlow®).

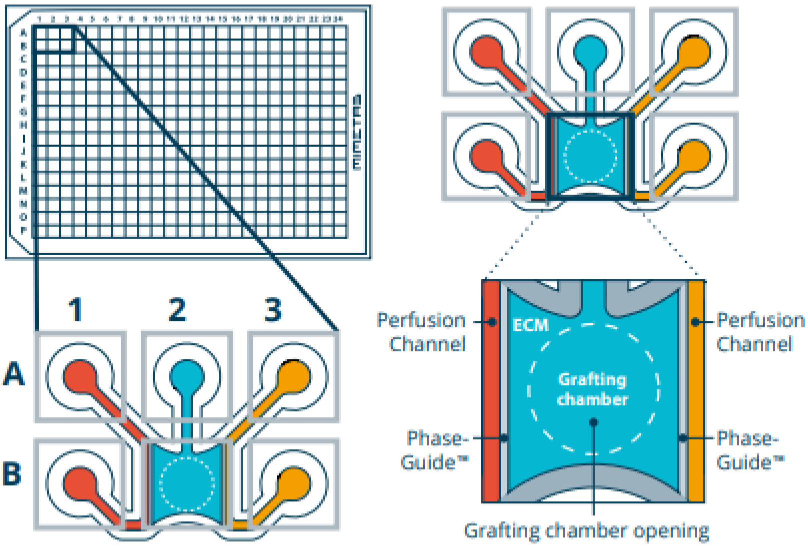

Figure 22: Schematic representation of MIMETAS OrganoPlate® Graft single chip layout. 2B position represents Graft Chamber (where the spheroid is harboured, after G-ECM gel loading), while 2A position represent the Graft Inlet. On the side (column 1 and 3, A/B) the two perfusion inlets and outlets are shown, which are directly connected to the perfusion channels inside the Graft Chamber, interfacing with the housed tissue. Image from https://www.mimetas.com/en/organoplate-graft.

An angiogenic cocktail was used to facilitate the formation of vessels and sprouts, which was composed as described in **Table 1.**

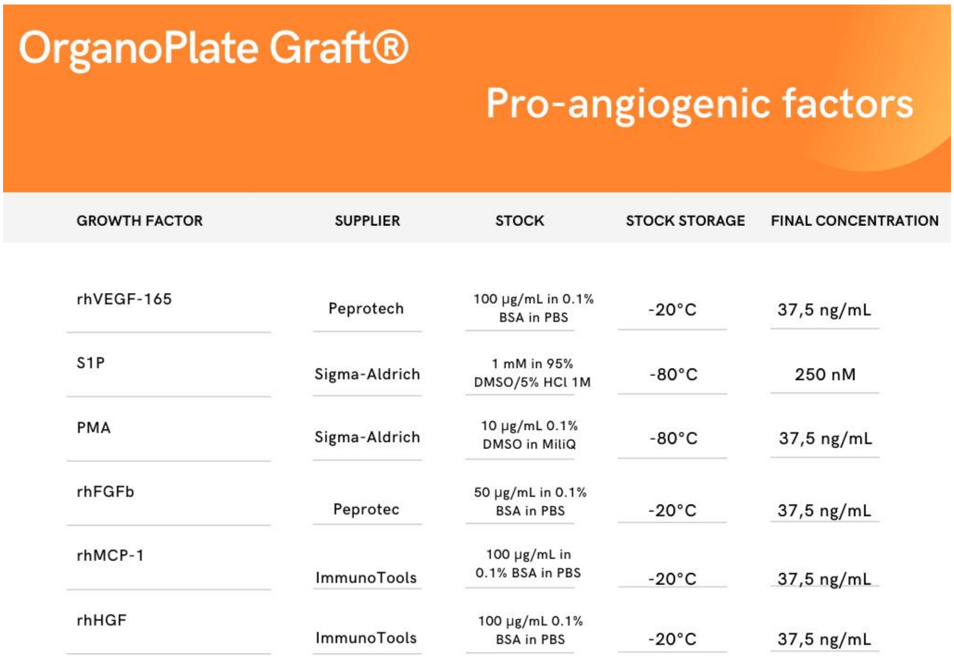
OrganoPlate Graft®

Pro-angiogenic factors

GROWTH FACTOR	SUPPLIER	STOCK	STOCK STORAGE	FINAL CONCENTRATION
rhVEGF-165	Peprotech	100 µg/mL in 0.1% BSA in PBS	-20°C	37,5 ng/mL
S1P	Sigma-Aldrich	1 mM in 95% DMSO/5% HCl 1M	-80°C	250 nM
PMA	Sigma-Aldrich	10 µg/mL 0.1% DMSO in MiliQ	-80°C	37,5 ng/mL
rhFGFb	Peprotec	50 µg/mL in 0.1% BSA in PBS	-20°C	37,5 ng/mL
rhMCP-1	ImmunoTools	100 µg/mL in 0.1% BSA in PBS	-20°C	37,5 ng/mL
rhHGF	ImmunoTools	100 µg/mL 0.1% BSA in PBS	-20°C	37,5 ng/mL

Table 1: List of Pro-angiogenic factors needed to prepare the angiogenic cocktail. Final concentration refers to the concentration in the final solution, obtained by diluting the relative stocks in an appropriate manner in any desired medium.

A repeating pipette (eLINE® electronic pipette, Sartorius, #735021, previously #730021) was used along all procedures to reduce operator-caused error and increase repeatability.

4.2 Methods

4.2.1 NPs Preparation and characterization

To prepare the NPs, NS-HC2000 was dissolved in acetonitrile (ACN) (at a final concentration of 10 mg/ml). The polymer solution was then diluted to 1 mg/ml (in ACN). When BTZ-loaded NPs (BTZ-NPs) were prepared, 50 µg of BTZ were added to the polymer solution (1mg/ml in ACN).

A lipid solution containing 200 µg of DSPE-PEG and 240 µg of EEG-PG in double-distilled water (ddH$_2$O), was prepared, for a total volume of 2 ml. This lipid solution was kept under stirring (300 rpm) at 60°C to prevent the formation of micelles. For fluorescent NPs, 10 µg of Egg-Liss-Rhod PEDSPE-PEG were added to the solution.

The polymer solution was added dropwise to the lipid solution to induce the spontaneous nanoprecipitation of core-shell NPs. Lastly, 1 ml of water was added to reduce the temperature and allow solvent evaporation. The particle suspension was centrifuged using Amicon ® Ultra centrifugal filter units (Merck Millipore), presenting a 10kDa cutoff-membrane for 13 minutes at 3200 rpm and room temperature (RT). After this step, 1 ml of distilled water was added to the filter unit and centrifuged again at the same speed and temperature. After that, the non-filtered NPs suspension was retrieved and re-suspended in 1 ml of ddH$_2$O or culture medium for further characterizations. The steps of the procedure are shown in **Figure 23**.

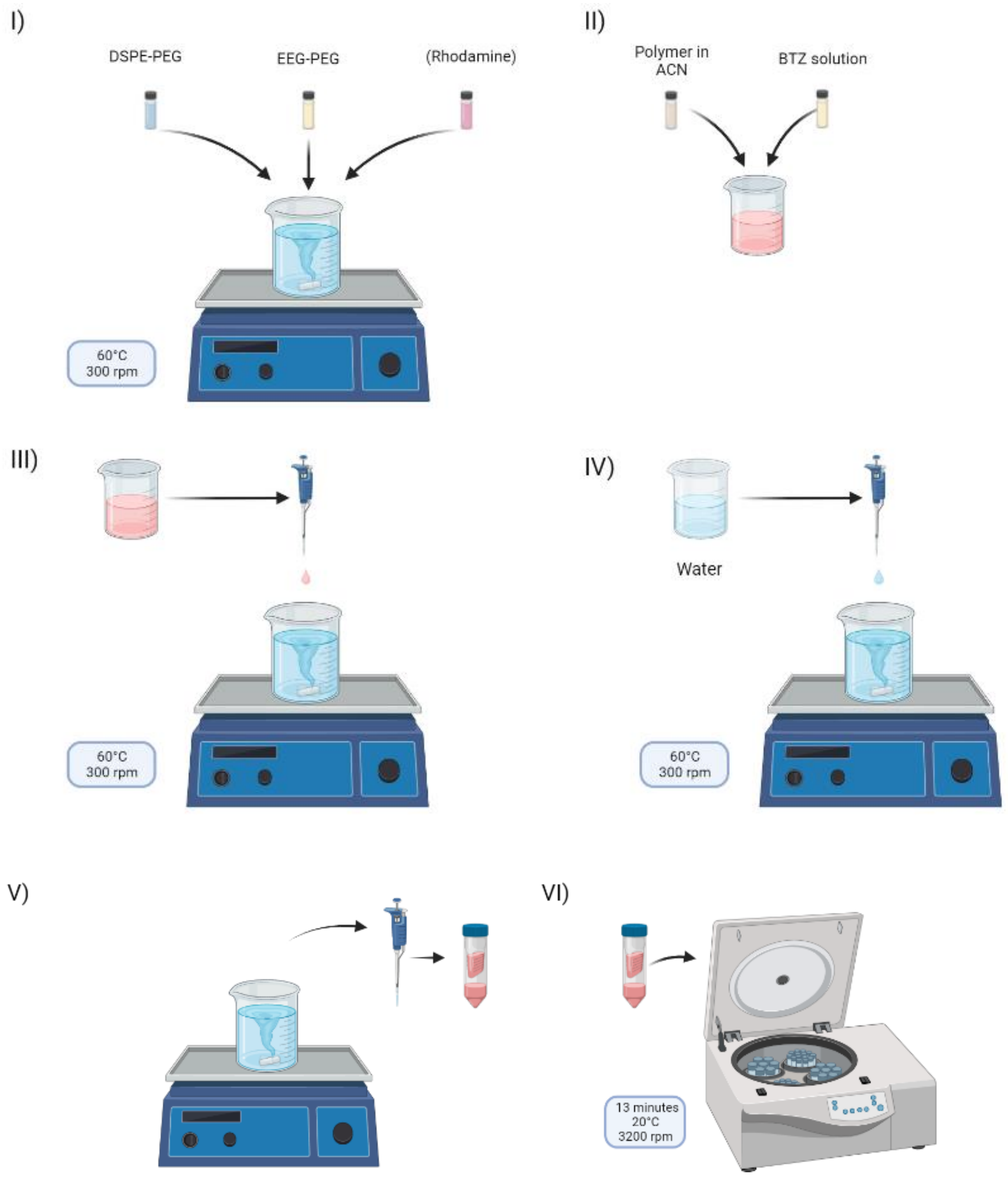

Figure 23: Schematic of NPs preparation; I) Lipid solution preparation; II) Polymer and BTZ solubilization in ACN; III) Dropwise addition of the polymer solution into the lipid solution and formation of core shell NPs; IV) Dropwise addition of distilled water to the NPs suspension under stirring to reduce the temperature and facilitate solvent removal. V) and VI) Centrifugation (x2) of the NPs suspension using Amicon filter units. Image created with Biorender.com.

Yield

At the end of the process, the yield was evaluated by freeze drying (LaboGene CoolSafe 4-15L) the NPs suspension and weighing the mass of the obtained NPs powder, according to the following equation *(5.2.1.1):*

$$Yield(\%) = \frac{Weight\ of\ the\ formulation}{Weight\ of\ polymer + Weight\ of\ drug + Weight\ of\ lipidic\ components} \cdot 100 \qquad (4.2.1.1)$$

- The *weight of the formulation* is the mass of NPs obtained at the end of the process.
- The *weight of polymer* is the mass of NS-HC2000 initially added in solution (1 mg)

- The *weight of drug* represents the amount of BTZ initially added to the polymer solution (50 µg).
- The *weight of lipid components* is defined as the sum of EGG-PG (200 µg) and DSPE-PEG (240µg) masses in the initial solution.

NPs were characterized by Dynamic Light Scattering (DLS) to measure their hydrodynamic diameter, which refers to the diameter of the NPs present in the solution surrounded by a thin layer of water, and polydispersity index (PDI), a value ranging between 0 and 1 related to the uniformity of diameter distribution in the whole solution.
The Zeta Potential of the NPs was assessed using the Litesizer™ Omega cuvettes, presenting gold electrodes to induce an electric field. This important parameter provides information about the stability of the suspension. The higher the absolute value of PDI, the lower is the tendency of NPs to form aggregates. These physical characterizations were performed using a Litesizer™ 500 (Anton Paar).

Encapsulation efficiency

To define the encapsulation efficiency (%) for BTZ-loaded NPs (BTZ-NPs), freeze-dried NPs were dissolved in 0.5 mL ACN to induce NPs rupture and drug release. The amount of drug in the NPs was assessed from the absorbance at the characteristic peak of BTZ (270 nm) through an empiric calibration curve. Absorbance was detected using a UV/VIS spectrophotometer (Lambda 365, Perkin Elmer®, Waltham, MA, USA). The encapsulation efficiency (EE) was then determined from these data using the formula (**Equation 5.2.1.2**).

$$EE(\%) = \frac{Amount\ of\ drug\ in\ NPs}{Amount\ of\ drug\ supplied} * 100 \qquad (4.2.1.2)$$

The total amount of drug in NPs is the BTZ mass detected through UV/VIS spectroscopy, while the amount of drug supplied is the BTZ mass used for BTZ-NPs preparation (50 µg).

Drug release

For the evaluation of the cumulative drug release, three formulations of BTZ-NPs were incubated at 37 °C in 1 mL ddH_2O. The experiment was performed in triplicate.

At the selected incubation timepoints, the NPs were retrieved from the incubator and the released drug was collected with the following procedure:

1. NPs were centrifuged (Beckman Coulter Allegra X 30) at 10.500 rpm for 10 minutes at room temperature, allowing the formation of a NPs pellet at the bottom of the tube.
2. The supernatant was transferred to another Eppendorf tube.
3. Distilled water (1 mL) was added to the NPs pellet and the suspension was pipetted to facilitate NPs dispersion.
4. The freshly obtained suspension was placed again in the incubator till the next time point.

Steps 1 to 3 were repeated at 1 hour, 3 hour and daily for a week.

The collected supernatants were freeze-dried overnight. The powder was solubilized in 0.5 ml acetonitrile and the amount of drug was detected using UV/VIS spectrophotometer (Lambda 365, Perkin Elmer®, Waltham, MA, USA) with the same procedure employed for the definition of the EE.

4.2.2 Spheroid-based models

Preparation of GBM Tumour spheroids and BBB-Spheroids

Different tumour spheroid (TS) compositions were tested as detailed below:

- Monoculture of U87.
- Monoculture of GBM-8.
- Coculture of U87 with microglia cells (HMC3, 30% and 50%).
- Coculture U87 (90%) and GMB-8 (10%), from now on referred to as "*Tumour Mix*."
- Coculture of Tumour Mix and HMC3s (30% and 50%)
- U87 (50%) and HASTR/ci35 (50%)
- U87 (70%) and remaining HASTR/ci35 (30%)
- Tumour Mix (70%) and HASTR/ci35 (30%)
- Tumour Mix (70%) and a coculture of HASTR/ci35 and HMC3 in a 1:1 ratio (referred as "Bio-Mix").

Blood Brain Barrier Spheroids (BBB-S) were created using three cell types that contribute to the structure of the BBB, i.e., endothelial cells, pericytes and astrocytes, with different ratios, as indicated below:

- Monoculture of HBEC-5i, referred as BBB-EC.
- Coculture of HBEC-5i (50%) and HBVPC/ci37 (50%), referred as BBB-EC-PC.
- Triculture of HBEC-5i, HASTR/ci35 and HBVPC/ci37, in a ratio of 1:1:1, referred to as BBB-BIO.

To form spheroids, cells were plated in a Corning® Costar® Ultra-Low Attachment Multiple 96-wells Plate (Merck) (4000 cells/well for TSs, 4500 cells/well for BBB-S). Plates were then incubated at 37°C for 4 days to allow the formation and growth of spheroids. **Figure 24** summarizes the key steps of the procedure for the preparation of BBB-S as an example.

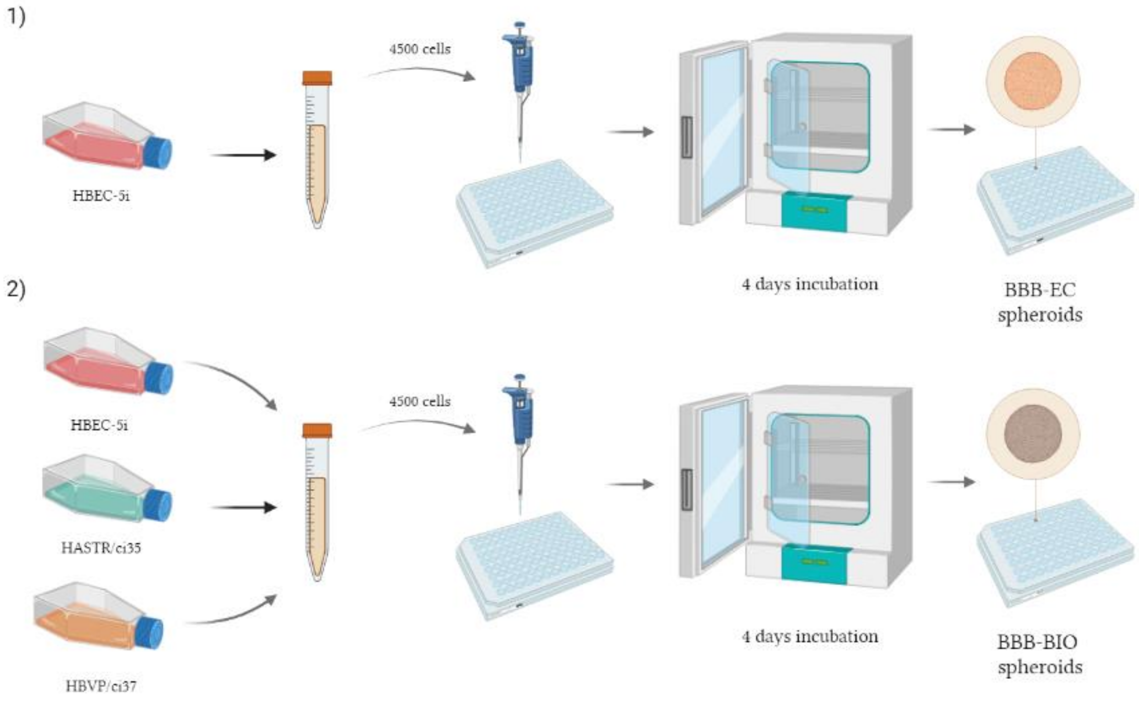

Figure 24: Preparation of BBB spheroids (BBB-S). Different protocols have been followed to obtain different compositions of spheroids. 1) Preparation of HBEC-5i monocultured spheroids (BBB-EC spheroids). 2) Preparation of BBB-BIO spheroids, with a ratio of 1:1:1 of HBEC-5i, HBVP/ci37 and HASTR/ci35. Image created with Biorender.com.

To form GBM-8 spheroids, a slightly different procedure was used. GBM-8 cells were first suspended by disaggregation of the free-floating spheres and pipetted in 96-well plates (8000 cell/well) and centrifuged at 1500 rpm for 5 minutes, using Centrifuge Z 446 K (Hermle, Labor Technik) with Mikrotitre rotor to obtain single spheroids. After 24 hours, the 96-wells plate was again centrifuged and left in the incubator for other three days, till complete formation of spheroids.

Qualitative analysis of spheroids morphology and cell distribution

To monitor the cell organization inside TS, two cell lines expressing green fluorescent protein (U87-GFP and GBM-8-GFP) were employed, while for the other cell lines, HASTR/ci35 and HMC3, the membrane was labelled using the commercial fluorescent membrane trackers, Vibrant™ DiD cell-labelling solution and Vybrant™ DiI cell-labelling solution (Molecular Probes, Inc), respectively. To label the membrane, cells were suspended at a density of 1 × 10^6/mL in proper culture medium, following by addition of 5 µL of the cell-labelling solution. Then, suspension is incubated at 37°C for 15 minutes and centrifuged at 1500 rpm for 5 minutes. The cell suspension was washed twice in culture medium before use.

Similarly, to study the organization of the three cell populations inside BBB-S, labelled-cells were used to form the spheroids. HVBPCs were labelled with Vybrant™ Dil cell-labelling solution while HASTR/ci35 were labelled using Vybrant™ DiD cell-labelling solution.

Before staining, culture medium was removed from TS and BBB-S. Secondly, 50 µl of 4% Paraformaldehyde (PFA) in Phosphate-Buffered Saline (PBS) (Alfa Aesar) were added to the wells to fix the samples. After a 20 min incubation at room temperature, PFA solution was removed from the wells and spheroids were rinsed twice in PBS for 5 minutes. These steps were performed under chemical fume hood. Then, 70 µl of a permeabilizing buffer (0.3% TritonX-100 in PBS) were added to the wells and incubated for 12 minutes, followed by two other rinsing steps in PBS.

For the BBB-S, the presence of tight junctions was verified by immunostaining with Anti-ZO1 antibody. Briefly, 50 µL of Thermo Scientific™ SuperBlock™ (PBS) Blocking Buffer were administered to the samples and incubated for 20 min. Primary Rabbit Recombinant Anti-ZO1 tight junction protein antibody (Abcam ab221547) was diluted at a ratio of 1:200 in the blocking buffer. After removing the blocking solution, 50 µL of antibody solution were dispensed into each well and the plate was incubated overnight at 4 °C. At the end of the incubation, the primary antibody was removed, and the BBB-S were rinsed three times with PBS. BBB-S were then incubated with 50 µL of the secondary antibody (Goat Anti-Rabbit IgG H&L Alexa Fluor® 555) (Abcam ab150078) in blocking solution (1:500) The plate was incubated for 2 h at room temperature in the dark and then washed twice with PBS.

For both BBB-S and TSs, cell nuclei were labelled by adding 70 µl of DAPI (4',6-Diamidino-2-Phenylindole, Dihydrochloride, Invitrogen™) solution. The plate was then incubated for 10 min at room temperature in the dark. This step was followed by two washing steps.

Images were acquired using a confocal spinning disk microscope (NikonECLIPSE Ti2) or a ZOE™ Fluorescent Cell Imager. The Z-stacking feature of the NIS-Elements Viewer was used on spheroids to reconstruct the lateral and frontal projections.

Drug treatment and cell viability assay

After their complete maturation, TSs were treated using BTZ in free form or at equivalent dose inside the NPs.

Spheroids of GBM-8, U87 and Bio-Mix were treated with 10, 20, 50 nM of BTZ-loaded NPs (BTZ-NPS) and free drug (BTZ), to compare the effect of the two treatment methods.

Higher concentrations (100, 200, and 500 nM) of BTZ-NPs were also administered to the following TSs:

- Monoculture of U87.
- Monoculture of GBM-8.
- Coculture of U87 and microglia cells (HMC3, 30% and 50%).
- *Tumour Mix*.
- Coculture of Tumour Mix and HMC3s (30% AND 50%).
- Bio-Mix.

Brightfield images were acquired for 3 days, every 24h, using a spinning disk microscope (Nikon ECLIPSE Ti2) or a ZOE™ Fluorescent Cell Imager.

Non-treated TS were used as controls. Cell viability after the treatment was assessed at different time points (24 h, 48 h, 72 h) using the CellTiter-Glo ® 3D Viability Assay (Promega), following the manufacturer instructions. Briefly, a volume of CellTiter-Glo ® 3D Reagent equal to the volume of cell culture medium present in each well of the 96-well plate was added. Then, plates were vigorously shaken for 5 minutes at 400 rpm protected from light using a Biometra TSC ThermoShaker to induce cell lysis. Spheroids were then transferred to a Thermo Scientific™ 96 Well White/Clear Bottom Plate and shaken to remove bubbles. Lastly, the luminescence signal was detected using a plate reader (Synergy™ HTX Multi-Mode Microplate Reader). The luminescence signal of each well is directly linked to cell viability, which was normalized to the untreated controls.

4.2.3 Hydrogel-based GBM models

Rheological characterization of Glioma extracellular matrix (G-ECM)-like hydrogel

To mimic the Glioma extracellular matrix (G-ECM), a collagen-I hydrogel (4mg/mL) was prepared by mixing the AMSbio Cultrex® 3D collagen I form rat tail (5 mg/mL, #3447-020-01) with 1 M HEPES (ThermoFisher 15630-122, pH 7.2-7.5) and 37 g/L NaHCO3 (Sigma S5761-500G), in 8:1:1 ratio. The mixture obtained was homogenized by pipetting several times in an ice bath and briefly spin down to remove air bubbles.

The mechanical properties of the G-ECM hydrogel were assessed via rheometer testing (Modular Compact Rheometer-MCR 302, Anton Paar), using a 25mm disk-plate geometry. For each analysis, 0.5mL samples were dispensed in the sol state (at 0 °C) on the lower plate of the rheometer. Once brought to the required temperature, the sol of Collagen-I was maintained in quiescent condition for a predefined time interval (15 minutes at a stable temperature) and finally tested. A strain sweep test was performed to identify the linear viscoelastic (LVE) region at constant frequency (1Hz) and temperature (37°C), by varying strain within a range of 0.01-500%.

Then, a Time Sweep Test was carried out to identify the crosslinking kinetics of collagen. The test was performed at 37 °C by applying a strain inside the LVE (0.1 %) with a constant frequency (1 Hz), for a total duration of 30 minutes.

Frequency sweep tests were performed at 37°C, 25°C, 15°C, 10°C and 4°C, keeping an angular frequency range of 0.1-100 rad/s and a strain of 0.1%. Storage modulus (G’) and loss modulus (G’’) measurements at 100 rad/s were compared between the different chosen temperatures.

GBM TSs embedding in G-ECM hydrogel.

Mature U87 spheroids (with U87 labelled with Vybrant™ Dil Cell-Labelling Solution), Tumour Mix spheroids (with U87-GFP and GBM-8-GFP) and Bio-Mix spheroids were prepared as described in Section 4.2.2 and embedded in a G-ECM gel solution in a 96 well plate in an ice bath. After the transfer, the 96-wells plate was placed in incubator at 37°C for at least 15 minutes to allow the gelification of the gels (example of procedure is shown in **Figure 25).**

To explore the role of microglia cells in supporting TSs invasion, Tumour Mix (with U87-GFP and GBM-8-GFP) were embedded in the hydrogel and HMC3 (labelled with Vybrant™ Dil Cell-Labelling Solution) (100 cells/µl, for a total volume of 10 µl per well) were embedded in the G-ECM gel.

Spheroids were treated with both free drug (BTZ) and BTZ-NPS at three concentrations (10, 50 and 200 nM) and monitored for 4 days, acquiring images every 24h. TSs were treated after 24h (48 h for U87 spheroids) post transfer, to let the spheroids adapt to the new culture conditions.

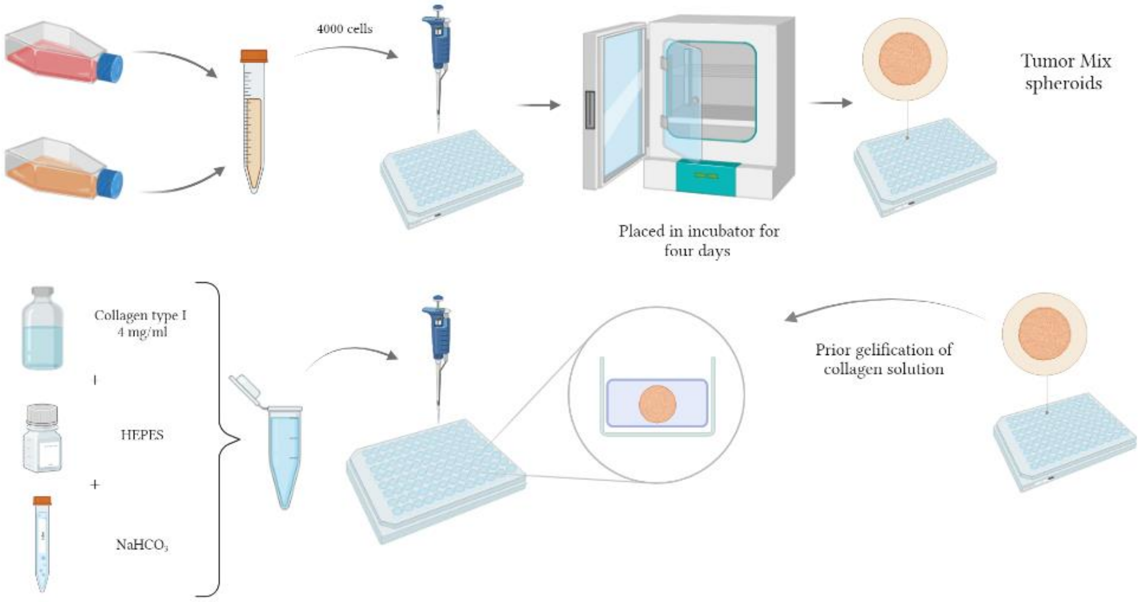

Figure 25: Schematic representation of the preparation of Tumour Mix spheroids and their embedding in G-ECM hydrogel. Image created with Biorender.com.

Evaluation of treatment efficacy in G-ECM hydrogel

Tumour Mix spheroids in G-ECM hydrogel and Tumour Mix spheroids in the same hydrogel embedding HMC3 were analysed to determine cell viability and invasion pattern through the hydrogel matrix, after treatment with BTZ-NPs or BTZ. Concentrations used for testing were of 10, 50 and 200 nM.

Specifically, the fluorescence intensity of GFP-expressing tumour cells was used as an indicator of cell viability. Spheroid viability was calculated by normalizing the GFP fluorescence intensity of the treated samples to the GFP fluorescence intensity of untreated controls. The fluorescence intensity was measured on images acquired on the median plane of the spheroids by the Nikon ECLIPSE Ti2 microscope as cumulative intensity on the region of interest.

Invasion patterns were assessed using the automatic ROI definition tool of the Nikon ECLIPSE Ti2 microscope. The tool allowed to delineate and measure the area of cells invasion using fluorescence images, comparing the invasive area to the area bordered by the spheroid mass, over time.

GBM TSs embedding in a Glycosaminoglycans (GAGs)-like hydrogel.

To determine the effect of hydrogel stiffness on the behaviour of TSs, Tumour Mix TSs were also embedded in a stiffer commercial polysaccharide-based hydrogel (VitroGel® 3D hydrogel solution, The Well Biosciences) with tuneable elastic modulus. This xeno-free gels can replicate the role of Glycosaminoglycans (GAGs), polysaccharides which are present in the ECM of glioblastoma and responsible for the high elastic modulus of the tumour tissue.

Tumour Mix Spheroids (with U87-GFP and GBM-8-GFP) were prepared as described in Section 4.2.2 and embedded in different concentrations of the VitroGel® Hydrogel System (TheWell Bioscience Inc.) to identify the dilution ratios that preserve the integrity of the tumour spheroids over time. The hydrogel was prepared according to the manufacturer's instructions, by first diluting the VitroGel 3D hydrogel solution with the provided Dilution Solution (Type 1) at different ratios, such as 1:3, 1:5, 1:10 and 1:20. The gel solution was poured in the wells of a multi-well plate and, prior to gelification, Tumour Mix spheroids were added. The plate wan then placed in the incubator at 37°C to allow gelification. Spheroids were visually checked every 24 hours for a total of 4 days through optical microscope (DMi1 Leica).

Using the dilution ratio of 1:3, tumour Mix spheroids were also used to obtain quantitative data on spheroid viability when undergoing treatment with BTZ-NPs or BTZ at three concentrations (10, 50 and 200 nM). The viability of the spheroids was determined as described before, using the GFP signal of the tumour cells as an indicator of cell viability.

Spheroids were monitored for 4 days, acquiring data from day 2 to day 4 every 24 hours. Images were acquired using a confocal microscope (Nikon ECLIPSE Ti2) every 24hours.

Assessment of microglia tumour homing capability

To investigate the ability of HMC3 to infiltrate GBM, Tumour Mix Spheroids embedded in the G-ECM gel were placed in the vicinity of HMC-3 cultured in the G-ECM gels, using two different experimental setups, as described in **Figure 26.**

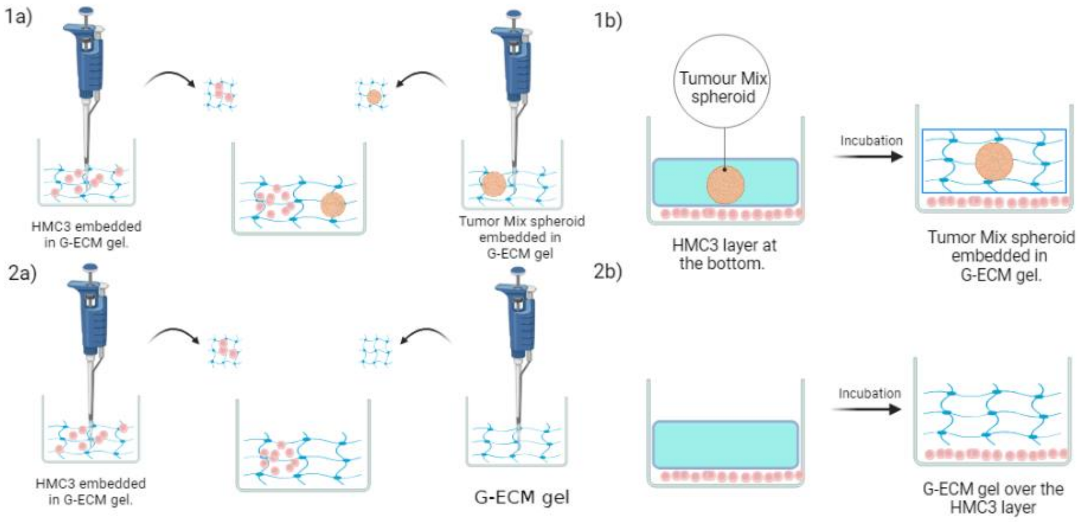

Figure 26: Schematic visual representation of the different steps needed to obtain the a) Interfacing-Gels (IG) and b) the Bottom-Gels (BG). Steps 1) show how to create the two Gels, embedding the Tumour Mix spheroids. Steps 2) show how create gels without the spheroids.

In detail, Tumour Mix spheroids were prepared as described above and embedded in 50 µL of the G-ECM gel. In a separate well, 25.000 or 50.000 HMC3 in 10 µl culture medium were mixed with the G-ECM gel solution The two separate gels, containing the tumour mix spheroid or the embedded HMC-3 were allowed to polymerize for 15 min at 37 °C. The two gels were then removed from their respective well, cut in two specular pieces using the tip of a micropipette, and combined in a clean well, so as to achieve an interfacing gel (IG-S) configuration, where one piece of the gel containing the HMC3 is placed in contact side by side with one piece of the gel containing the Tumour Mix. As control, the same process was performed using the HMC3-embedding gel in contact with an empty gel piece (without the tumour spheroid, IG).

Similarly, vertical migration was studied by creating a different setup. First, HMC3 cells were seeded (25.000 or 50.000 cells per wells) on the bottom of the wells and let adhere for 2 h. Then, the Collagen-I solution was poured on top. Prior to its gelification, Tumour Mix spheroids were added (Bottom-Gel with Spheroids, BG-S). As a control, the same procedure was followed but without the embedding of the Tumour Mix spheroid (BG). Confocal microscope images were acquired to assess the migration pathways. The presence of HMC3 cells nearby the spheroids was confirmed by imaging the plane corresponding to the centre of spheroids at different time point.

4.2.4 3D-Vascular *in vitro* model

Preliminary testing

The cell viability of the constituent cells of the BBB (i.e., HBEC-5i and of HVBP) within the collagen-based gel was assessed by seeding HBEC-5i, HVBPC and a mixture of the two (1:1) on top of the collagen solution, before collagen polymerization to embed the cells in the matrix, or after collagen polymerization, to allow cells to grow on top of the collagen matrix. Cells seeded in 2D culture on uncoated wells and on gelatin-coated (HBEC-5i) or collagen-coated (HVBP, 50HBEC-5i:50HVBP) wells were used as negative and positive controls respectively.

Cell viability was evaluated using the CellTiter® Blue assay (Promega), following the manufacturer instructions. The reagent solution was prepared by mixing Resazurin with culture medium, at a ratio of 1:6.

Culture medium was removed, and 100 µl of the reagent solution were added to each well. After an incubation of 3 hours at 37 °C, the reagent was collected in a black 96-wells plate, suitable for the fluorescence readings (Invitrogen™, Microplates for Fluorescence-based Assays, 96-well). Resorufin (and cell viability) was quantified by detecting the fluorescence emission at 560/590nm using a plate reader (Synergy™ HTX Multi-Mode Microplate Reader). As control, the reagent was added to bare wells, defined as "blank". The values of blank measurements were then subtracted from final values obtained.

After the removal of the reagent solution, cells in gel were washed once with 100 µl of PBS and 100 µl of fresh medium were added.

Thus, cell viability was monitored after 24h, 48h and 7 days, for the different culturing conditions. Results obtained from the 3D configuration were analysed both in terms of percentual increase of cell viability compared to the values obtained after 24 h and in terms of percentual increase of cell viability compared to the mean values obtained from the 2D-culturing conditions, for each cell lines.

Development of a microvascular network

To recreate an *in vitro* vascularized network, the MIMETAS Organo Plate® Graft Chip was employed. This microfluidic platform can be used to vascularize tissues, such as spheroids and organoids, following the administration of angiogenic factors to the graft chamber, which should promote angiogenic sprouts. The development of this device comprises three principal phases:

I. The formation of a vascular Network inside the chip.
II. The insertion of the tissue of choice.
III. The characterization of created vessel.
IV.

Firstly, the G-ECM solution was prepared by placing an Eppendorf tube on ice, to prevent gelification, and adding Collagen-I (5 mg/ml AMSbio Cultrex® 3D collagen I rat tail, 5 mg/mL, #3447-020-01), HEPES (1 M, ThermoFisher 15630-122, pH 7.2-7.5) and $NaHCO_3$ (37g/l, Sigma S5761-500G, pH 9.5) in 8:1:1 ratio. For each chip, 2.5 µl of G-ECM gel were dispensed in the gel inlet (column 2, **Figure 22**), by using an electronic pipette (eLINE® electronic pipette, Sartorius, #735021, previously #730021). Then, the OrganoPlate® was incubated for 15 minutes to allow complete gelification. To prevent the gel from drying, 50 µl of HBSS were added after the incubation, followed by another step in the incubator for 5 h.

After this step, endothelial cells (HBEC-5i) were seeded in the inlet of the lateral channels (10,000 cells/µL).

For the step of seeding, two different approaches were tested. In one case, cells were dispersed in culture medium mixed with 0,1% Gelatin (ATCC), (1:1ratio with culture medium). Otherwise, the channel was pre-coated with Collagen-I, followed by cell seeding.

For the channel coating procedure, 40 µL of collagen-I (0,125 mg/mL, AMSbio Cultrex®) were dispensed in each of the two perfusion inlets and then incubated at 37°C in a humified incubator for 1 h. After that, the coating solution was removed, and the channel was washed with 50 µL of PBS. For cell seeding, 2 µl (corresponding to 20000 cells/well) of cell suspension were injected in the perfusion inlet (for reference, columns 1 and 3 of chip showed in **Figure 22**). This step was followed by the injection of 50 µl of medium, in the same inlets, prior for 3 hours.

After the adhesion of cells, 50 µl of medium were also added to the perfusion medium outlet (columns 2, row B, **Figure 22**) and to the Graft chamber. Lastly, HBSS was removed from all wells.

After these passages, the OrganoPlate® was put on dynamic culture in the MIMETAS Rocker in a humified incubator, with an inclination of 14°, which was switched every 8 minutes.

For an optimal vessel maturation, medium was refreshed every 2-3 days by replacing the medium from medium inlets and outlets (50 µl each).

After the formation of vessels (about 5 days), a mixture of angiogenic factors (50 µl, prepared as described in Table 1) was added to the graft chamber to promote angiogenic sprouting.

Prior to the injection of the cocktail, the medium was removed from all wells of the OrganoPlate® Graft. The injection of the cocktail was immediately followed by the injection of medium without the factors in all perfusion inlets and outlets. Finally, the plate was put on the MIMETAS Rocker in incubator to continue culture until completed vessels maturation and beginning of sprouting.

Once a complete and dense vessel network was identified, Tumour Mix spheroids were placed and cultured in the graft chamber. First, endothelial cells culture media was removed from the Graft chamber, and from perfusion inlet and outlet. The spheroids prepared as described in **4.2.2,** were placed using p200 pipettes with wide bore tips. Then, 5 µl of G-ECM solution were added, to embed the spheroid. After a 15 min incubation at 37°C, 50 µl of tissue specific media were added to the Graft Chamber. The plate was put in a humified incubator under dynamic flow, as described before. Chip development was monitored using Bio-Rad ZOE™ Fluorescent Cell Imager and a confocal microscope, a Nikon ECLIPSE Ti2 inverted microscope.

Immunostaining

The immunostaining protocol was optimized from the procedure suggested by MIMETAS. After having removed the medium from all chips, 50 µL 4% PFA in PBS (Alfa Aesar) were added to the graft chamber, inlets, and outlets. Chips were rinsed 3 times for 5 min by adding 50 µL of PBS in the graft chamber, inlets, and outlets. Cells were permeabilized for 10 min using 0.3% TritonX-100 in PBS (50 µL to each well). After another washing step, 50 µL of Thermo ScientificTM SuperBlock™ (PBS) were added to the graft chamber, inlets, and outlets, and incubated for 45 minutes. Primary antibodies were diluted in the blocking buffer (1:500). For this study, Recombinant Anti-ZO1 tight junction protein antibody (rabbit monoclonal antibody, Abcam ab221547) and Recombinant Anti-CD31 antibody (rabbit monoclonal antibody, Abcam ab76533) were used. Once the blocking solution was removed, 20 µL of the antibody solution were injected into inlets and outlets and in the graft chamber and incubated overnight at 4 °C. The primary antibody solution was then aspirated, and the washing step was repeated three times.

The secondary antibody (Goat Anti-Rabbit IgG H&L Alexa Fluor® 555, Abcam ab150078) was diluted in the blocking solution (1:200) and dispensed to the chip (20 µL) in the graft chamber and incubated for 2 h at room temperature, protected from light. After three further washing steps (PBS), cells were stained with 4’,6-Diamidino-2-Phenylindole (DAPI) for 15 min. Images were acquired using Nikon ECLIPSE Ti2 inverted microscope. All incubation steps were performed under dynamic conditions using the OrganoFlow® with an inclination angle of 5° and a switching interval of 2 min.

Assessment of NPs permeability and HMC3 extravasation

To study extravasation through the obtained vessels, five days after administration of the Pro-angiogenic factors, 50µL of Rhodamine-labelled NPs (prepared as described in section **4.2.1**) in HBEC-5i culture medium (1mg/mL) were injected in the perfusion inlets. Images were acquired 3h after injection using a confocal microscope (Nikon ECLIPSE Ti2).

Similarly, extravasation of HMC3 was studied by first labelling cells with Vybrant™ Dil and followed by cell injection in the perfusion inlet (50.000 cells/inlet).

The HMC3 suspension was also injected into some of the MIMETAS chip hosting tumour spheroids, to compare infiltration in the presence of tumour with the tumour-free conditions. After the injection of HMC3 cells, images were acquired after 3 hours and after 7 days using the Nikon ECLIPSE Ti2 inverted microscope.

4.2.5 Statistical analysis

Results are reported as mean ± standard deviation. The size of the sample population (n) is specified in the corresponding section of the results. Statistical analysis was performed with GraphPad Prism software (GraphPad, San Diego, CA). One or Two-way ANOVA analysis with a 95% confidence interval was used for comparisons.

5 Results and discussion

5.1 NPs preparation and characterization

Both empty and BTZ-loaded NPs (BTZ-NPs) were successfully obtained through nanoprecipitation. The hydrodynamic diameter measured through DLS, reported in **Figure 27**, **A**, shows a slight and not significant increase in the NPs size, after encapsulation of BTZ, with size varying from 139 ± 28 nm for empty NP to 157 ± 14 nm for BTZ-NPs. A slight increase in particles size after drug loading was also observed by other authors and is generally considered an indication of successful drug encapsulation. [104]

The polydispersity index (PDI), which is an indicator of the homogeneity of NPs dispersions, was extremely low (11±1%) for the empty NPs, indicating a well monodispersed suspension, with a non-significant increase for BTZ-NPs (20 ± 7%), as depicted in **Figure 27, a**.

The Z-potential values represented in **Figure 27,b** show that NPs and BTZ-NPs possessed a negative surface charge, which can promote NPs internalization by endocytosis. [105] Moreover, the high absolute value of surface charge is an indicator of the stability of the formulation since particles repulsion is expected to reduce the formation of aggregates [106]. BTZ-NPs displayed a less negative value of Zeta Potential, which might be attributed to the presence of drug near the surface of the NPs (**Figure 27,b**).

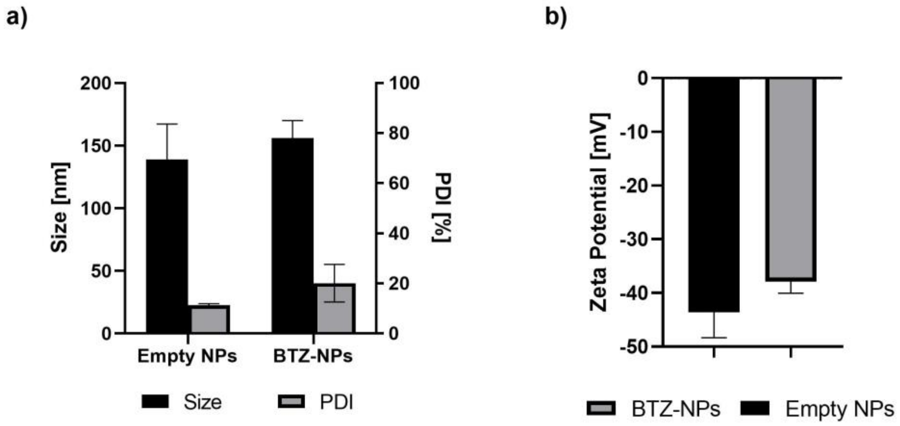

Figure 27: a) Hydrodynamic diameter and polydispersity index (PDI) for empty NPs and BTZ-NPs (n=3); b) Zeta potential (mV) for empty NPs and BTZ-NPs. (n=3).

The drug encapsulation efficiency (EE) determined by UV spectroscopy was 11+2%, comparable with the values obtained in other detections made by the group by high-performance liquid chromatography (HPLC, EE~10%) technique. The obtained EE is similar but slightly lower than values reported by other authors, using nanocomplexation, for which an EE of 15% was reported. [107]

Drug release kinetics are shown in **Figure 28.** Following an initial burst release in the first 24 hours, the NPs were able to support a sustained release over time (reaching approximately an 80% release after 7 days), compatible with a prolonged treatment. The results suggest that BTZ in the surface layers of the NPs can diffuse in the first hours, accounting for the observed burst release, while the drug encapsulated in the polymeric core is released at a slower pace. This release profile may result in more favourable drug administration, since a prolonged release may strongly reduce undesired side effects. [107]

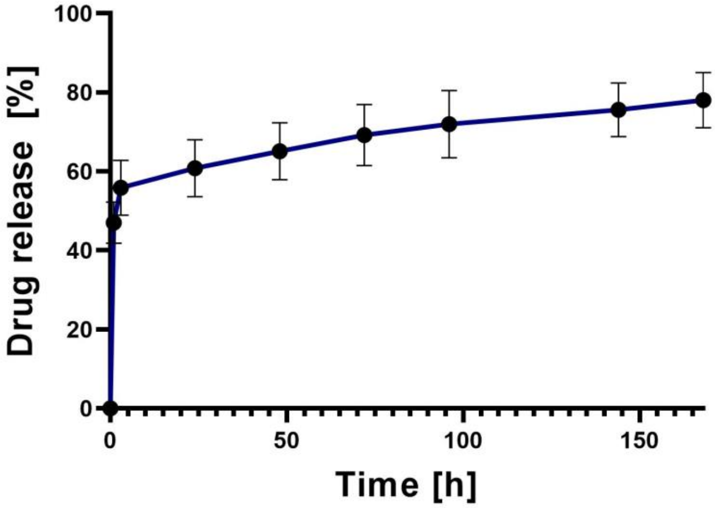

Figure 28: Drug release kinetics, over 168 h observation, for BTZ-NPs in water (n=3).

5.2 Spheroid-based GBM models

Preparation of the different multicellular spheroid models

Many studies suggested that microglia play a key role in tumour progression and invasion, although the effects on the response of GBM to cytotoxins must still be investigated.[108] Therefore, TS comprising different ratios (70:30 and 50:50) of HMC3 were prepared, in combination with either U87 alone (**Figure 29**), or the tumour mix (**Figure 30**). These different compositions were selected to replicate the histological composition of human GBM. Indeed, literature data reported that tumour-associated microglia comprise from 35 to 50% of the GBM mass [101].

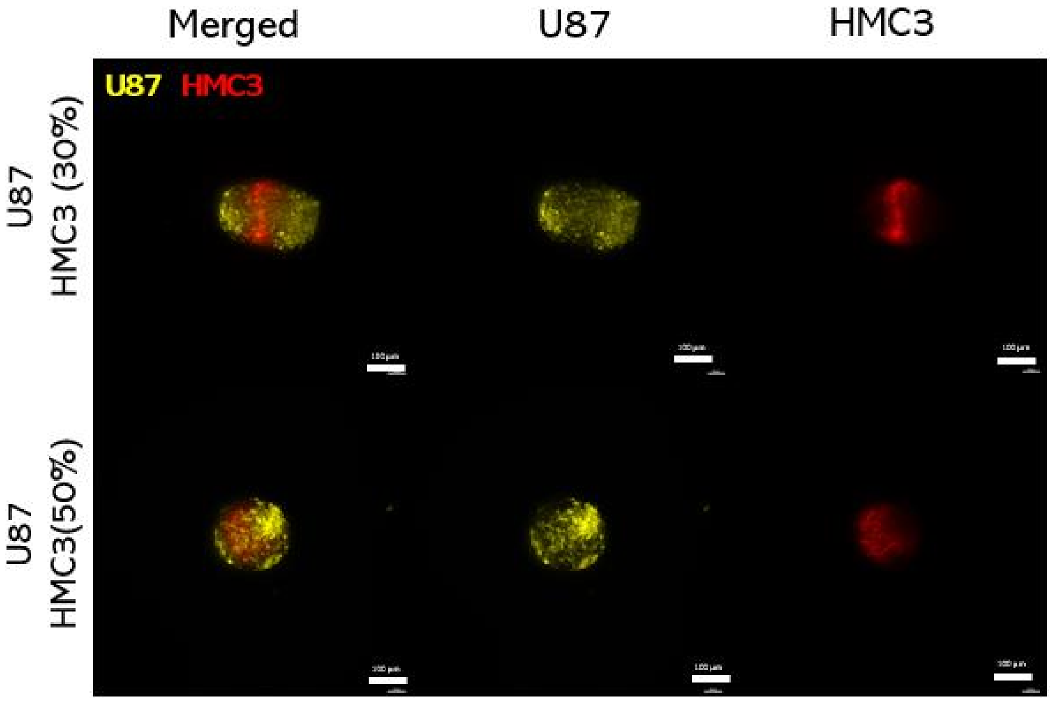

Figure 29: Fluorescence imaging of the U87 spheroid and U87 spheroids comprising different ratios (30 and 50) of HMC3. U87 cells (labelled with Vybrant™ Dil Cell-Labelling Solution) are shown in yellow, while HMC3 are shown in red (labelled with Vybrant™ DiD Labelling Solution). Scale bar=100 µm.

As shown in **Figure 29**, HMC3 localized mostly in the inner core of U87 spheroids, regardless of their initial ratio.

Tumour mix spheroids containing both U87 and GBM-8 (90:10) were successfully obtained, as shown in **Figure 30**. The selected ratio replicates the human GBM composition, where the majority of the mass is composed by differentiated tumour cells and only a small portion is represented by GSCs [35]. In the Tumour Mix spheroids, GBM-8 cells (in green) localize in the periphery of the spheroid, mimicking the invasive niches, characteristic of GBM [37].

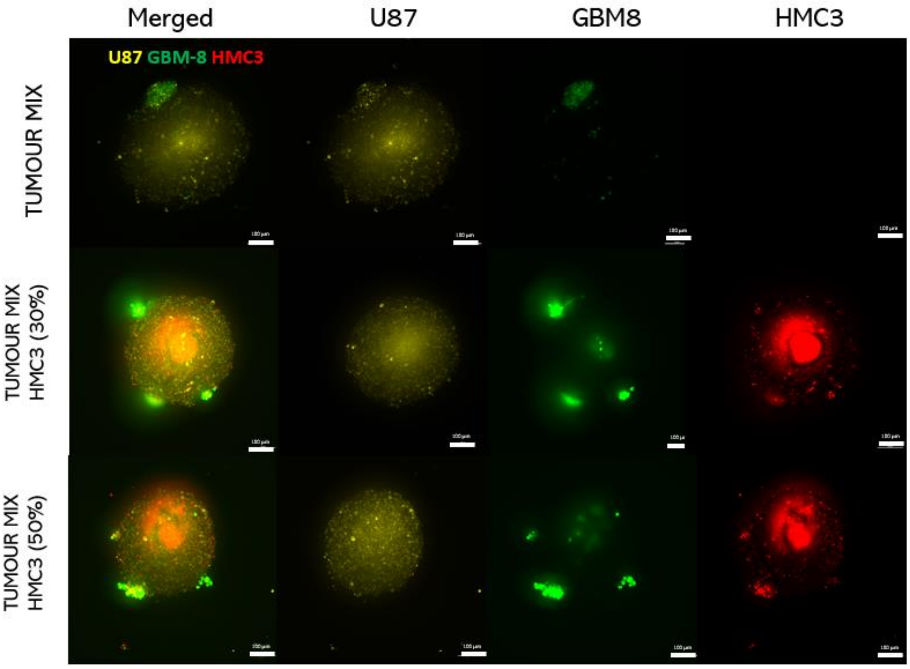

Figure 30: Fluorescence imaging of the Tumour Mix spheroid and Tumour Mix spheroids comprising different ratios (30 and 50) of HMC3. U87 cells (labelled with Vybrant™ Dil Cell-Labelling Solution) are shown in yellow, GFP-labelled GBM-8 are shown in green, while HMC3 are shown in red (labelled with Vybrant™ DiD Labelling Solution). Scale bar=100 µm.

For Tumour Mix spheroids with HMC3 cells, GBM-8 cells accumulated in the inner area and in the peripheral areas of the spheroid, resembling the hypoxic and invasive niches of GBM.

This organization of GBM-8 cells in niches-like clusters was also stable over time, as confirmed by the images collected in **Figure 31**. The images confirmed the presence of fluorescence areas of GBM-8 cells in all spheroids, proving that these models allow the formation of stem cells niches, as observed *in vivo*. The different localization of these niches appears evident from **Figure 31**, depending on the compositions of spheroids. Indeed, in Tumour Mix spheroids, niches were mostly in the peripheral areas near the more invasive *Tumour border regions,* and very few in the inner part. On the other hand, with the addition of microglia (50%) more niches could be observed in the inner part of the spheroids, similar to the *hypoxic/necrotic* niches. [37] Tumour Mix spheroids with 30% microglia showed an intermediate behaviour with smaller niches but distributed both in the inner part and in the peripheral regions of the spheroids, resembling a more physiological *in-vivo* tumour mass. These findings suggest how this composition, which includes both GSCs and HMC3, could recreate a more reliable *in vitro* model of GBM, in terms of composition and also in terms of spatial configuration of cells, crucial elements in determining response to drug treatment [102].

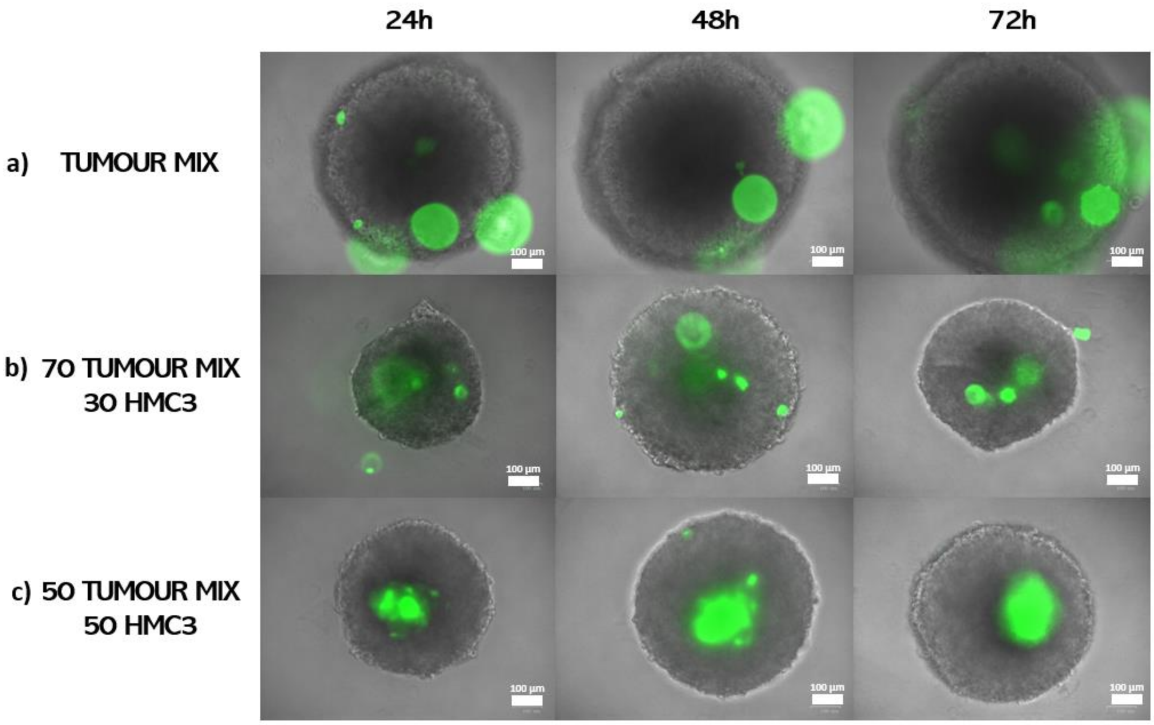

Figure 31: Merge images of brightfield and greenfield of a) Tumour Mix spheroids and b) 70:30 c) 50:50 Tumour Mix/HMC3 spheroids. Images were acquired 24, 48h and 72h after the formation of spheroids, without performing any treatment. Green fluorescence indicates the GFP-GBM-8 cells. Scale bar= 100 µm.

TS containing HASTR/ci35 (50% or 30%) were then prepared using U87 or the Tumour Mix and the distribution of this cell type within the spheroid was investigated.

As shown in Figure 32, astrocytes can be successfully integrated inside U87 spheroids and mostly tended to accumulate in the inner zones, surrounded by tumour cells, with very few cells in the outer zones, similar to what observed for HMC3.

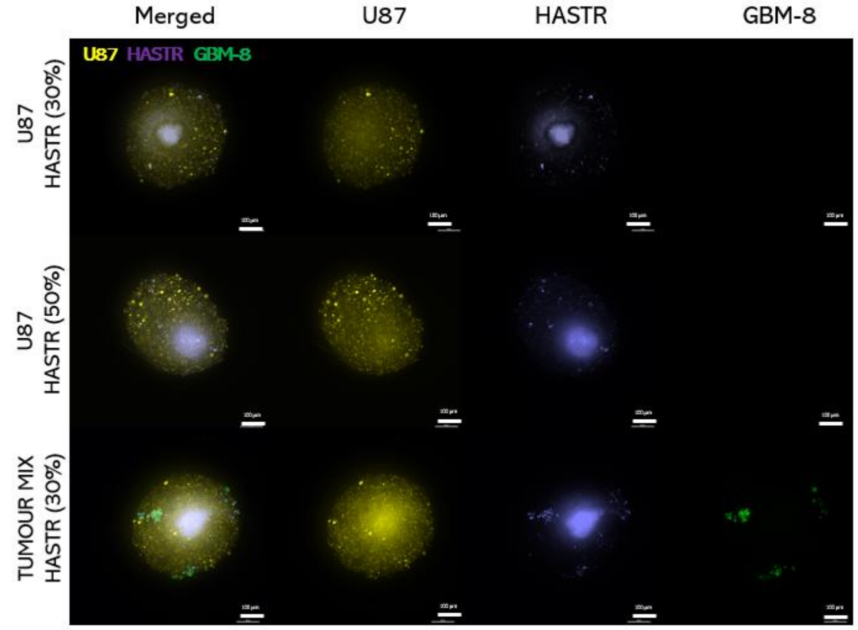

Figure 32: Fluorescence imaging of the U87 spheroid and Tumour Mix spheroids comprising different ratios (30 and 50) of HASTR. U87 cells (labelled with Vybrant™ Dil Cell-Labelling Solution) are shown in yellow, GFP-labelled GBM-8 are shown in green, while HASTR are shown in violet (labelled with Vybrant™ DiD Labelling Solution). Scale bar=100 µm.

In Tumour Mix spheroids, astrocytes localized in the inner part of the spheroid (Figure 32), with GBM-8 forming small cluster, similar to invasive and peri necrotic tumour niches, surrounded by U87 cells (in yellow).

To investigate the effect of microglia, BIO-MIX spheroids, composed by 30% of a mix of HASTR and HMC3 (1:1) and by 70% of the Tumour Mix were used. This better replicates the microenvironment of GBM, which is composed of different cell types, such as tumour cells, GSCs, microglia, and astrocytes. Moreover, the intercellular communication among these cells is known to impact on the tumour behaviour. [34]

As shown in **Figure** 33, astrocytes localized in the inner area of the spheroid. Similarly, HMC3 cells accumulated in the inner parts. On the other hand, GBM-8 cells formed niches in the peripheral area, resembling the invasive niches in GBM. This analysis demonstrated how overall this composition assumed a biomimetic morphology.

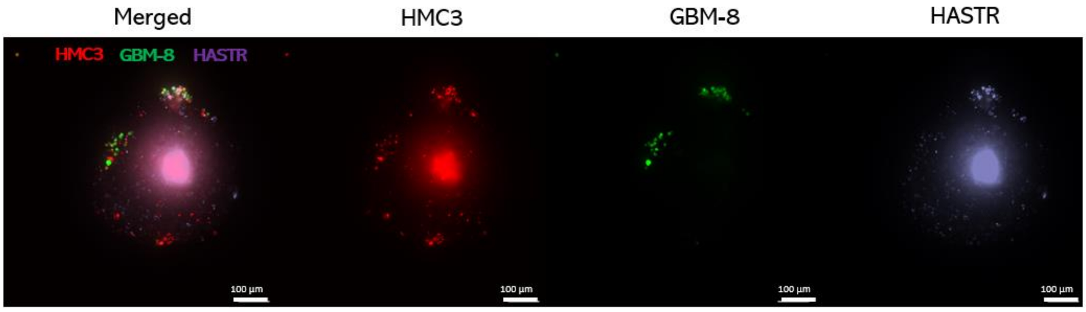

Figure 33: Fluorescence imaging of the Bio Mix spheroids. HMC3 cells (labelled with Vybrant™ Dil Cell-Labelling Solution) are shown in red, GFP-labelled GBM-8 are shown in green, while HASTR are shown in violet (labelled with Vybrant™ DiD Labelling Solution). Scale bar=100 µm.

Drug response of the tumour spheroids

Figure 34 and **Figure 35**, show the cell viability of U87 spheroids and GBM-8 spheroids after treatment with BTZ or BTZ-NPs at different timepoints. Results show that U87 spheroids were overall more resistant to BTZ than GBM-8 ones, when treated with either, BTZ or BTZ-NPs. Furthermore, considering the same concentration and incubation time, BTZ induced a higher decrease in cell viability, compared to BTZ-NPs. This difference can be attributed to the release profile of BTZ-NP (see **Figure 28**), which gradually released BTZ overtime. Low concentrations of BTZ-NPs did not produce a significant reduction of cell viability over time for both cell lines, with a more evident response to BTZ-NPs treatment achieved with a concentration of 50 nM, more evident for GBM-8 spheroids.

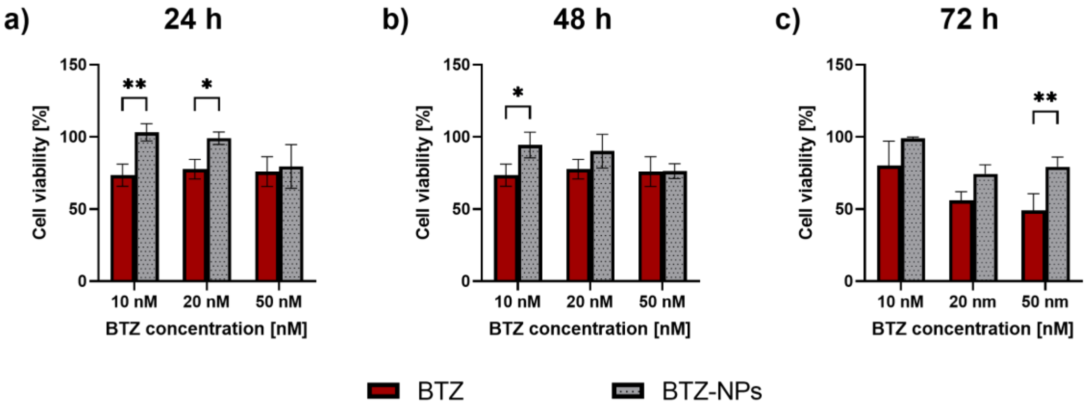

Figure 34: Cell viability of U87 spheroids treated with BTZ and BTZ-NPs at different concentrations and different time points: a) 24h, b) 48h and c) 72h. Multiple comparisons were performed using two-way ANOVA. *p<0.05, **p<0.01, ***p<0.001, ****p<0.0001.

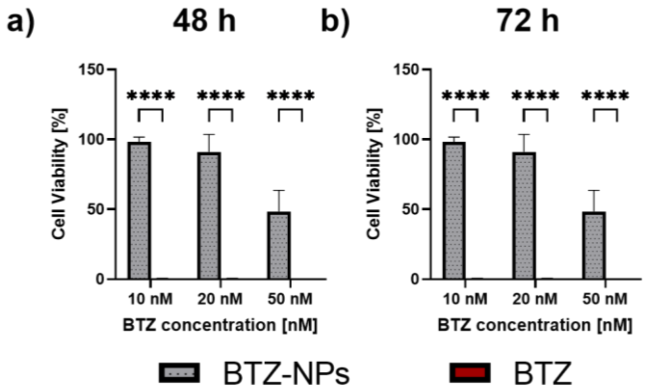

Figure 35: Cell viability of GBM-8 spheroids treated with BTZ and BTZ-NPs at different concentrations and different time points: a) 48h and b) 72h. Multiple comparisons were performed using two-way ANOVA. *p<0.05, **p<0.01, ***p<0.001, ****p<0.0001.

These tests suggested that higher concentrations of BTZ-NPs should be adopted to produce a comparable therapeutic effect to the one exerted by BTZ. Therefore, subsequent analyses were conducted at higher concentration of BTZ-NPs (100 nM, 200 nM, 500 nM) on spheroids of U87, GBM-8, and the Tumour Mix.

Figure 36 shows the morphology of U87 spheroids after treatment with BTZ-NPs at higher concentrations.

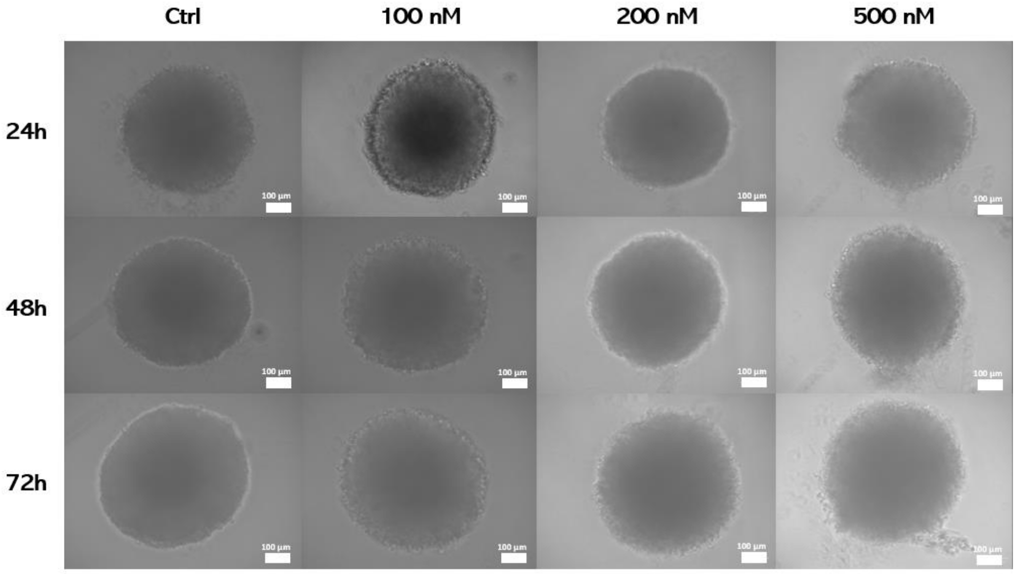

Figure 36: Bright field images of U87 spheroids, treated with different concentrations of BTZ-NPs (100 nM, 200 nM, and 500 nM). Images were acquired at different time points (24, 48, and 72h). Scale bar= 100µm.

Compared to untreated controls, U87 spheroids treated with BTZ NPs slightly lost compactness at the edges, which was more evident with increasing incubation time and BTZ-NPs concentration. Reduction in spheroid size and loss of integrity was observed for high NPs concentrations, suggesting that BTZ NPs are effective against U87 spheroids at concentrations above 50 nM, by reducing their physical integrity.

Brightfield images of GBM-8 spheroids treated with BTZ-NPs are reported in **Figure 37**.

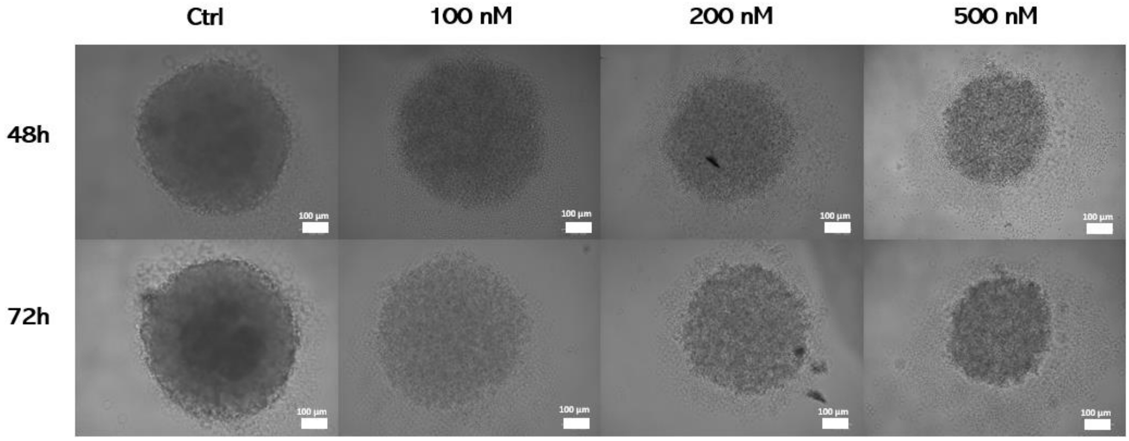

Figure 37: Bright field images of GBM-8 spheroids, treated with different concentrations of BTZ-NPs (100 nM, 200 nM, and 500 nM). Images were acquired at different time points (48 and 72h). Scale bars= 100µm.

GBM-8 spheroids begin to lose compactness at concentrations of 100 nM, after 48h. This same behaviour was observed also at the 72 h timepoint. When treated with concentrations over 200nM cell detachment and a marked reduction of spheroid size was observed.

Brightfield images of Tumour Mix spheroids after treatment with BTZ-NPs are reported in **Figure 38.**

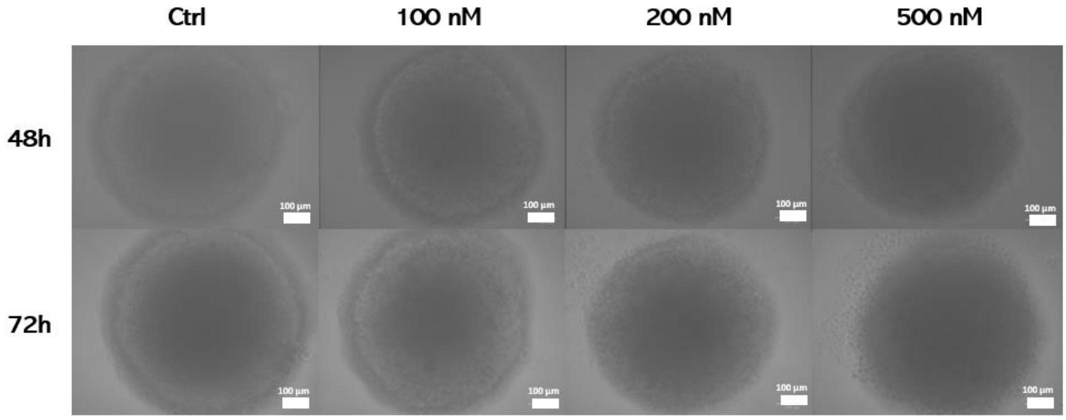

Figure 38: Bright field images of Tumour Mix spheroids, treated with different concentrations of BTZ-NPs (100 nM, 200 nM, and 500 nM). Images were acquired at different time points (48 and 72h). Scale bar= 100µm.

Spheroids began to lose compactness at the edges when treated with higher concentrations (>200nM), more evidently for longer periods of treatment (72h). No decrease in size was noted.

Cell viability quantification, shown in **Figure 39** confirmed that U87 spheroids were overall more resistant, for all tested concentrations of BTZ-NPs.

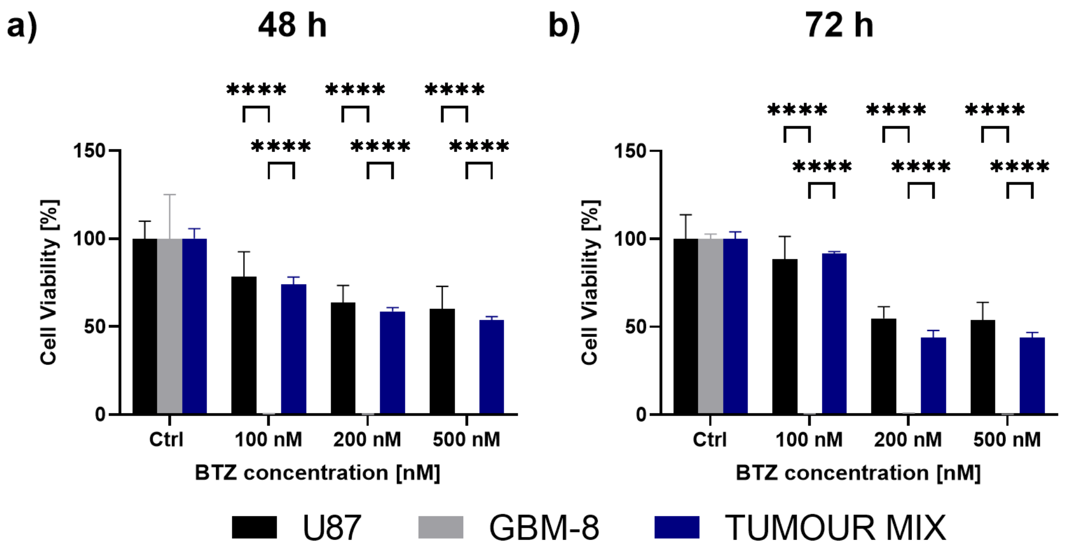

Figure 39: Cell viability of U87, GBM-8, and tumour mix spheroids, after BTZ-NPs treatment measured after a) 48h and b) 72h of treatment. Multiple comparisons were performed using two-way ANOVA. *p<0.05, **p<0.01, ***p<0.001, ****p<0.0001.

However, cell viability significantly decreased over time for the highest concentration of BTZ-NPs (500nM), reaching 65%. On the other hand, GBM-8 spheroids were extremely sensitive to treatment with BTZ-NPs, even at the lowest concentrations. A drastic reduction in cell viability was observed after 48h treatment with 100 nM BTZ NPS, with cell viability decreasing to around 0,5%. Results also indicated how the addition of GBM-8 cells to differentiated tumour cells did not seem to change their response to treatment. Since no significant differences between the behaviour of Tumour Mix and U87 spheroids were observed over time, the results seemed to suggest that there was no GSCs-mediated chemoresistance for the time points considered. This evidence might seem in contrast with general knowledge on GBM, as GSCs are commonly considered the major responsible for chemoresistance [102]. However, chemoresistance normally emerges over longer periods of treatment and it is normally induced by the interaction between GSCs and other extrinsic factors [109]. In fact, although the 3D configuration of spheroids is a much more reliable model compared to 2D cell culture, the model still lacks some essential features, such as the influence of the GBM-ECM or the interplay with non-tumour cells [11].

However, the significant difference in cell viability after treatment between GBM-8 and TM spheroids hinted that U87 cells might play a role of protection on GBM-8 cells, when in a 3D configuration, highlighting the importance of the spheroid models.

Inclusion of HMC3 in TS

When adding microglia to U87 spheroids, results (**Figure 40**) indicate that cell viability decreased considerably over time and by increasing BTZ concentrations, regardless of the amount of microglia added to the spheroid composition. After 72 hours of treatment with BTZ-NPs (500 nM), the viability of spheroids with HMC-3 decrease to 20%, regardless of the HMC-3 concentration.

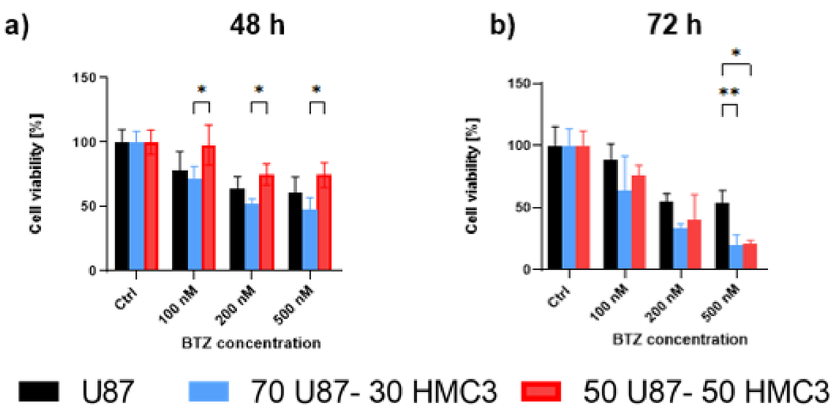

Figure 40: Cell viability of U87 spheroids, and U87 spheroids containing HMC3 (30% or 50%) after treatment with BTZ-NPs measured after a) 48 h and b) 72 h of treatment (n=3). Multiple comparisons were performed using two-way ANOVA. *p<0.05, **p<0.01, ***p<0.001, ****p<0.0001.

U87 spheroids were more resistant to drug treatment compared to the other spheroids, reaching, a viability of 48 ± 12% after 72 hours treatment with the highest concentration of BTZ-NPs. These results are supported by available literature, as U87 cells are more resilient to the treatment than HMC3 cells. [110]

Cell viability assay was then assessed on Tumour Mix spheroids comprising HMC3 in different ratios (70:30 and 50:50) after treatment with BTZ-NPs (**Figure** 41). Results indicate an increase of treatment efficacy, with increasing BTZ-NPs concentration. Interestingly, this decreasing trend was more evident for spheroid with HMC3 than for Tumour Mix spheroids. Spheroids with both GBM-8 and HMC3 seemed to be more affected by treatment. Indeed, after 72h of treatment at the highest BTZ-NPs concentration, cell viability values decrease to 24% for the composition with 30% HMC3 and to 8% with 50% HMC3. However, no significant differences could be noticed between the two ratios of HMC3 selected for the test.

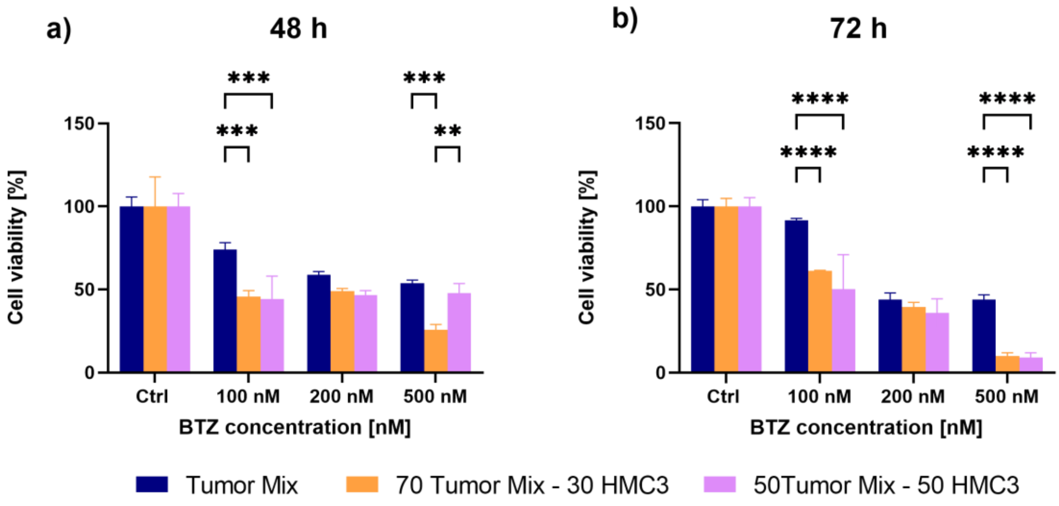

Figure 41: Cell viability of Tumour Mix spheroids, and Tumour Mix spheroids containing HMC3 (30% or 50%) after treatment with BTZ-NPs measured after a) 48 h and b) 72 h of treatment (n=3).

Multiple comparisons were performed using two-way ANOVA. *p<0.05, **p<0.01, ***p<0.001, ****p<0.0001.

Drug response of BIOMIX spheroids.

Figure 42 shows the response to BTZ and BTZ-NPS of the BIO-MIX spheroids. This configuration did not particularly suffer the BTZ-NPs insult, since no appreciable differences could be observed as compared to untreated spheroids. On the other hand, the highest concentrations of BTZ resulted in a decrease in tumour size. Moreover, 50nM-FD-treated spheroids, for all time points, seemed to lose compactness at the edges.

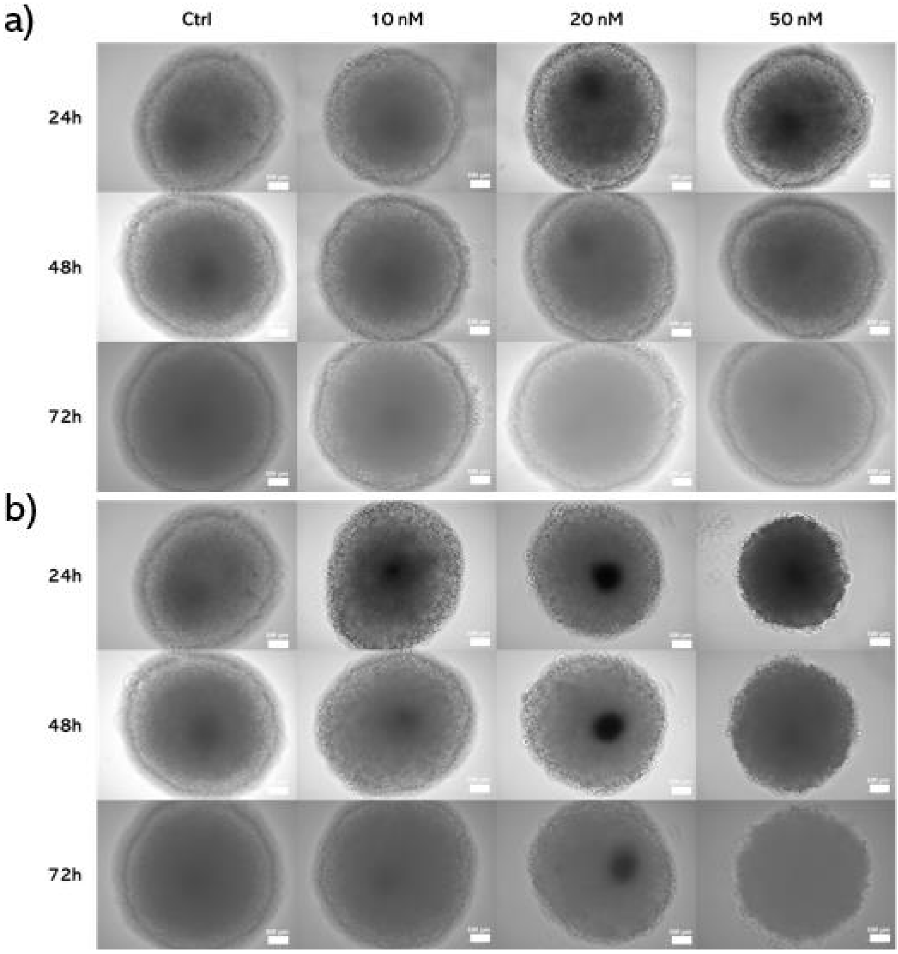

Figure 42: Bright field images of BIO-MIX spheroids, treated with different concentrations of a) BTZ-NPs and b) free BTZ (10 nM, 20 nM, and 00 nM). Images were acquired at different time points (24, 48, and 72h). Scale bar= 100µm.

This was confirmed by cell viability measurements (Figure 43).

Figure 43 shows how BIO-MIX spheroids were overall more sensitive to free BTZ treatment than BTZ-NPs for all time points. However, BTZ treatment did not produce a drastic cell viability reduction observed for other types of spheroids at BTZ concentrations below 20 nM.

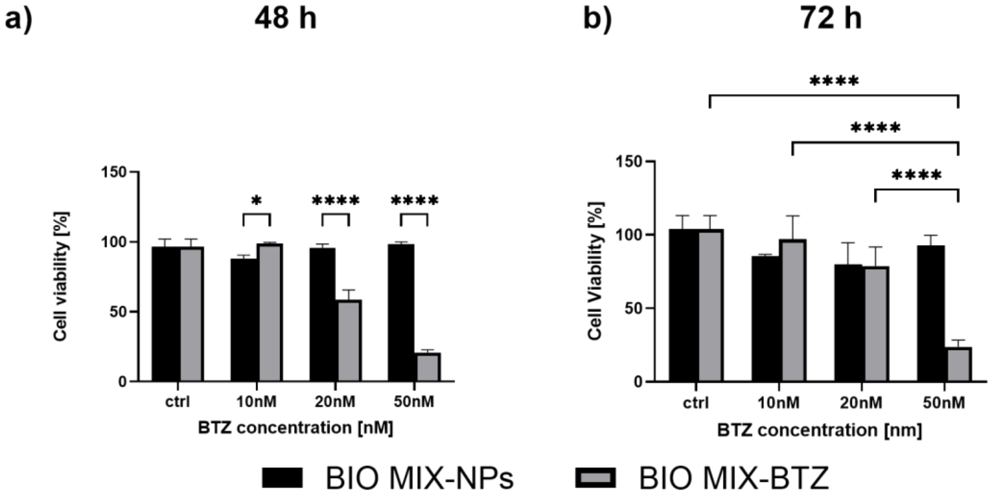

Figure 43: Cell viability of BIO-MIX spheroids treated with BTZ and BTZ-NPs at different concentrations and different time points: a) 48h and b) 72h. Multiple comparisons were performed using two-way ANOVA. *p<0.05, **p<0.01, ***p<0.001, ****p<0.0001.

Based on these results we also investigated the response to BTZ-NPs treatment with higher concentrations. The BIO MIX spheroids were not particularly sensitive even to higher concentrations of BTZ-NPs. Only when adopting a 500 nM concentration of drug there was a higher (not significant) decrease in cell viability, with a residual viability of 78%, after 72h of treatment (**Figure** 44**)**.

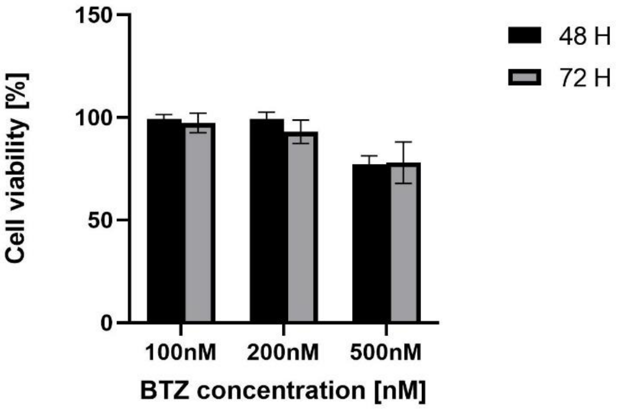

Figure 44: Cell viability of BIO-MIX spheroids treated with BTZ-NPs at different concentrations (100, 200 and 500 nM) after 48 and 72h. Multiple comparisons were performed using two-way ANOVA. *p<0.05, **p<0.01, ***p<0.001, ****p<0.0001.

The graph in **Figure 45** provides a comparison between the cell viability of the BIO MIX spheroids and the Tumour Mix spheroids, treated with the same concentrations of BTZ-NPs. Indeed, after treatment for 72h with a 200 nM concentration, the BIO-MIX spheroids showed a cell viability of around 92 ± 6 %, while the viability of the Tumour Mix spheroids was significantly lower, at 44 ± 4 %. At the 500 nM concentration, the viability of the BIO-MIX spheroid reached 78 ± 10 %, significantly higher than the value obtained for Tumour Mix spheroids (44 ± 3%) (**Figure** 45).

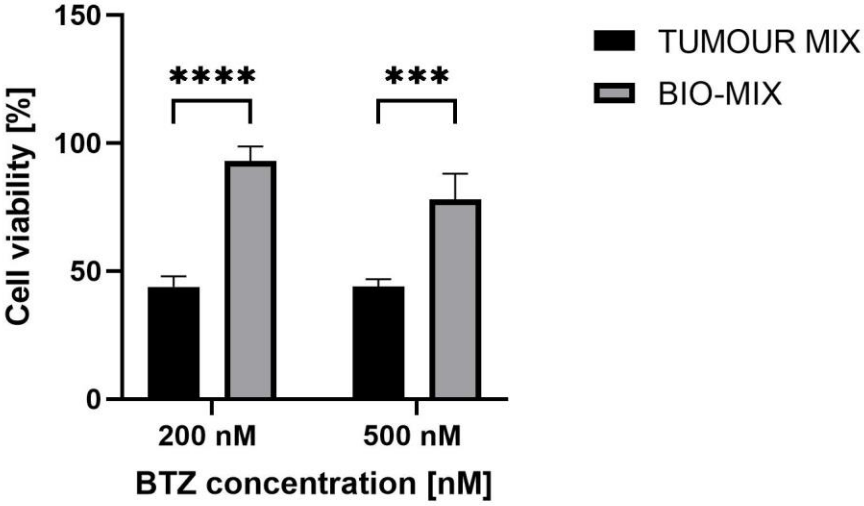

Figure 45: Cell viability of Tumour mix and BIO-MIX spheroids, after BTZ-NPs treatment measured after 72h of treatment. Multiple comparisons were performed using two-way ANOVA. *p<0.05, **p<0.01, ***p<0.001, ****p<0.0001.

Regarding the free drug, an opposite behaviour was observed (**Figure** *43***)**. The free drug treatment, led to sensibly lower values of cell viability for all concentrations considered. Considering that the BIO-MIX composition was chosen to be more physiological, and includes normal cells in the brain parenchyma (such as astrocytes and microglia), this result may indicate possible undesired toxicity of the free BTZ treatment. This aspect can be considered as a proof of the importance that BTZ should not be administered in the free form, but rather encapsulated in NPs or other carriers, to better target the tumour mass. Indeed, the outcome of phase II clinical trial using BTZ in patients with recurrent malignant glioma was not promising, most likely due to low bioavailability of BTZ and to its poor BBB penetration. Therefore, exploiting an advanced targeted BTZ delivery system to glioma cells might pave the way for its future clinical application. [98]

5.3 Hydrogel-based GBM models

Rheological characterization of G-ECM hydrogel

The G-ECM hydrogel (i.e., the Collagen-I gel described in section 4.2.3) was rheologically characterized by performing different test. Firstly, the strain sweep test allowed to identify the linear viscoelastic region (LVE), in which the storage modulus G’ and the loss module G’’ are independent from the applied strain (this region is identified in **Figure 46** by a black dotted line). Both systems behaved like a viscoelastic solid in the LVE range, and like a sol, outside this this region.

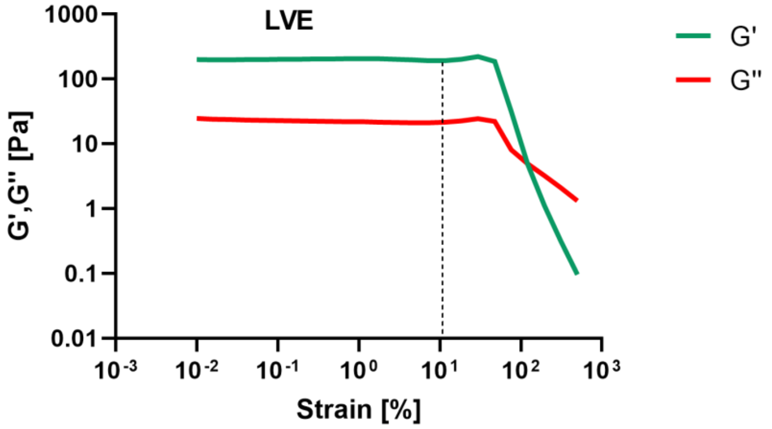

Figure 46: Strain sweep test on G-ECM hydrogel, performed at constant temperature of 37°C. The frequency was set at 1 Hz (1rad/s), and the strain was varied in the range 0.01-500%. LVE region is identified as the region in which both G' and G'' are stable delimitated by the dotted line.

A *Temperature Sweep test* was performed to identify the gelation time at 37 °C, which was then employed in subsequent tests. As shown in **Figure 47**, the value of G' start to increase notably after ~100 s, until it settles at a higher plateau after 7 minutes. The corresponding value of viscosity (ƞ) is 168 Pa·s, while the starting values were 1 Pa·s. This test confirmed that the incubation time of 15 min at 37°C was sufficient to guarantee the gelation of the G-ECM hydrogel.

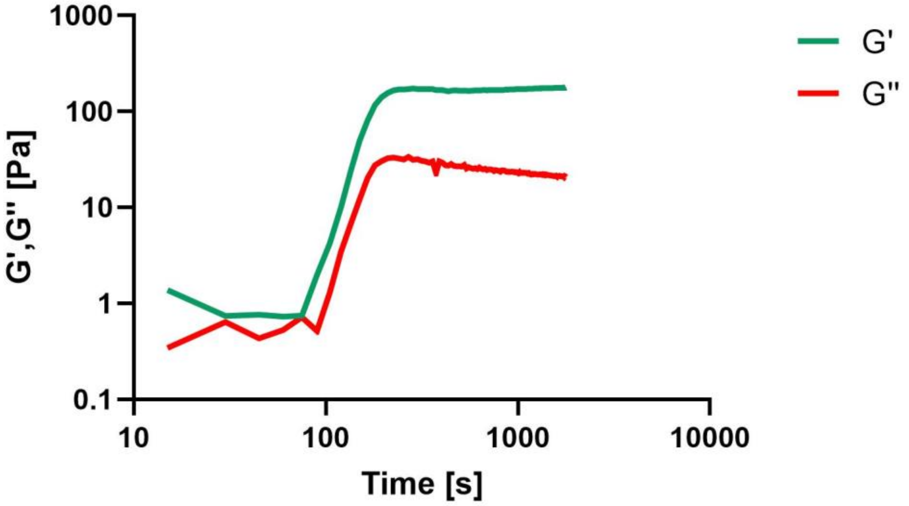

Figure 47: Time sweep test performed on G-ECM hydrogel at a constant temperature of 37°C. Duration of test was of 30 minutes. During the test, frequency (1 Hz) and strain (0.1%, within the LVE region) were kept constant.

Frequency sweep tests performed at 37°C (**Figure 48**) confirm that the material is in the gel state. Moreover, the storage modulus obtained is compatible with the values defined in the literature for the extracellular matrix of glioblastoma (100 and 10kPa). [50]

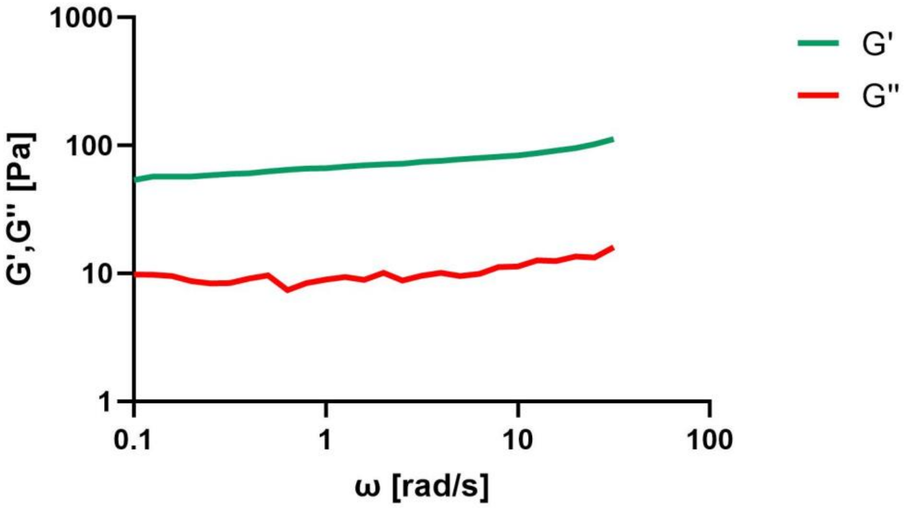

Figure 48: Frequency sweep test of G-ECM hydrogel at 37°C. The test was performed varying frequency on a range of 0.1-100 rad/s, while keeping the strain value settled to 0.1% (within the LVE region). The graph confirmed the gel nature of the hydrogel at 37°C since G' is over G''. Test was performed after solution was kept 15 minutes at 37°C.

The frequency sweep tests were performed also at other temperatures to identify where the sol-gel transition occurs. Temperatures tested were 25°C, 15°C, 10°C and 4°C. As shown in **Figure** 49, the hydrogel maintained a gel behaviour until the temperature was set to 4°C. At this temperature, a crossover point between G' and G'' was observed, indicating a gel-to-sol transition. [111]

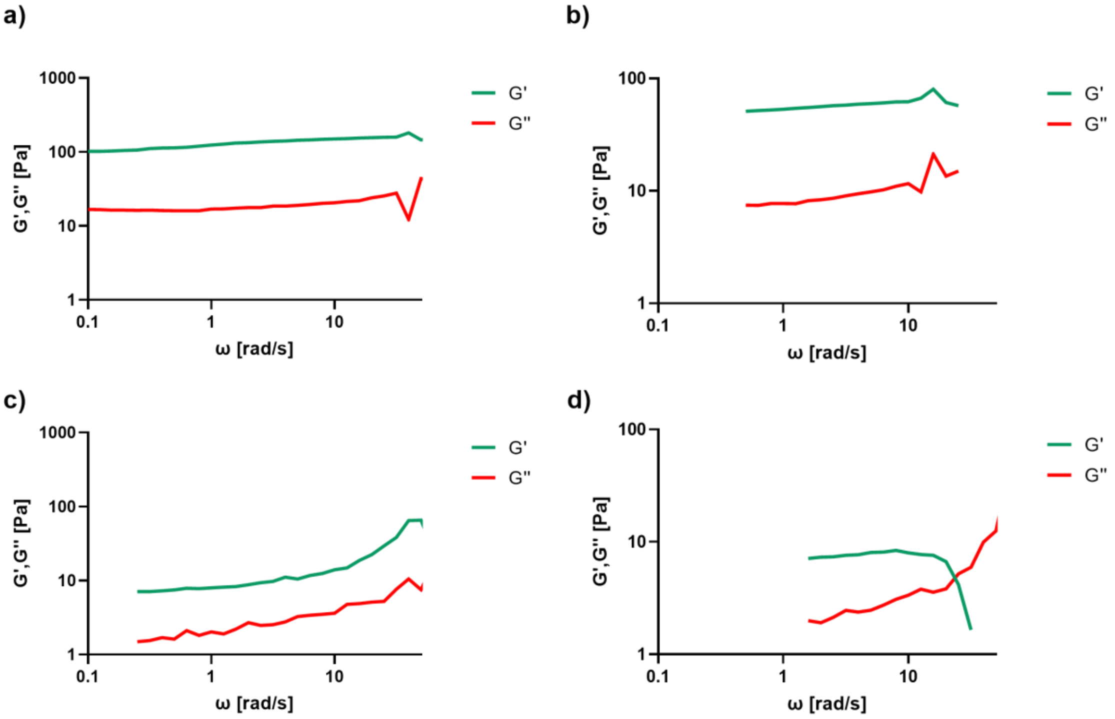

Figure 49: Frequency sweep test at different temperatures for G-ECM hydrogel. a) Frequency sweep test performed at 25°C. b) Frequency sweep test performed at 15°C. c) Frequency sweep

test performed at 10°C. d) Frequency sweep test performed at 4°C. All tests were performed after 15 minutes at the selected temperature.

Therefore, these tests allowed to affirm that for G-ECM hydrogel, stability can be guaranteed in the range 10°C -37°C. Moreover, results confirmed that temperatures below 4°C induced the transition from gel-to-sol.

Drug response of GBM spheroids embedded in G-ECM hydrogel.

Tumour spheroids were embedded in a G-ECM hydrogel matrix, to assess the role of GBM ECM in the response to drug treatment. First, monocultured U87 spheroids were embedded in the G-ECM matrix and treated with BTZ or BTZ-NPs.

As shown in **Figure 50**, untreated U87 spheroids had a strong tendency to migrate through the collagen hydrogel. This tendency was maintained also after treatment with low concentrations of BTZ-NPs (10, 50 nM). However, the highest concentration (200 nM) of BTZ-NPs led to a massive reduction in cell invasion. The same decrease was observed after treatment with free BTZ. Qualitatively, a 50 nM concentration of BTZ seemed to induce the same inhibition effect as the 200 nM BTZ-NPs. Furthermore, fluorescence imaging (obtained by labelling U87 with Vybrant™ DiD Labelling Solution) confirmed the presence of invasive cells surrounding the spheroids, and the poor efficacy of the BTZ treatment against U87 spheroids, since only a small reduction of spheroid size was observed.

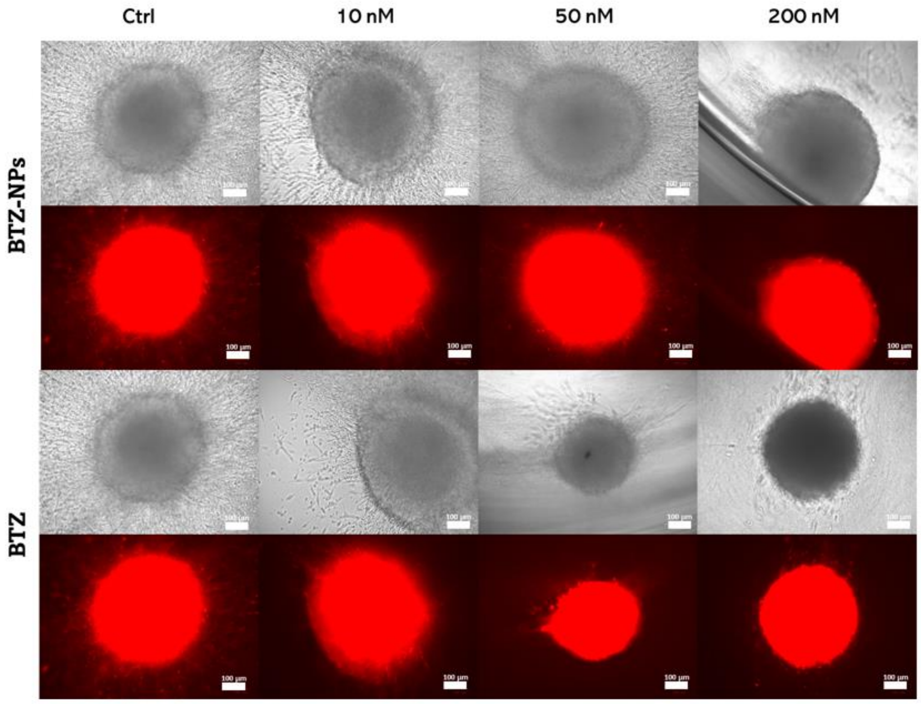

Figure 50: Bright field and red field images of U87 spheroids (labelled with Vybrant™ Dil Cell-Labelling Solution), embedded in G-ECM hydrogel and treated with different concentrations of BTZ-NPs and BTZ (10 nM, 50 nM, and 200 nM). Images were acquired at 48 h after treatment. Scale bars= 100µm.

Tumour Mix spheroids were also embedded in the G-ECM gel and treated with BTZ-NPs and BTZ.

Since HMC3 cells are usually not located inside the spheroid mass, unless for advanced state of GBM progression [112], HMC3 cells were embedded in the G-ECM gel surrounding the Tumour Mix spheroid, to evaluate HMC3 impact on the behaviour of spheroids.

Figure 51 reports the percentual fluorescence intensity [%] values (normalized by the intensity of the controls) after the treatment with three concentrations of free BTZ and BTZ-NPs in the presence or in the absence of embedded HMC3.

As shown in **Figure 51,a**, all treatments with free drug resulted in a reduction of fluorescence intensity, i.e., cell viability, lower when higher BTZ concentrations were administered. Specifically, after 96h of treatment at the concentration of 200 nM the fluorescence intensity decreased to nearly 25% of its initial value. Overall, all concentrations of free BTZ induced a reduction in cell viability. On the other hand, BTZ-NPs treatment had a similar efficacy, comparable with BTZ, only for concentration of 200 nM. This result could be related to the reduced NPs delivery to the tumour caused by the embedding inside a hydrogel matrix, which does not influence free BTZ diffusion due to its smaller size.

As shown in **Figure 51,b**, the trends were similar in presence of HMC3 cells: free BTZ had the most notable effects, and a similar response was induced by the highest concentration of BTZ-NPs. These results confirmed how the presence of HMC3 cells did not significantly affect treatment with either free drug or NPs.

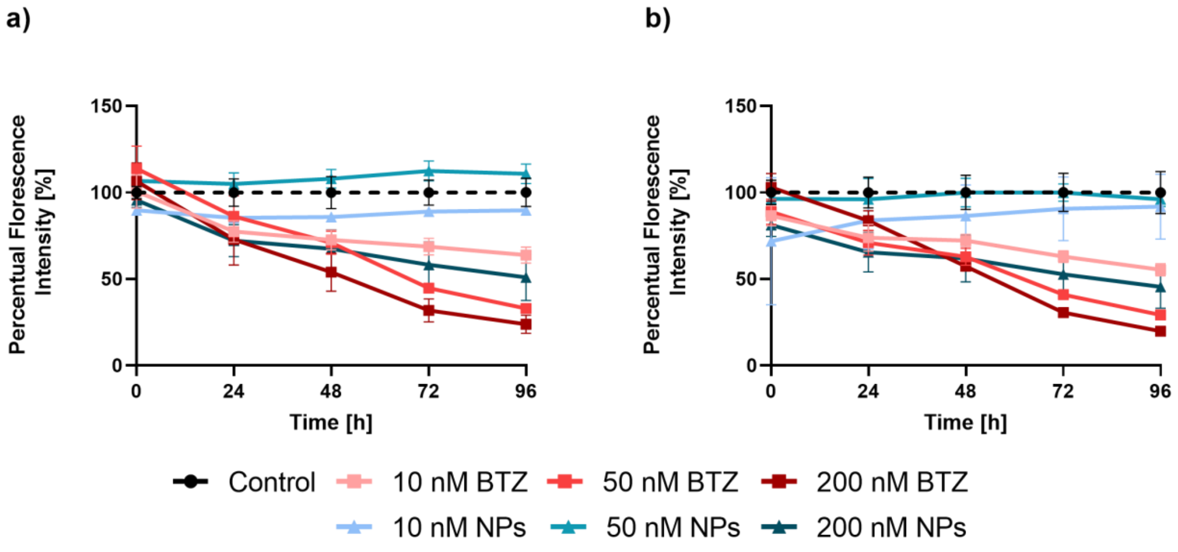

Figure 51: Fluorescence intensity of Tumour Mix spheroids embedded in G-ECM gel a) without HMC3 and b) containing HMC3, over 96h of observation after treatment with BTZ and BTZ-NPs at different concentrations (10, 50, 200 nM).

This aspect was further confirmed by the analysis of invasive patterns of Tumour Mix spheroids in the G-ECM matrix, reported in **Figure 52**.

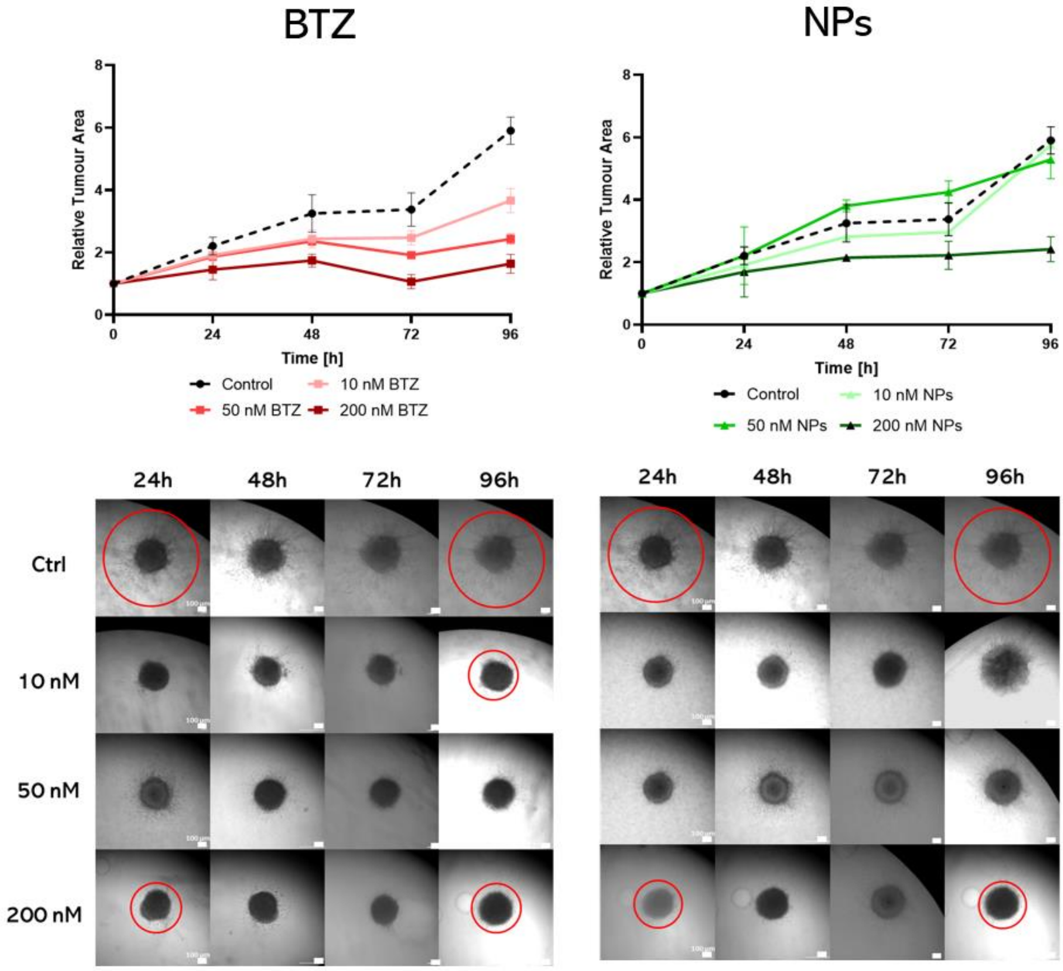

Figure 52: Quantitative (Relative Tumour Area) and qualitative analysis (brightfield images) of infiltration of Tumour Mix spheroids embedded in G-ECM gel. Results were acquired over 96h of observation after the treatment with BTZ and BTZ-NPs at different concentration (10, 50, 200 nM). Scale bars= 100 μm.

Results show how treatment with free BTZ reduced the tendency of the Tumour Mix spheroid to infiltrate, especially for concentrations above 50 nM. On the other hand, coherently with cell viability, BTZ-NPs did not produce significant variations of the spheroid invasiveness for treatments up to 50 nM. The treatment at the highest BTZ-NPs concentration (200 nM) generated an effect comparable to what observed for the free drug at 50 nM. For all treatment conditions the highest effect was observed after 72 hours, while efficacy seemed to decrease at the 96h timepoint. This is coherent with the mechanism of action of BTZ, which transiently inhibits proteasome activity, with a maximum activity observed within 72h from exposure to the drug.[113]

Figure 53 shows that the invasion trends with HMC3 cells presence in the G-ECM.

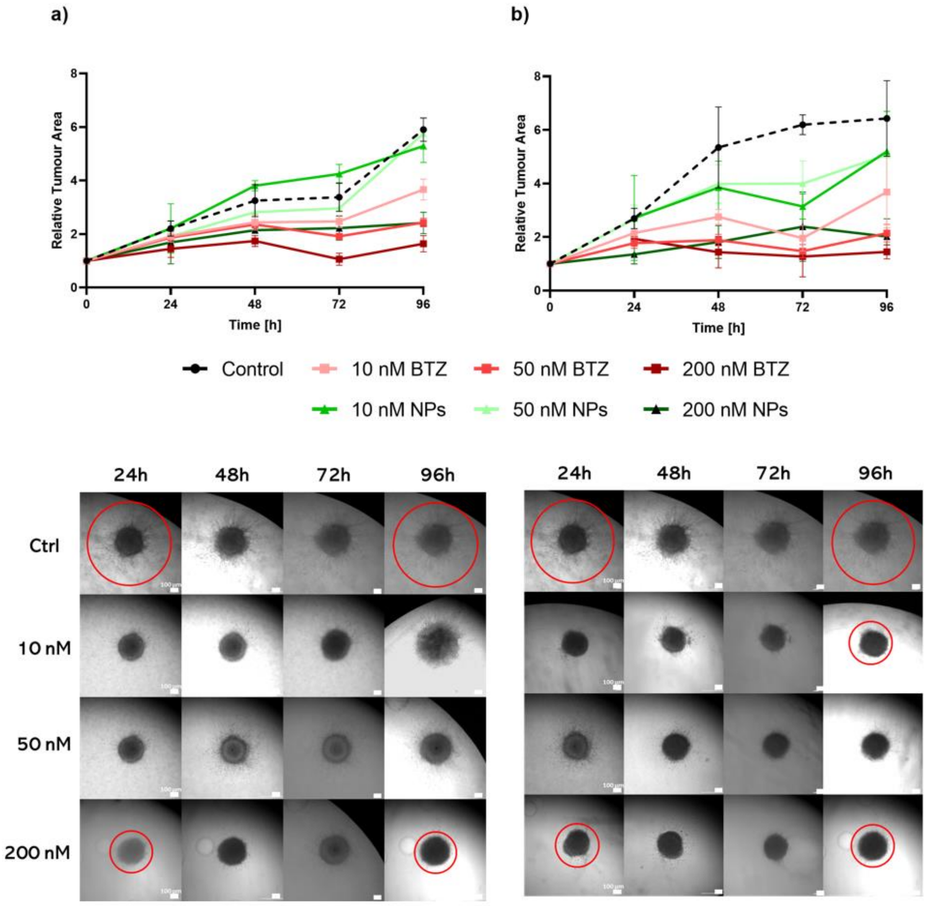

Figure 53: Quantitative (Relative Tumour Area) and qualitative analysis (brightfield images) of infiltration of Tumour Mix spheroids and HMC3 embedded in the G-ECM gel. Results were acquired over 96h of observation after the treatment with BTZ and BTZ-NPs at different concentration (10, 50, 200 nM). Scale bars= 100 μm.

Invasion trends were not different between the setups with and without HMC3 cells, suggesting again how microglia did not affect drug efficacy. However, the presence of microglia in the G-ECM matrix led to a more pronounced and faster invasion of the Tumour Mix spheroid. This evidence confirmed that microglia, communicating with surrounding cells and sensing mechanical cues from the ECM, may contribute to GBM progression and diffusion, e.g., through the expression of cytokines. [114]

Drug response of BIO-Mix spheroids embedded in G-ECM

Figure 54 shows the infiltration of BIO-MIX spheroids inside the G-ECM gel. Untreated spheroids migrated and invaded through the gel matrix. However, this migration tendency was reduced after BTZ-NPs administration. This reduction of the infiltration area was even more evident when the treatment was performed using free BTZ, with concentrations above 50 nM. Moreover, the negative effect of treatment is also confirmed by merged images of **Figure 54**, which show how the red signal is progressively dimmer, with increasing BTZ concentrations, especially with free drug. Lastly, control images proved that spheroid embedding did not alter the spatial disposition of cells within the spheroid: GBM-8 cells are mostly found in little niches around the spheroids and on the centre, while red signals, referring to the U87 cells, can be found all over the mass.

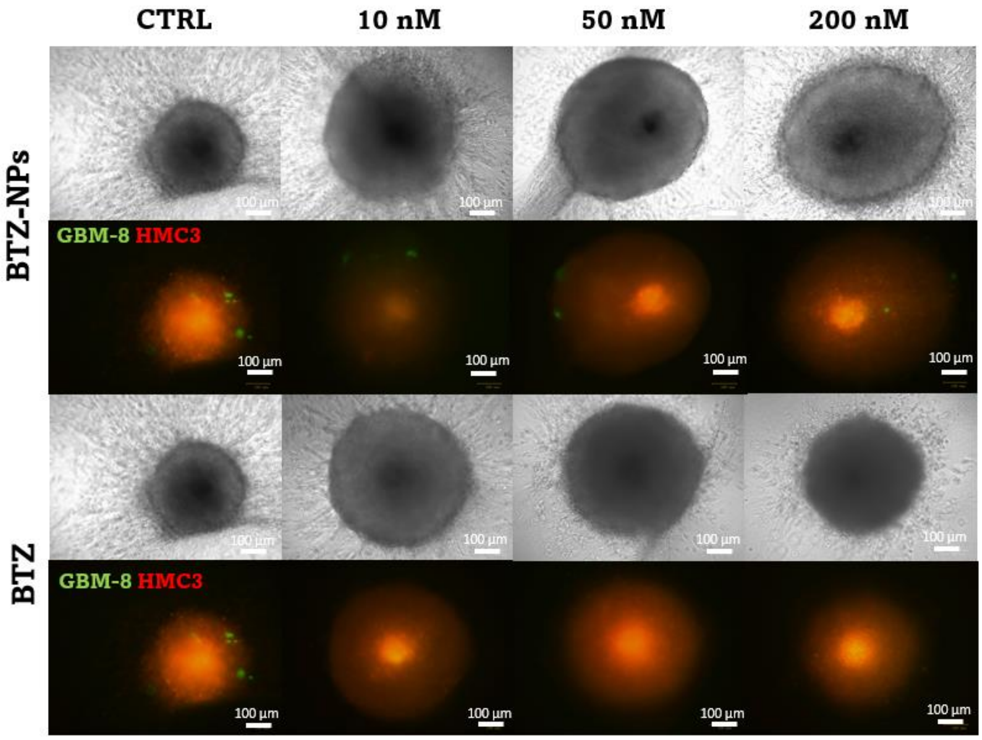

Figure 54: Bright field and red field images of BIO-MIX spheroids embedded in G-ECM hydrogel and treated with different concentrations of BTZ-NPs and BTZ (10 nM, 50 nM, and 200 nM). U87 cells (labelled with Vybrant™ DiI Labelling Solution) are shown in red, GBM-8-GFP are shown in green. Images were acquired at 24 h after treatment. Scale bars= 100µm.

Drug response of GBM TSs embedded in stiff Glycosaminoglycans (GAGs)-like hydrogel.

Considering that the matrix strongly affects the diffusion and delivery of NPs, as indicated by the above experiment and by other works [115], we also tested a stiffer glioma ECM-like matrix, the VitroGel® 3D hydrogel xeno-free solution (The Well Biosciences). This matrix is composed of polysaccharides, that replicate the role of Glycosaminoglycans (GAGs) present in the GBM ECM, which are responsible for the high elastic modulus of the tumour tissue.

By testing different concentrations of the GAG-like gel, (Figure 53)) it was observed that the two higher concentrations (1:3 and 1:5) did not affect spheroid shape overtime, since spheroids seemed to mostly maintain their original shape and remained compact. Changes in spheroid structure and shape were observed for the two lower concentrations (1:10 and 1:20), although no invasion though the matrix was observed. These results confirm that gel stiffness affects the behaviour of the tumour spheroids, with lower stiffness resulting in less compact spheroids (**Figure 55**).

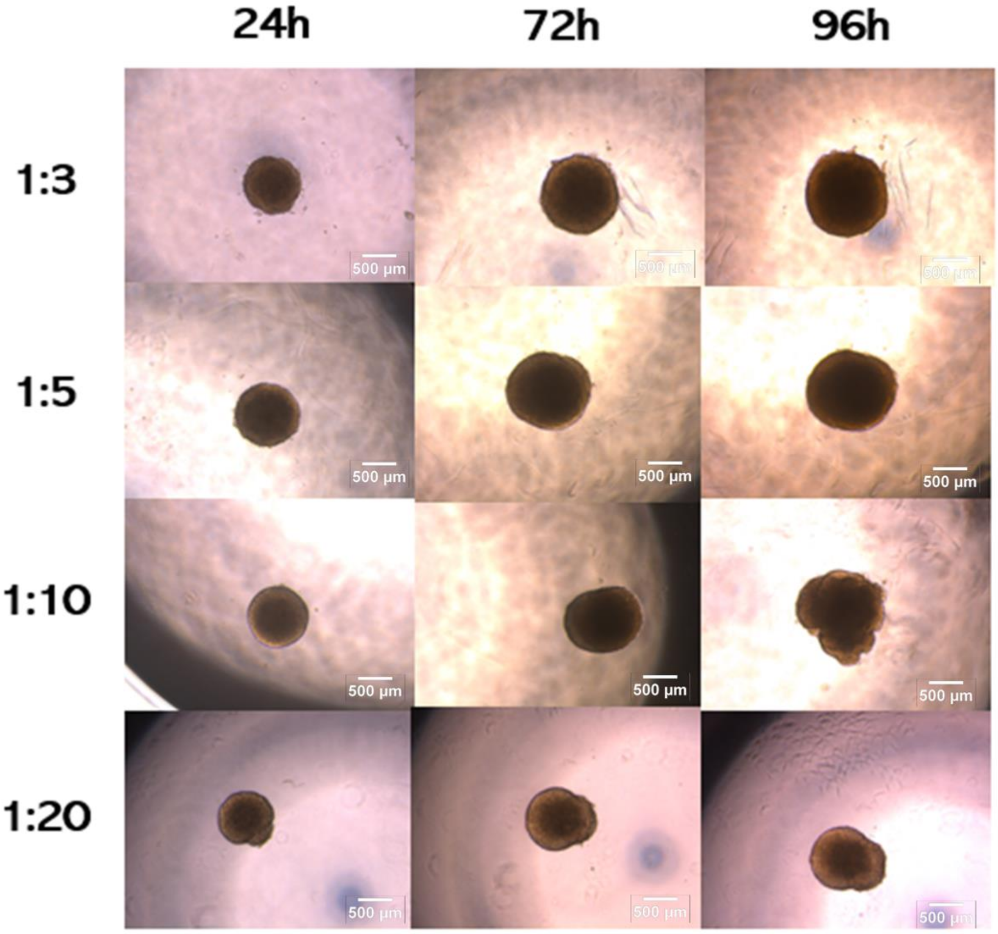

Figure 55: Optical images of Tumour Mix spheroids in GAGs-like gels at different dilutions (1:3, 1:5, 1:10, 1:20). Images were acquired at different time points (24, 48, 72 and 96h). Red circles highlight the areas of infiltration after 24, 72 and 96 h. Scale bar= 500µm.

The effect of BTA and BTZ-NPs was then tested on the Tumour Mix spheroids embedded in the GAG-ECM. Images were acquired after 48-, 72- and 96-hours post treatment.

Results in **Figure 56** indicate that the effect of treatment was lower than in G-ECM gel. For free BTZ, the 200 nM concentration resulted in the highest decrease in cell viability as observed in the G-ECM. While treatment with BTZ-NPs did not reduce cell viability. This indicated how a stiffer matrix, hampered drug delivery to the tumour mass, since we observed that only the highest concentration of the FD (of smaller size than BTZ-NPs) induced some cytotoxic effect. This proved once more how the integration of spheroids in the correct ECM-like matrix is fundamental to predict a reliable drug delivery efficiency to the tumour mass. Therefore, determining the correct mechanical properties and composition of the tumour ECM is fundamental to design a correct ECM replica for in vitro studies.

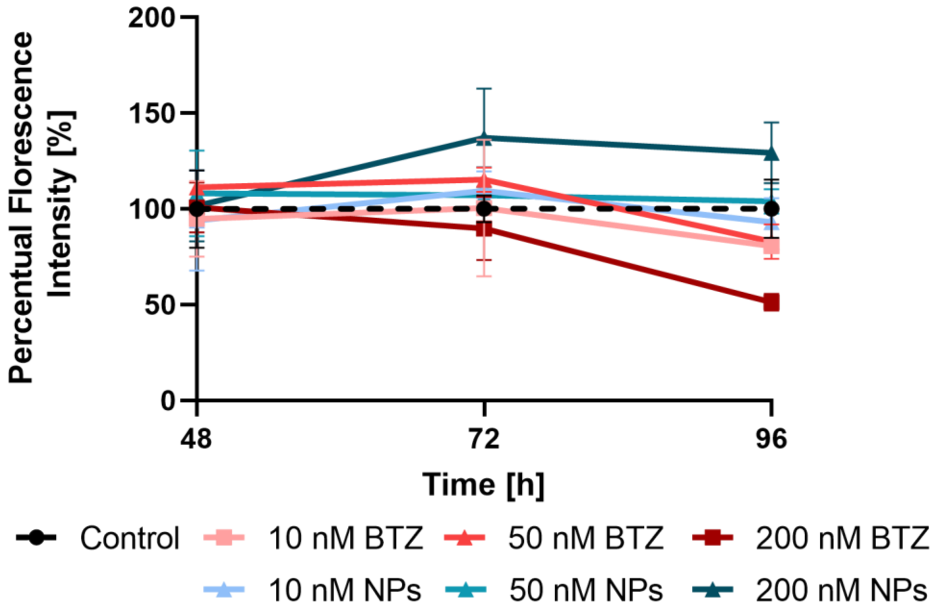

Figure 56: Fluorescence intensity of Tumour Mix spheroids embedded in GAGs-like gel, over 96h of observation after the treatment with BTZ and BTZ-NPs at different concentration (10, 50, 200 nM).

Microscopy images of the Tumour Mix spheroids embedded in the GAG-like gel further confirm this behaviour **Figure 57**. No evident reduction in the fluoresce intensity of the spheroid was observed overtime when treating with BTZ-NPs. However, when using free BTZ at the highest concentration, a slight reduction in fluorescence signal was noted after 72 h, which became more evident at the longest timepoint.

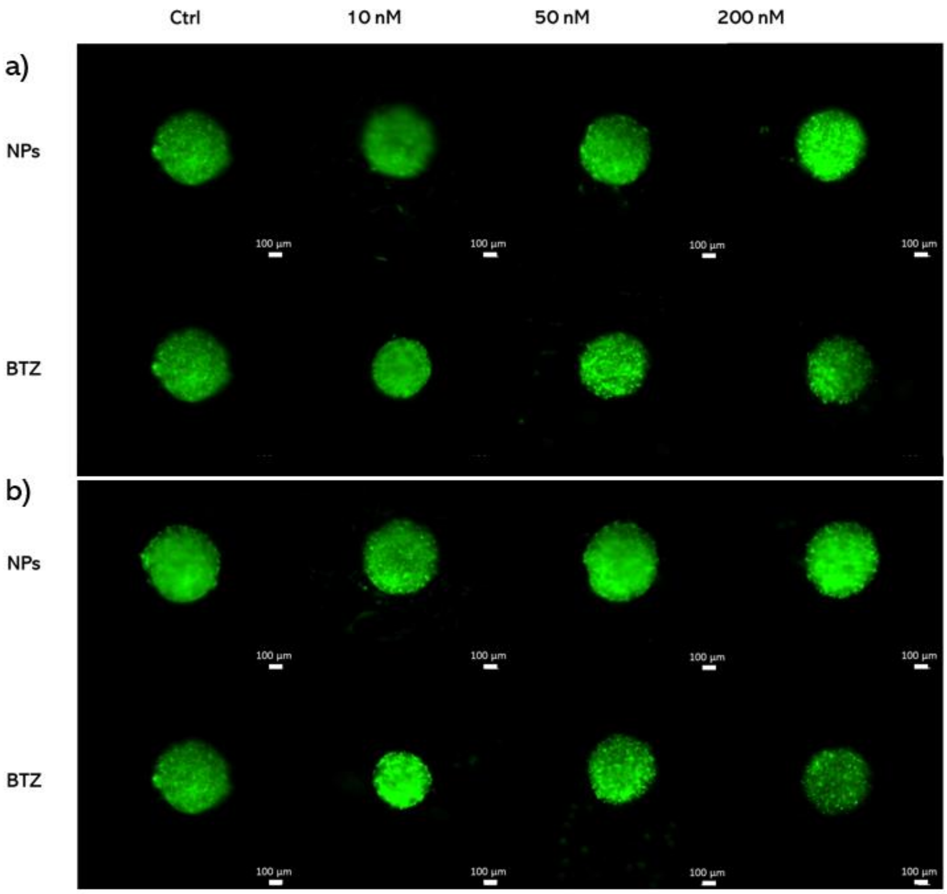

Figure 57*:* Fluorescence imaging of Tumour Mix spheroids embedded in GAGs-like gel and treated with different concentrations of BTZ and BTZ-NPs (100 nM, 200 nM, and 500 nM). Images were acquired after a)72h and b) 96h of treatment. GFP-labelled U-87 and GBM-8 are shown in green. Scale bar= 100 µm.

It is important to point out that, when using GAGs-like gel, infiltration patterns were not investigated, since visual inspection of the wells confirmed the total absence of cell migration. This was thought to be due to a higher stiffness characterizing the GAGs-like gel, as also confirmed by other works. [116]

Assessment of microglia tumour homing capability

To further understand the role of HMC3 in the TME and how their behaviour, in particular migration, is influenced by the presence of the tumour mass the horizontal and vertical migration pattern of microglia through the G-ECM gel was investigated in the presence or absence of the tumour spheroid. Without the tumour spheroid, HMC3 cells remained confined in the gel where they were initially embedded, and no migration was detected in either direction after 48 hours (**Figure** 58**),** regardless of the initial concentration of cells in the gel.

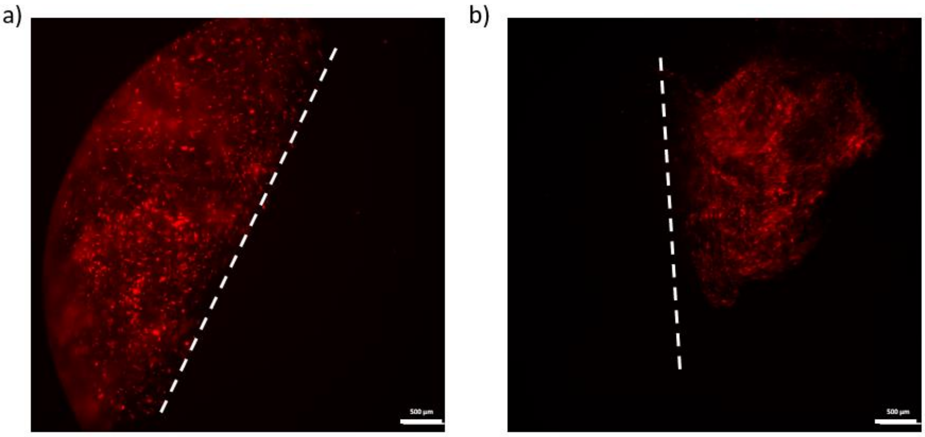

Figure 58: Fluorescence imaging of HMC3 cells 48h after the embedding in the -ECM gel, with a seeding density of a) 25000 or b) 50000 cells/well. HMC3 cells (labelled with Vybrant™ Dil Cell-Labelling Solution) are shown in red. The interface between the two G-ECM matrix is outlined by a dotted line. Scale bars= 500µm.

On the other hand, when Tumour Mix spheroids were embedded in the G-ECM gel, migration of HMC3 towards the spheroid could be noticed both for the horizontal and the vertical, setup, more evident for higher concentrations of HMC-3 in the gel Fluorescence acquisitions in z-stack modality demonstrated that the microglia were able to infiltrate the spheroid and localized in the core for IG setup (**Figure 59**).

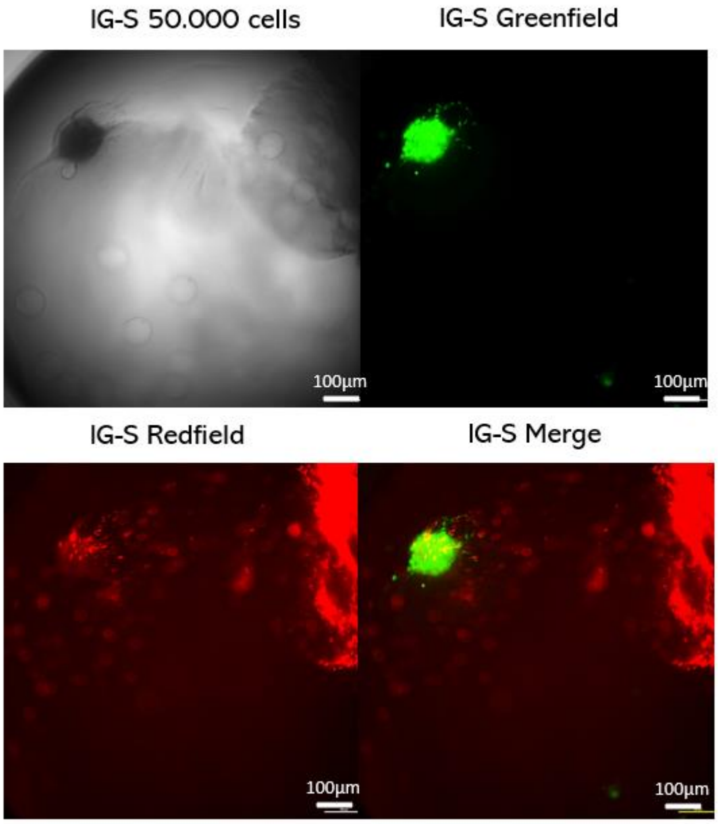
IG-S 50.000 cells

IG-S Greenfield

IG-S Redfield

IG-S Merge

Figure 59: Fluorescence imaging of HMC3 cells 48h after the embedding in IG-S. HMC3 cells (labelled with Vybrant™ Dil Cell-Labelling Solution) are shown in red, while GFP-labelled U-87 and GBM-8 are shown in green. Scale bars= 500µm.

This behaviour was confirmed also for the vertical setup (**Figure 60**), Indeed, the signal of HMC3 was distributed inside the spheroid and microglia were found in the core. While, for Bottom-Gels with no spheroid any migration trend was noted.

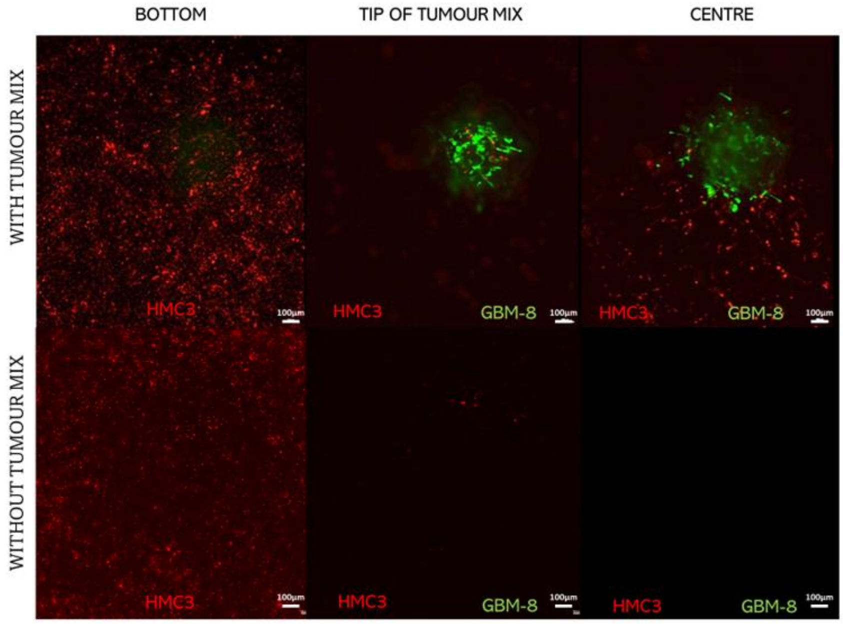

Figure 60: *Z* Fluorescence imaging of HMC3 migration at different heights in BG with and without Tumour mix Spheroids, after 48h. HMC3 cells (labelled with Vybrant Dil Cell-Labelling Solution) are shown in red, GFP-labelled U87 and GBM-8 cells are shown in green. Scale bars= 100µm.

5.4 An in vitro 3D-model of the BBB

It has already been mentioned that the Blood Brain Barrier plays a crucial role in supporting growth and progression of the GBM, as well as in regulating drug transport to the CNS. In tumour conditions, the permeability of the BBB might be modified, however this is still an open debate. [40], [117] Therefore, reliable models of GBM must strive to produce and include this fundamental player.

In this optic, we created BBB spheroids, BBB-S, and BBB on a chip to be merged with the spheroid and G-ECM models.

As it is shown in **Figure 61**, BBB spheroids including endothelial cells, pericytes and astrocytes were successfully obtained. Endothelial cells appeared distributed over the spheroid mass, while pericytes and astrocytes show this tendency seemed to preferentially accumulate towards the centre of the spheroid (violet and red signals in **Figure 61**). These images can be confronted with the ones obtained by the coculture of pericytes and endothelial cells. Surprisingly, the absence of astrocytes did not alter the positioning of pericytes (shown in red) within the BBB spheroid, since they can still be found in the centre of the spheroid.

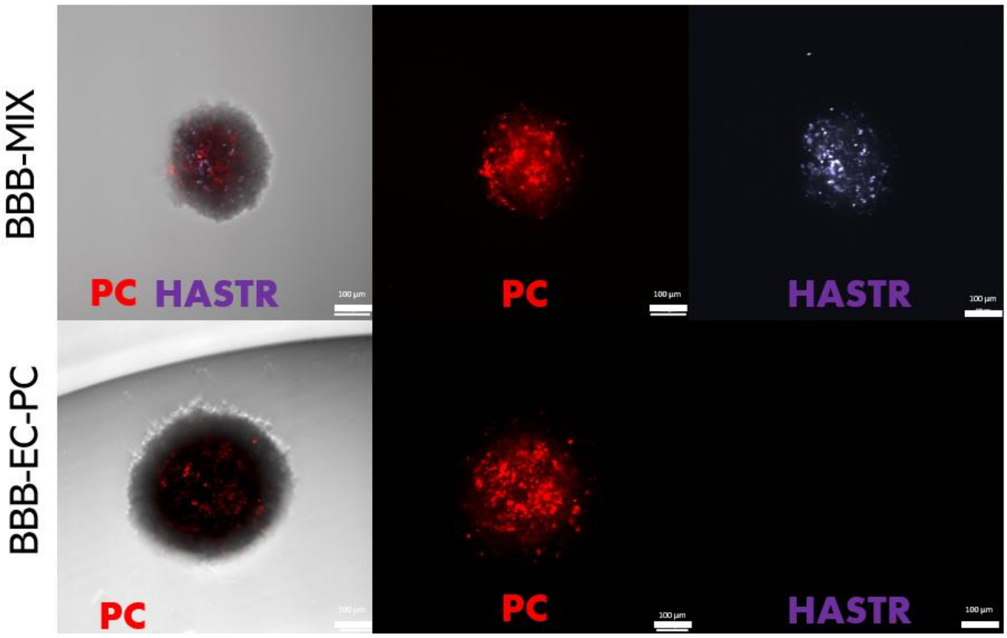

Figure 61: a) Image acquired in fluorescence microscopy for BBB MIX and BBB-EC-PC spheroids. Pericytes are shown in red (labelled with Vybrant™ Dil Labelling Solution), while astrocytes are shown in violet (labelled with Vybrant™ DiD Labelling Solution). Scale bars= 100 µm.

An immunostaining for ZO-1 protein (associated with tight junctions) confirmed the presence of ZO-1 proteins in the whole structure of the spheroid, in areas where endothelial cells were identified (**Figure 62**). This evidence highlights the potential of spheroid-based models, as they can replicate the interaction between BBB cells as well as the presence of thigh junctions, which are one of the key elements in the barrier effect of brain capillaries.

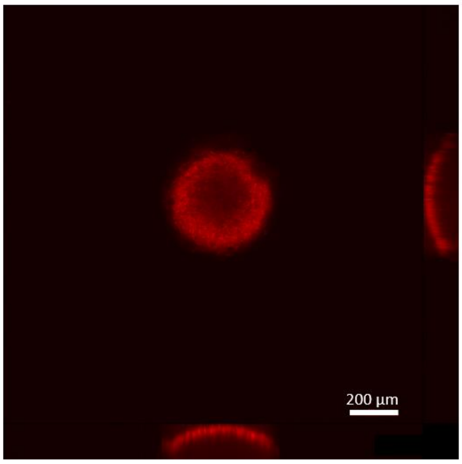

Figure 62*:* Reconstruction of lateral and frontal projections obtained using Z-stacking feature of the BBB-EC-PC for the immunostaining of ZO-1, with Anti-ZO1 antibody. The distribution of ZO-1 is shown in red. Scale bar= 200 µm.

5.5 3D-Vascular commercial model

Preliminary testing

Human brain endothelial cells HBEC-5i and human pericytes (HVBPCs) in contact with the G-ECM gel used in the microfluidic device was verified before proceeding with further tests.

Therefore, cell adhesion was verified by acquiring images of the different cell lines over the G-ECM gel., at 24h and 48h. As shown in **Figure 63,** both cells adhered to the G-ECM gel without any difficulty after 48h. HBEC-5i cells adhered well after 24h of culturing, while HVBPC took more time to fully adhere. This behaviour was also confirmed by the cell viability assays (**Figure 64).**

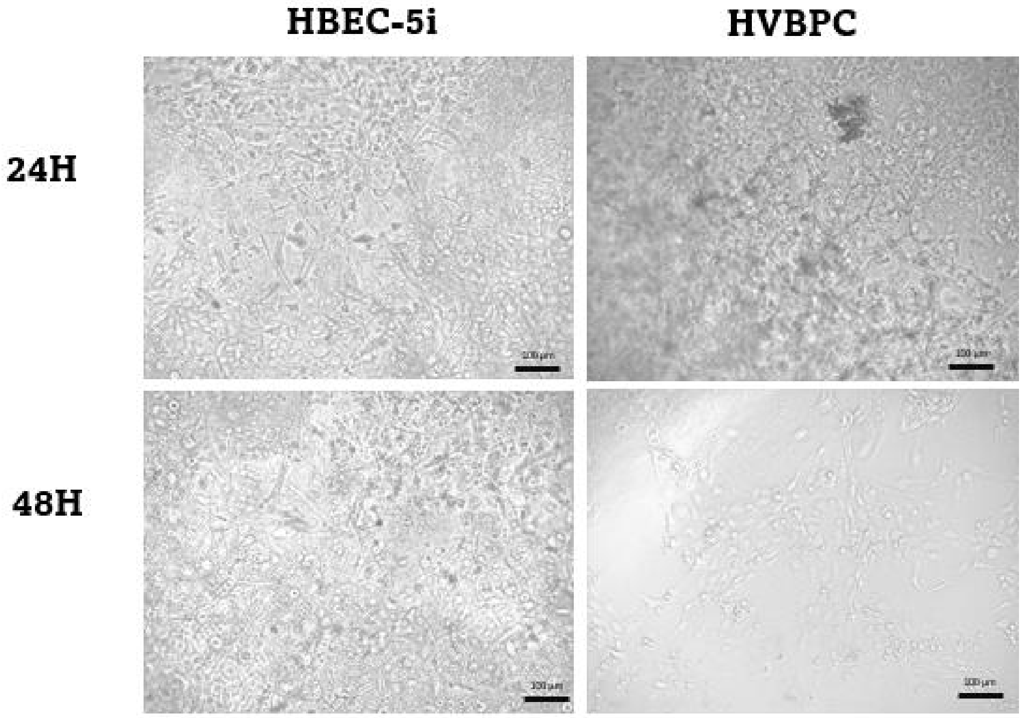

Figure 63: Brightfield images of HBEC-5i and HVBPC, cultured on G-ECM after 24h and 48h. Scale bars= 100 µm.

Figure 64 shows that endothelial cells (HBEC-5i) were able to grow and proliferate in the G-ECM gel, as indicated by the increase in cell viability overtime. Therefore, our preliminary results indicate that the HBEC-5i cell line is suitable for the microfluidic chip approaches. Pericytes and the combination of the two cell lines showed a similar trend, with non-cytotoxic effects noted.

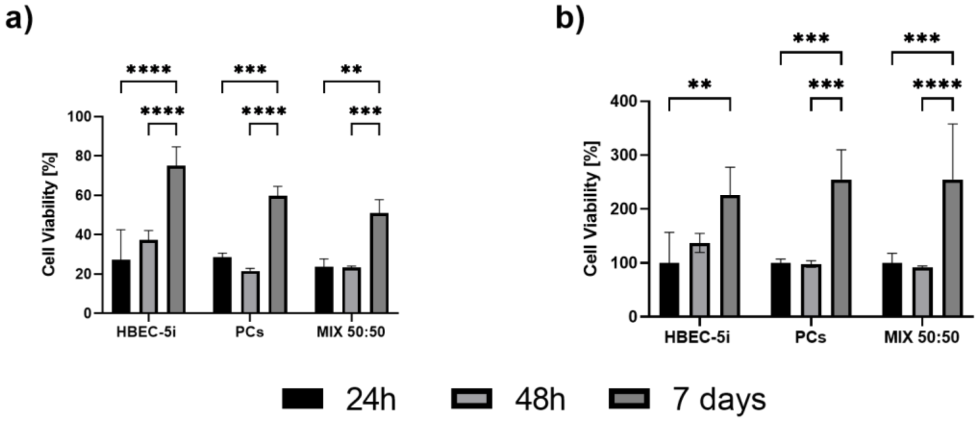

Figure 64: Cell viability of HBEC-5i, HBVPCs and their combination (MIX 50:50) seeded in G-ECM gel. a) Percentual cell viability normalized by the mean values obtained for the corresponding 2D culture control b) Cell viability normalized by the values at 24h. Multiple comparisons were performed using two-way ANOVA. *p<0.05, **p<0.01, ***p<0.001, ****p<0.0001.

Development of a microvascular network

Following the protocol in **4.2.4**, we obtained an *in vitro* brain capillary network with dense homogenous vessel structure and well-branched sprouts.

In the absence of a well-dense structure of the G-ECM gel, endothelial cells were able to migrate in the graft chamber, without encountering barriers. On the other hand, as shown in **Figure 65,** a correctly performed G-ECM gel seeding and gelation allowed the creation of perfusion channels. Otherwise, cells were free to migrate into the graft chamber.

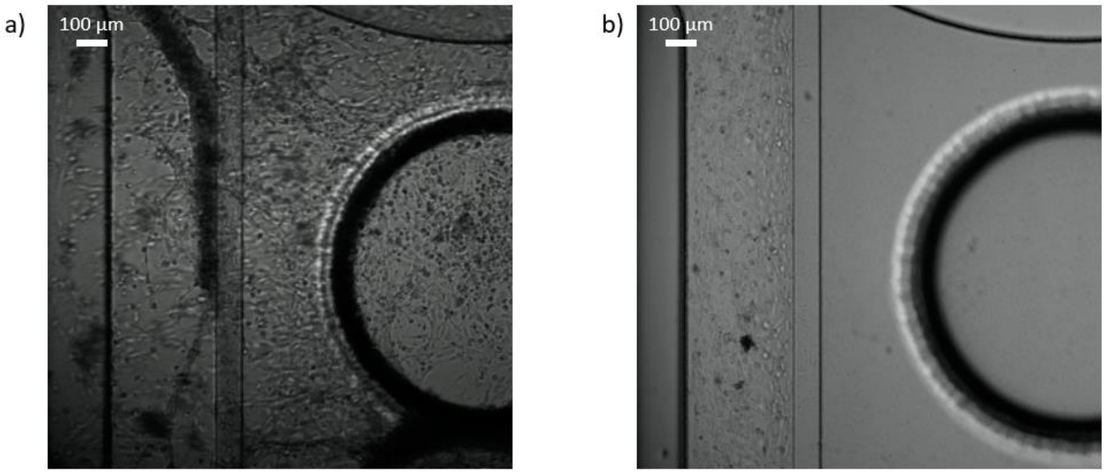

Figure 65: Brightfield images of the perfusion channels and graft chamber. a) Cells spreading in the absence of a well-gelled G-ECM barriers, b) Correct distribution of endothelial cells through the perfusion channels, after a correct G-ECM deposition. Scale bar= 100µm.

Since it was proven that the presence of the G-ECM gel walls did not support the homogeneous adhesion of endothelial cells (**Figure 66,a)** and the addition of the growth factors-enriched medium caused the detachment of the formed endothelium (**Figure 66,b),** we performed some optimization steps for the seeding protocol.

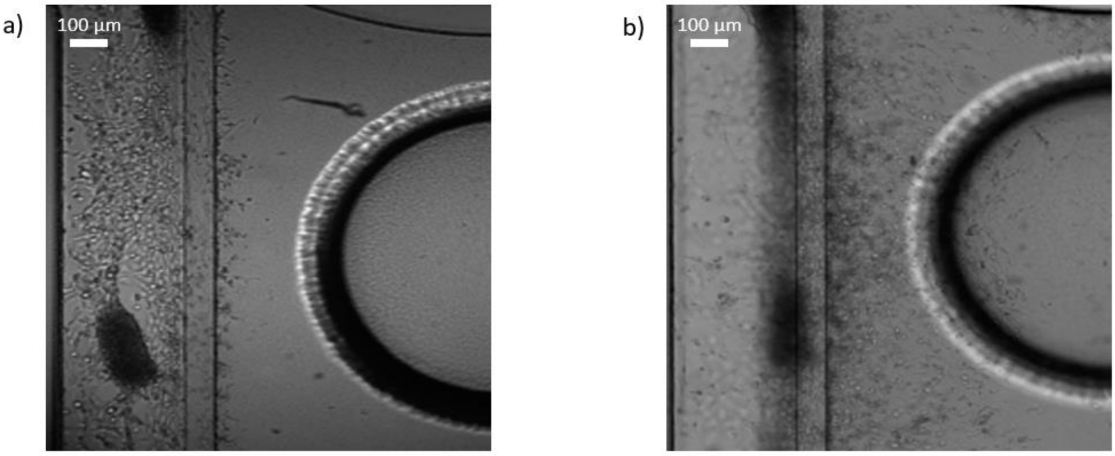

Figure 66: Brightfield images of perfusion channels and graft chamber after the direct seeding of HBEC-5i. a) Formation of cell aggregates and areas without cell adhesion after 4 days from seeding. b) Detachment of endothelium and invasion into the graft chamber after the addition of pro-angiogenic factors (day 7). Scale bar= 100µm.

Thus, we suspended HBEC-5i in a mixture of their culture medium and 0.1% gelatine (ATCC), to increase adhesion. All steps were performed at low temperature to avoid gelatin cross-linking before seeding. After seeding, gel stabilization was achieved at 37°C.

This approach led to the formation of a homogeneous endothelial cell coating within the canal. The endothelium appeared complete about 4 days after cell seeding, as shown by images in Figure 67 acquired after 3 and 5 days from cell seeding. In both cases, the vessel appeared to be intact, and only a few cells migrated spontaneously and randomly to the graft chamber.

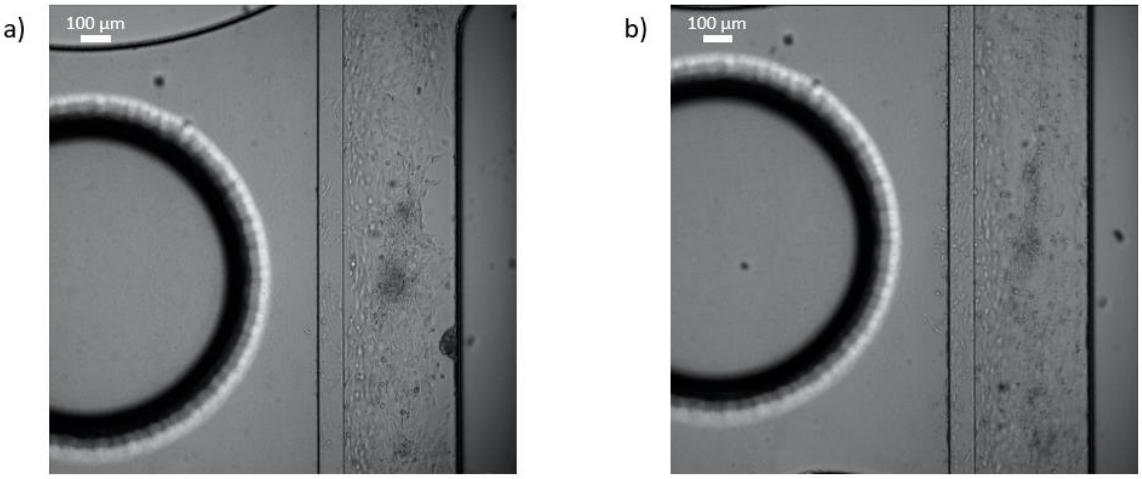

Figure 67: a) Brightfield image proving the correct realization of a vessel inside the perfusion channel, 3 days after HBEC-5i seeding, b) Brightfield image showing the beginning of sprouting towards the graft chamber, after 5 days from seeding. Scale bar= 100 µm.

Once the formation of the channel was verified, it was fundamental to assess the preserved structure and functionality characterizing the cerebral capillaries. As shown in Figure 68,a endothelial cells preserved their morphology and were densely and homogeneously spread over the channel. An immunostaining allowed to verify the presence of a functional vascular capillaries structure. Indeed, the immunostaining of cluster of differentiation 31 (CD31), a characteristic adhesion protein for platelets and endothelial cells [118] was performed to ensure the maintained native phenotype **(Figure 68, b)**. Immunostaining for tight junction protein-1 (or zonula occludens-1 protein, ZO-1) [119] confirmed the presence of tight junctions and the subsequent formation of a compact vascular structure that should be able to mimic the highly selective permeability of BBB capillaries and hamper the extravasation of drugs and substances from the vessel. **(Figure 68, c)**.

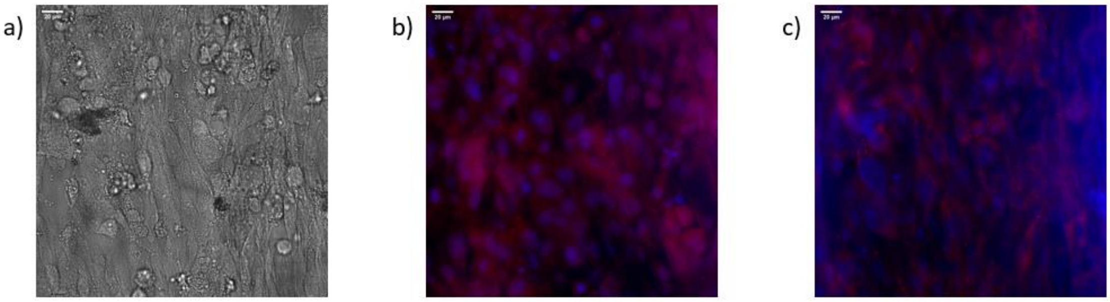

Figure 68: Images (60x magnification) of the endothelial cell seeded into a perfusion channel. a) Brightfield image of endothelial cells morphology and distribution; b) Confocal microscopy image showing endothelial cells labelled with Anti-CD31 antibody (in red) and nuclei stained with DAPI (in blue); c) Confocal microscopy image showing the presence of the tight junctions of endothelial cells stained with Anti-ZO1 antibody (in red) and nuclei labelled with DAPI (in blue). Scale bar= 20 µm.

Angiogenic sprouting.

Angiogenic sprouting was successfully induced. After complete maturation of perfusion channels, which lasted four days, the protocol by the manufacturer suggested to add a growth factor-enriched medium on the fifth day from cell seeding to induce the formation of the microvascular network. Therefore, after the administration of the pro-angiogenic cocktail, sprouts were followed for 5 days. Images were acquired both before the administration and after, on day 1 and 5. Images in **Figure 69** demonstrated how the addition of the pro-angiogenic cocktail induced sprouting phenomena, from day 1 to day 5. Moreover, this confirmed how the addition of gelatine did not hinder the formation of vessels nor the growth of new vessels towards the graft chamber.

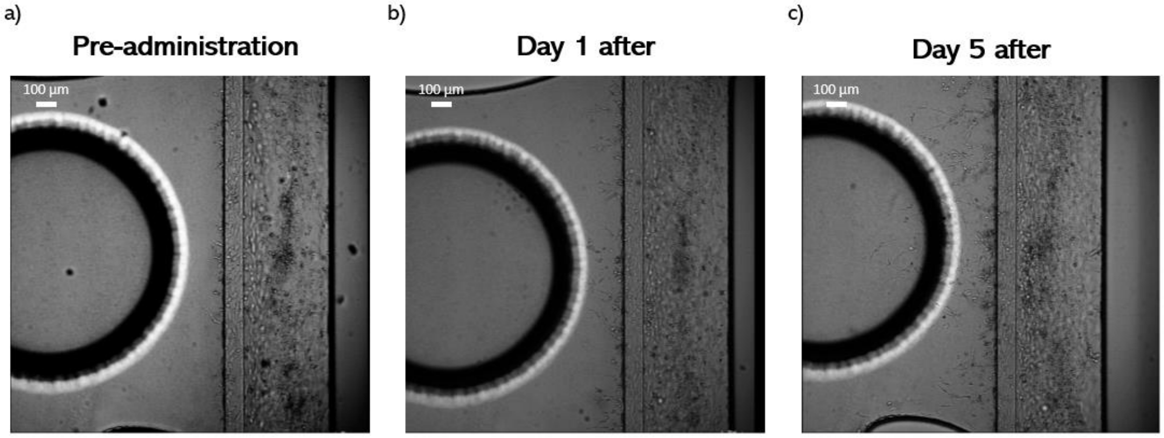

Figure 69: Brightfield images showing a partial visual of perfusion channel and graft channel; a) showing the situation prior to the growth factor administration; b) showing the first day after administration; c) showing the fifth day after administration of growth factors. Scale bars= 100μm.

Immunostaining was performed on the sprouts and confirmed the realization of a correct structure of the endothelium, as shown by the expression CD31 and ZO-1 proteins in the newly formed vessels. CD31-antibody confirmed that, even after 7 days after the administration of pro-angiogenic cocktail, cells maintained the correct phenotype (**Figure *70*, a**). The second staining in **Figure 70, b** allowed to localize occluding junctions along the capillaries, which were thought to be indicative of the replicative nature of the human brain endothelium [119].

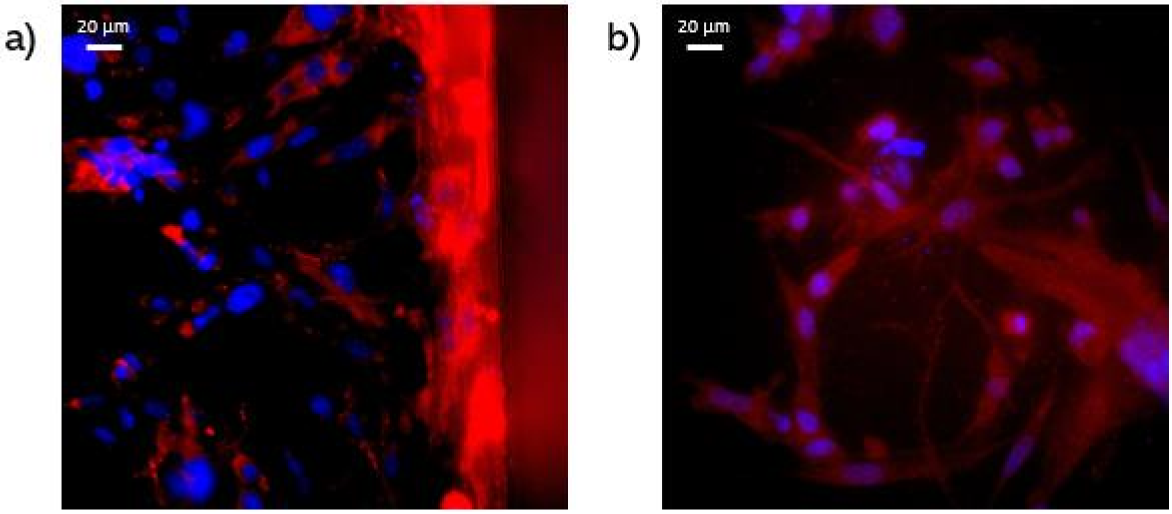

Figure 70: Immunostaining images acquired by confocal microscope (60X magnification) showing the vascular network after 7 days from administration of pro-angiogenic cocktail. a) Confocal image showing endothelial cells labelled with Anti-CD31 antibody in red and nuclei labelled with DAPI in blue. b) Confocal image showing the tight junctions present both in the origin vessel that in the sprouts (in red), obtained by the staining with Anti-ZO1 antibody, and the nuclei, stained with DAPI showed in blue. Scale bar= 20 μm.

Nanoparticles permeability assay

At this point, it was possible to draw considerations on the functionality of the endothelium created by performing a nanoparticle permeability assay. To do so, a Rhodamine-labelled NPs suspension was injected into the vascular network model, through the inlets of the perfusion channels, aiming to simulate an *in vivo* administration.

The perfusion assays on the model (**Figure 71**) illustrated that Rhodamine-NPs remained confined within the channel without permeating through capillaries (consistent with other *in vivo* studies [120]). This led to the conclusion that the walls of the perfusion channels were intact through all the assay and the microvascular network was composed of vessels with compact structure and no fenestrations allowing the permeation of cells.

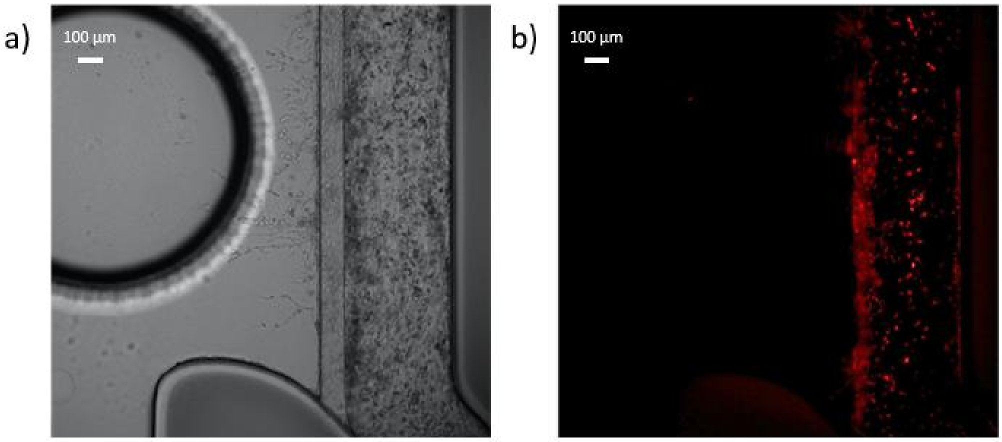

Figure 71: a) Brightfield images of a of the perfusion channel and the graft chamber, showing origin vessel and its sprouting, b) Red-field image showing the Rhodamine-labelled NPs inside the perfusion channel, 3h after injection Scale bar= 100 µm.

These results confirmed that the obtained vessels represent a good replica of the BBB permeability.

Housing of the tumour model

Once vessel formation was optimized, the tumour spheroid was inserted in the graft chamber. This was done using the Tumour Mix spheroid, by following the protocol furnished by the manufacturer. Thus, the spheroid was directly pipetted into the graft chamber, by using a pipette with a wide bore tip. This first trial however was not successful, as the spheroids seemed to lose the integrity after few hours (**Figure 72**).

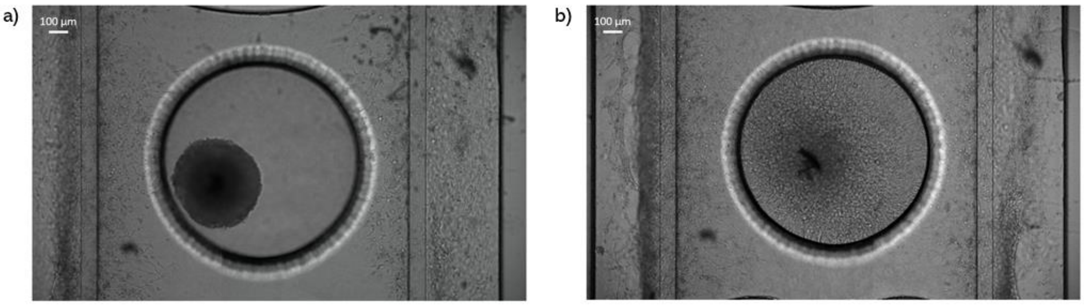

Figure 72*:* Brightfield images of the housing of the Tumour Mix spheroids; a) right after the insertion and b) after 1 hour.

Therefore, it was decided to house the spheroid but embedded in the above-mentioned G-ECM gel. This option provided a better stability for the spheroid mass, allowing the maintenance of the rounded structure several days after the insertion, that was confirmed by the fluorescence imaging of U87 and GBM-8 GFP cells in the spheroid. Furthermore, we observed invasion of tumour cells, beginning from 72h post spheroid insertion (**Figure** *73*).

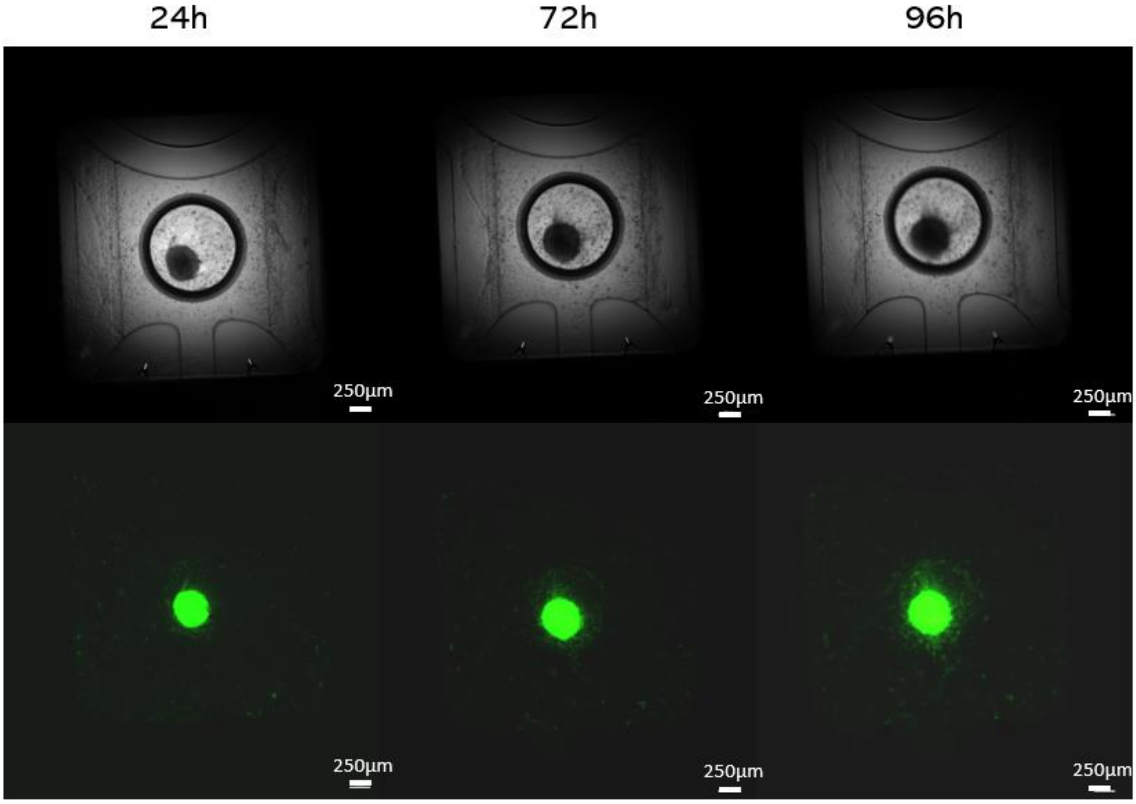

Figure 73: Brightfield and greenfield images of Tumour Mix spheroids after the insertion in the graft chamber. Images were acquired 24, 48h and 72h after the insertion of spheroids. GFP-labelled u87 and GBM-8 cells are shown in green. Scale bars= 250µm.

HMC3 extravasation through the vessel structure

At this point, we repeated in the microfluidic model a microglia migration assay in the presence or in the absence of the spheroid in the graft chamber. Thus, DIl-labelled HMC3 were injected into the perfusion channels to simulate an *in vivo* administration.

In the absence of the spheroid mass, we observed that HMC3 remained in the vessels (**Figure 74)**. Red-field images, showing HMC3, were acquired after 3h from the injection of cell suspension (**Figure** *74*, b) and indicate no extravasation of microglia through the G-ECM gel. Any migration was noted also after 24h (**Figure 74, c)**.

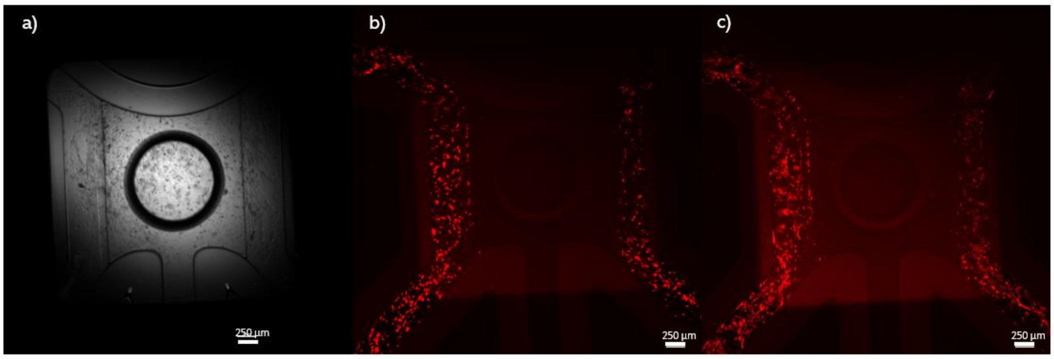

Figure 74: Bright-field (a) and red-field (b) image of the graft chamber after 3 hours from the injection of HMC3, and c) after 24h from the injection of HMC3. HCM3 (labelled with Vybrant™ Dil Labelling Solution) are shown in red. C) Scale bar=250µm.

Using a different chip containing the tumour spheroid in the graft chamber, we observed that cells started to accumulate at the walls of vessels adjacent to the Graft Chamber (**Figure 75, a,b)** and migrated towards tumour mass. Redfield images show that in presence of the Tumour Mix spheroid HMC3 were attracted towards the tumour mass and migrated through the G-ECM gel matrix (**Figure 75, c**). These results confirm that the model could be used to study, test, and validate new drug delivery methods, specifically microglia-mediated transport to GBM.

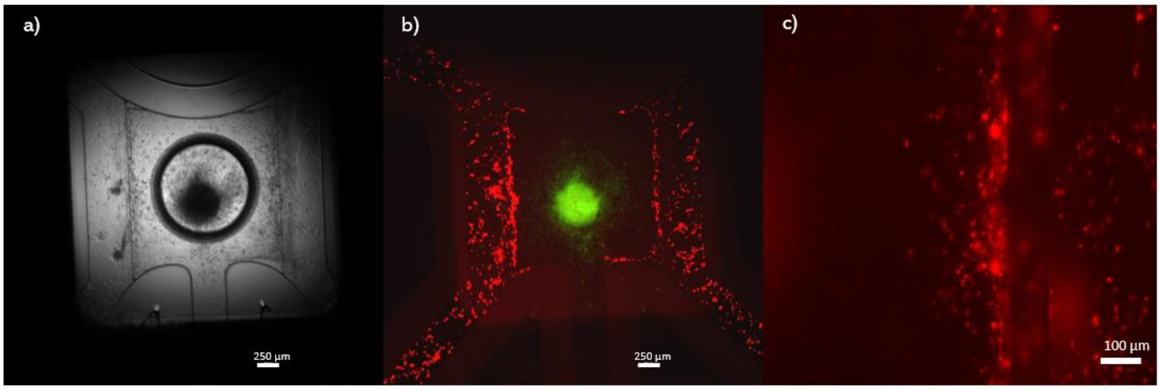

Figure 75: a) Brightfield and b) fluorescence images of graft chamber housing the Tumour Mix spheroid, 3h post injections of HMC3 cells. HMC3 cells (labelled with Vybrant™ Dil Labelling Solution) are shown in red, while GFP-labelled U87 GBM-8 are shown in green. Scale bar= 250 µm; c) Detail of the right side of the chip with the perfusion channel on the right side. HMC3 cells (labelled with Vybrant™ Dil Labelling Solution) are shown in red. Scale bar= 100 µm.

6 Conclusions

In this work, reliable models of GBM and its microenvironment (GBM TME) were obtained. Lipid-coated polymeric NPs of small size and low PDI were produced by nanoprecipitation to encapsulate Bortezomib, a proteosome inhibitor and their efficacy was validated on the novel GBM TME models. The NPs were able to encapsulate BTZ and to release it in a sustained fashion, after an initial burst. Such release profile is compatible with treatment since it is expected to reduce adverse effects of the drug.

Complex multicellular TS were successfully developed, comprising different cell lines, human GBM, GSC, immune cells and astrocytes, aiming to replicate the heterogeneous landscape of GBM. Including these cells is particularly important, since it has the potential to mimic the intercellular interactions between the different elements of the tumour TME, which are involved in determining the drug response and the development of resistance in GBM.

The preliminary drug screening on spheroid-based model proved the efficacy of the NPs-mediated treatment. Even though NPs treatment was less effective than the administration of free drug on cancer cell, NPs can reduce the cytotoxic side effect on normal cell types. Moreover, increasing the biomimicry of spheroids in terms of cellular compositions changed the response to treatment, proving the importance of mimicking the complex intercellular interaction in GBM to provide a reliable screening.

Since the tumour extracellular matrix is a relevant barrier to drug accumulation, TS were successfully embedded in a G-ECM gel to study the ability of TS to invade the matrix after the drug insult. The results confirm the role of ECM in reducing treatment efficacy, especially by limiting NPs infiltration. Moreover, the G-ECM based model was employed to prove the microglia tropism toward the tumour mass, paving the way for future nanomedicine therapies to exploit microglia as cell-carrier of NPs to enhance their infiltration. In future studies, the G-ECM can also be employed as a bioink to realize 3D-bioprinited models, which will be able to replicate not only the composition of the ECM but also its physical structure.

Since the BBB is the most relevant barrier to drug delivery to GBM, two different 3D model were designed. First, multicellular spheroids were developed using the main cellular component of the BBB (astrocytes, pericytes and endothelial cells), preserving the characteristic tight junctions found *in vivo*. Then an *in vitro* brain microvasculature network was implemented and optimized using commercial microfluidic device (OrganoPlate® Graft by MIMETAS). Its biomimetic potential was increased by using human brain-derived cell lines, such as HBEC-5i, to create well-structured vessels and sprouts. The platform supports the vascularization of spheroid based GBM model and was used to assess the extravasation of the NPs. Since the results confirmed the limited extravasation capability of these NPs (as observed by previous in vivo studies by the group), HMC3 cells extravasation was also assessed, confirming that microglia cells can migrate through the vessel towards the tumour mass, therefore confirming their potential as NPs carriers to GBM. The results confirmed the potential of this platform as a powerful tool to reliably validate *in vitro* new promising treatment strategies based on nanomedicine and cell transporters.

Future studies may further implement the spheroid models, e.g., by adding other cell lines, such as neurons, to allow a more inclusive study of the intercommunication between different cell lines. Moreover, different ECM-like gel matrixes, could be implemented to achieve a more biomimetic composition (i.e., by mixing hyaluronic acid and collagen) and further assess the role of ECM characteristics (e.g., mechanical properties) on the drug response.

Last, to achieve a more comprehensive GBM replica for nanomedicine screening, the microfluidic model could be further improved by including the other components of the BBB, such as astrocytes and pericytes.

This work provided fundamental insights both on the development of GBM models and their use as drug screening platforms and represents a promising starting point for further development and validation.

7 Bibliography

[1] M. Davis, "Glioblastoma: Overview of Disease and Treatment," *Clin J Oncol Nurs*, vol. 20, no. 5, pp. S2–S8, Oct. 2016, doi: 10.1188/16.CJON.S1.2-8.

[2] A. C. Tan, D. M. Ashley, G. Y. López, M. Malinzak, H. S. Friedman, and M. Khasraw, "Management of glioblastoma: State of the art and future directions," *CA Cancer J Clin*, vol. 70, no. 4, pp. 299–312, Jul. 2020, doi: 10.3322/caac.21613.

[3] D. N. Louis *et al.*, "The 2016 World Health Organization Classification of Tumors of the Central Nervous System: a summary," *Acta Neuropathol*, vol. 131, no. 6, pp. 803–820, Jun. 2016, doi: 10.1007/s00401-016-1545-1.

[4] K. Urbańska, J. Sokołowska, M. Szmidt, and P. Sysa, "Review Glioblastoma multiforme – an overview," *Współczesna Onkologia*, vol. 5, pp. 307–312, 2014, doi: 10.5114/wo.2014.40559.

[5] S. E. Lakhan and L. Harle, "Difficult diagnosis of brainstem glioblastoma multiforme in a woman: a case report and review of the literature," *J Med Case Rep*, vol. 3, no. 1, p. 87, Dec. 2009, doi: 10.1186/1752-1947-3-87.

[6] A. F. TAMIMI and M. JUWEID, "Epidemiology and Outcome of Glioblastoma," in *Glioblastoma*, Codon Publications, 2017, pp. 143–153. doi: 10.15586/codon.glioblastoma.2017.ch8.

[7] S. Grochans *et al.*, "Epidemiology of Glioblastoma Multiforme–Literature Review," *Cancers (Basel)*, vol. 14, no. 10, p. 2412, May 2022, doi: 10.3390/cancers14102412.

[8] W. Wu *et al.*, "Glioblastoma multiforme (GBM): An overview of current therapies and mechanisms of resistance," *Pharmacol Res*, vol. 171, p. 105780, Sep. 2021, doi: 10.1016/j.phrs.2021.105780.

[9] S. L. Perrin *et al.*, "Glioblastoma heterogeneity and the tumour microenvironment: implications for preclinical research and development of new treatments," *Biochem Soc Trans*, vol. 47, no. 2, pp. 625–638, Apr. 2019, doi: 10.1042/BST20180444.

[10] J. Bruns, T. Egan, P. Mercier, and S. P. Zustiak, "Glioblastoma spheroid growth and chemotherapeutic responses in single and dual-stiffness hydrogels," *Acta Biomater*, vol. 163, pp. 400–414, Jun. 2023, doi: 10.1016/j.actbio.2022.05.048.

[11] M. A. Qazi *et al.*, "Intratumoral heterogeneity: pathways to treatment resistance and relapse in human glioblastoma," *Annals of Oncology*, vol. 28, no. 7, pp. 1448–1456, Jul. 2017, doi: 10.1093/annonc/mdx169.

[12] H. Ohgaki and P. Kleihues, "The Definition of Primary and Secondary Glioblastoma," *Clinical Cancer Research*, vol. 19, no. 4, pp. 764–772, Feb. 2013, doi: 10.1158/1078-0432.CCR-12-3002.

[13] "Marked genomic differences characterize primary and secondary glioblastoma subtypes and identify two distinct molecular and clinical secondary glioblastoma entities. ".

[14] F. Liu *et al.*, "EGFR Mutation Promotes Glioblastoma through Epigenome and Transcription Factor Network Remodeling," *Mol Cell*, vol. 60, no. 2, pp. 307–318, Oct. 2015, doi: 10.1016/j.molcel.2015.09.002.

[15] N. Shinojima *et al.*, “Prognostic value of epidermal growth factor receptor in patients with glioblastoma multiforme.,” *Cancer Res*, vol. 63, no. 20, pp. 6962–70, Oct. 2003.

[16] C. Brennan *et al.*, “Glioblastoma subclasses can be defined by activity among signal transduction pathways and associated genomic alterations.,” *PLoS One*, vol. 4, no. 11, p. e7752, Nov. 2009, doi: 10.1371/journal.pone.0007752.

[17] Cancer Genome Atlas Research Network, “Comprehensive genomic characterization defines human glioblastoma genes and core pathways.,” *Nature*, vol. 455, no. 7216, pp. 1061–8, Oct. 2008, doi: 10.1038/nature07385.

[18] R. G. W. Verhaak *et al.*, “Integrated Genomic Analysis Identifies Clinically Relevant Subtypes of Glioblastoma Characterized by Abnormalities in PDGFRA, IDH1, EGFR, and NF1,” *Cancer Cell*, vol. 17, no. 1, pp. 98–110, Jan. 2010, doi: 10.1016/j.ccr.2009.12.020.

[19] T. Ozawa *et al.*, “*PDGFRA* gene rearrangements are frequent genetic events in *PDGFRA* -amplified glioblastomas,” *Genes Dev*, vol. 24, no. 19, pp. 2205–2218, Oct. 2010, doi: 10.1101/gad.1972310.

[20] K. L. Ligon *et al.*, “Olig2-regulated lineage-restricted pathway controls replication competence in neural stem cells and malignant glioma.,” *Neuron*, vol. 53, no. 4, pp. 503–17, Feb. 2007, doi: 10.1016/j.neuron.2007.01.009.

[21] A. O. Sasmita, Y. P. Wong, and A. P. K. Ling, “Biomarkers and therapeutic advances in glioblastoma multiforme,” *Asia Pac J Clin Oncol*, vol. 14, no. 1, pp. 40–51, Feb. 2018, doi: 10.1111/ajco.12756.

[22] K. Urbanska, J. Sokolowska, M. Szmidt, and P. Sysa, “Glioblastoma multiforme - An overview,” *Wspolczesna Onkologia*, vol. 18, no. 5. Termedia Publishing House Ltd., pp. 307–312, 2014. doi: 10.5114/wo.2014.40559.

[23] A. G. Linkous and E. M. Yazlovitskaya, “Angiogenesis in Glioblastoma Multiforme: Navigating the Maze,” *Anticancer Agents Med Chem*, vol. 11, no. 8, pp. 712–718, Oct. 2011, doi: 10.2174/187152011797378643.

[24] A. M. Rojiani and K. Dorovini-Zis, “Glomeruloid vascular structures in glioblastoma multiforme: an immunohistochemical and ultrastructural study,” *J Neurosurg*, vol. 85, no. 6, pp. 1078–1084, Dec. 1996, doi: 10.3171/jns.1996.85.6.1078.

[25] “Kleihues P, Burger PC, Collins VP, Cavenee WK. Pathology and genetics of tumours of the nervous system. IARC Press, Lyon 2000.”.

[26] D. J. Brat *et al.*, “Pseudopalisades in Glioblastoma Are Hypoxic, Express Extracellular Matrix Proteases, and Are Formed by an Actively Migrating Cell Population,” *Cancer Res*, vol. 64, no. 3, pp. 920–927, Feb. 2004, doi: 10.1158/0008-5472.CAN-03-2073.

[27] S. De Vleeschouwer and G. Bergers, *Glioblastoma: To Target the Tumor Cell or the Microenvironment?* 2017.

[28] W. Tomaszewski, L. Sanchez-Perez, T. F. Gajewski, and J. H. Sampson, “Brain Tumor Microenvironment and Host State: Implications for Immunotherapy.,” *Clin Cancer Res*, vol. 25, no. 14, pp. 4202–4210, Jul. 2019, doi: 10.1158/1078-0432.CCR-18-1627.

[29] A. D’Alessio, G. Proietti, G. Sica, and B. M. Scicchitano, “Pathological and Molecular Features of Glioblastoma and Its Peritumoral Tissue,” *Cancers (Basel)*, vol. 11, no. 4, p. 469, Apr. 2019, doi: 10.3390/cancers11040469.

[30] E. Codrici, I.-D. Popescu, C. Tanase, and A.-M. Enciu, “Friends with Benefits: Chemokines, Glioblastoma-Associated Microglia/Macrophages, and Tumor Microenvironment,” *Int J Mol Sci*, vol. 23, no. 5, p. 2509, Feb. 2022, doi: 10.3390/ijms23052509.

[31] H. E. de Vries, G. Kooij, D. Frenkel, S. Georgopoulos, A. Monsonego, and D. Janigro, “Inflammatory events at blood-brain barrier in neuroinflammatory and neurodegenerative disorders: implications for clinical disease.,” *Epilepsia*, vol. 53 Suppl 6, no. Suppl 6, pp. 45–52, Nov. 2012, doi: 10.1111/j.1528-1167.2012.03702.x.

[32] R. Glass and M. Synowitz, “CNS macrophages and peripheral myeloid cells in brain tumours,” *Acta Neuropathol*, vol. 128, no. 3, pp. 347–362, Sep. 2014, doi: 10.1007/s00401-014-1274-2.

[33] H. Grégoire *et al.*, “Targeting Tumor Associated Macrophages to Overcome Conventional Treatment Resistance in Glioblastoma,” *Front Pharmacol*, vol. 11, Apr. 2020, doi: 10.3389/fphar.2020.00368.

[34] M. Dapash, D. Hou, B. Castro, C. Lee-Chang, and M. S. Lesniak, “The Interplay between Glioblastoma and Its Microenvironment,” *Cells*, vol. 10, no. 9, p. 2257, Aug. 2021, doi: 10.3390/cells10092257.

[35] D. Schiffer, M. Mellai, E. Bovio, I. Bisogno, C. Casalone, and L. Annovazzi, “Glioblastoma niches: from the concept to the phenotypical reality,” *Neurological Sciences*, vol. 39, no. 7, pp. 1161–1168, Jul. 2018, doi: 10.1007/s10072-018-3408-0.

[36] D. Schiffer, L. Annovazzi, C. Casalone, C. Corona, and M. Mellai, “Glioblastoma: Microenvironment and Niche Concept,” *Cancers (Basel)*, vol. 11, no. 1, p. 5, Dec. 2018, doi: 10.3390/cancers11010005.

[37] D. Hambardzumyan and G. Bergers, “Glioblastoma: Defining Tumor Niches,” *Trends Cancer*, vol. 1, no. 4, pp. 252–265, Dec. 2015, doi: 10.1016/j.trecan.2015.10.009.

[38] S. Guelfi, H. Duffau, L. Bauchet, B. Rothhut, and J.-P. Hugnot, “Vascular Transdifferentiation in the CNS: A Focus on Neural and Glioblastoma Stem-Like Cells,” *Stem Cells Int*, vol. 2016, pp. 1–13, 2016, doi: 10.1155/2016/2759403.

[39] Y. Shi *et al.*, “Construction of a novel blood brain barrier-glioma microfluidic chip model: Applications in the evaluation of permeability and anti-glioma activity of traditional Chinese medicine components.,” *Talanta*, vol. 253, p. 123971, Feb. 2023, doi: 10.1016/j.talanta.2022.123971.

[40] Y. Wang *et al.*, “Remodelling and Treatment of the Blood-Brain Barrier in Glioma,” *Cancer Manag Res*, vol. Volume 13, pp. 4217–4232, May 2021, doi: 10.2147/CMAR.S288720.

[41] J. Guyon, C. Chapouly, L. Andrique, A. Bikfalvi, and T. Daubon, “The Normal and Brain Tumor Vasculature: Morphological and Functional Characteristics and Therapeutic Targeting,” *Front Physiol*, vol. 12, Mar. 2021, doi: 10.3389/fphys.2021.622615.

[42] C. D. Arvanitis, G. B. Ferraro, and R. K. Jain, “The blood–brain barrier and blood–tumour barrier in brain tumours and metastases,” *Nat Rev Cancer*, vol. 20, no. 1, pp. 26–41, Jan. 2020, doi: 10.1038/s41568-019-0205-x.

[43] J. R. Kane, “The Role of Brain Vasculature in Glioblastoma,” *Mol Neurobiol*, vol. 56, no. 9, pp. 6645–6653, Sep. 2019, doi: 10.1007/s12035-019-1561-y.

[44] L. G. Dubois *et al.*, “Gliomas and the vascular fragility of the blood brain barrier,” *Front Cell Neurosci*, vol. 8, Dec. 2014, doi: 10.3389/fncel.2014.00418.

[45] J. P. Straehla *et al.*, “A predictive microfluidic model of human glioblastoma to assess trafficking of blood–brain barrier-penetrant nanoparticles,” *Proceedings of the National Academy of Sciences*, vol. 119, no. 23, Jun. 2022, doi: 10.1073/pnas.2118697119.

[46] Enaya Mohiuddin and Hiroaki Wakimoto, “Extracellular matrix in glioblastoma: opportunities for emerging therapeutic approaches,” *Department of Neurosurgery, Massachusetts General Hospital, Harvard Medical School, Boston, MA 02114, USA*.

[47] A. C. Bellail, S. B. Hunter, D. J. Brat, C. Tan, and E. G. Van Meir, “Microregional extracellular matrix heterogeneity in brain modulates glioma cell invasion,” *Int J Biochem Cell Biol*, vol. 36, no. 6, pp. 1046–1069, Jun. 2004, doi: 10.1016/j.biocel.2004.01.013.

[48] A. C. Bellail, S. B. Hunter, D. J. Brat, C. Tan, and E. G. Van Meir, “Microregional extracellular matrix heterogeneity in brain modulates glioma cell invasion,” *Int J Biochem Cell Biol*, vol. 36, no. 6, pp. 1046–1069, Jun. 2004, doi: 10.1016/j.biocel.2004.01.013.

[49] V. P. Ferrer, V. Moura Neto, and R. Mentlein, “Glioma infiltration and extracellular matrix: key players and modulators,” *Glia*, vol. 66, no. 8, pp. 1542–1565, Aug. 2018, doi: 10.1002/glia.23309.

[50] H. Ruiz-Garcia, K. Alvarado-Estrada, P. Schiapparelli, A. Quinones-Hinojosa, and D. M. Trifiletti, “Engineering Three-Dimensional Tumor Models to Study Glioma Cancer Stem Cells and Tumor Microenvironment,” *Front Cell Neurosci*, vol. 14, Oct. 2020, doi: 10.3389/fncel.2020.558381.

[51] R. Sun and A. H. Kim, “The multifaceted mechanisms of malignant glioblastoma progression and clinical implications,” *Cancer and Metastasis Reviews*, vol. 41, no. 4, pp. 871–898, Dec. 2022, doi: 10.1007/s10555-022-10051-5.

[52] T. Mammoto, A. Jiang, E. Jiang, D. Panigrahy, M. W. Kieran, and A. Mammoto, “Role of Collagen Matrix in Tumor Angiogenesis and Glioblastoma Multiforme Progression,” *Am J Pathol*, vol. 183, no. 4, pp. 1293–1305, Oct. 2013, doi: 10.1016/j.ajpath.2013.06.026.

[53] T. A. Ulrich, E. M. de Juan Pardo, and S. Kumar, “The Mechanical Rigidity of the Extracellular Matrix Regulates the Structure, Motility, and Proliferation of Glioma Cells,” *Cancer Res*, vol. 69, no. 10, pp. 4167–4174, May 2009, doi: 10.1158/0008-5472.CAN-08-4859.

[54] R. Gómez-Oliva *et al.*, “Evolution of Experimental Models in the Study of Glioblastoma: Toward Finding Efficient Treatments,” *Front Oncol*, vol. 10, Jan. 2021, doi: 10.3389/fonc.2020.614295.

[55] F. L. Robertson, M.-A. Marqués-Torrejón, G. M. Morrison, and S. M. Pollard, “Experimental models and tools to tackle glioblastoma,” *Dis Model Mech*, vol. 12, no. 9, Sep. 2019, doi: 10.1242/dmm.040386.

[56] M. Paolillo, S. Comincini, and S. Schinelli, “In Vitro Glioblastoma Models: A Journey into the Third Dimension,” *Cancers (Basel)*, vol. 13, no. 10, p. 2449, May 2021, doi: 10.3390/cancers13102449.

[57] S. Caragher, A. J. Chalmers, and N. Gomez-Roman, “Glioblastoma’s Next Top Model: Novel Culture Systems for Brain Cancer Radiotherapy Research.,” *Cancers (Basel)*, vol. 11, no. 1, Jan. 2019, doi: 10.3390/cancers11010044.

[58] B. H. Rath, J. M. Fair, M. Jamal, K. Camphausen, and P. J. Tofilon, “Astrocytes Enhance the Invasion Potential of Glioblastoma Stem-Like Cells,” *PLoS One*, vol. 8, no. 1, p. e54752, Jan. 2013, doi: 10.1371/journal.pone.0054752.

[59] E. M. Galan-Moya *et al.*, “Secreted factors from brain endothelial cells maintain glioblastoma stem-like cell expansion through the mTOR pathway,” *EMBO Rep*, vol. 12, no. 5, pp. 470–476, May 2011, doi: 10.1038/embor.2011.39.

[60] D. M. Leite, B. Zvar Baskovic, P. Civita, C. Neto, M. Gumbleton, and G. J. Pilkington, “A human co-culture cell model incorporating microglia supports glioblastoma growth and migration, and confers resistance to cytotoxics.,” *FASEB J*, vol. 34, no. 1, pp. 1710–1727, Jan. 2020, doi: 10.1096/fj.201901858RR.

[61] W. Chen *et al.*, “Glioma cells escaped from cytotoxicity of temozolomide and vincristine by communicating with human astrocytes,” *Medical Oncology*, vol. 32, no. 3, p. 43, Mar. 2015, doi: 10.1007/s12032-015-0487-0.

[62] R. Gómez-Oliva *et al.*, “Evolution of Experimental Models in the Study of Glioblastoma: Toward Finding Efficient Treatments,” *Front Oncol*, vol. 10, Jan. 2021, doi: 10.3389/fonc.2020.614295.

[63] J. D. Lathia, S. C. Mack, E. E. Mulkearns-Hubert, C. L. L. Valentim, and J. N. Rich, “Cancer stem cells in glioblastoma,” *Genes Dev*, vol. 29, no. 12, pp. 1203–1217, Jun. 2015, doi: 10.1101/gad.261982.115.

[64] A. Torsvik *et al.*, “U-251 revisited: genetic drift and phenotypic consequences of long-term cultures of glioblastoma cells,” *Cancer Med*, vol. 3, no. 4, pp. 812–824, Aug. 2014, doi: 10.1002/cam4.219.

[65] M. Paolillo, S. Comincini, and S. Schinelli, “In Vitro Glioblastoma Models: A Journey into the Third Dimension.,” *Cancers (Basel)*, vol. 13, no. 10, May 2021, doi: 10.3390/cancers13102449.

[66] L.-B. Weiswald, D. Bellet, and V. Dangles-Marie, “Spherical Cancer Models in Tumor Biology,” *Neoplasia*, vol. 17, no. 1, pp. 1–15, Jan. 2015, doi: 10.1016/j.neo.2014.12.004.

[67] S. ZHANG, R. XIE, F. WAN, F. YE, D. GUO, and T. LEI, “Identification of U251 glioma stem cells and their heterogeneous stem-like phenotypes,” *Oncol Lett*, vol. 6, no. 6, pp. 1649–1655, Dec. 2013, doi: 10.3892/ol.2013.1623.

[68] L.-B. Weiswald, D. Bellet, and V. Dangles-Marie, “Spherical Cancer Models in Tumor Biology,” *Neoplasia*, vol. 17, no. 1, pp. 1–15, Jan. 2015, doi: 10.1016/j.neo.2014.12.004.

[69] T. Stanković *et al.*, “In vitro biomimetic models for glioblastoma-a promising tool for drug response studies,” *Drug Resistance Updates*, vol. 55, p. 100753, Mar. 2021, doi: 10.1016/j.drup.2021.100753.

[70] J. M. Kelm, N. E. Timmins, C. J. Brown, M. Fussenegger, and L. K. Nielsen, “Method for generation of homogeneous multicellular tumor spheroids applicable to a wide variety of cell types,” *Biotechnol Bioeng*, vol. 83, no. 2, pp. 173–180, Jul. 2003, doi: 10.1002/bit.10655.

[71] T. Stanković *et al.*, “In vitro biomimetic models for glioblastoma-a promising tool for drug response studies,” *Drug Resistance Updates*, vol. 55, p. 100753, Mar. 2021, doi: 10.1016/j.drup.2021.100753.

[72] T. Stanković *et al.*, “In vitro biomimetic models for glioblastoma-a promising tool for drug response studies,” *Drug Resistance Updates*, vol. 55, p. 100753, Mar. 2021, doi: 10.1016/j.drup.2021.100753.

[73] E. C. Costa, D. de Melo-Diogo, A. F. Moreira, M. P. Carvalho, and I. J. Correia, “Spheroids Formation on Non-Adhesive Surfaces by Liquid Overlay Technique: Considerations and Practical Approaches,” *Biotechnol J*, vol. 13, no. 1, p. 1700417, Jan. 2018, doi: 10.1002/biot.201700417.

[74] A. Yilmazer, “Evaluation of cancer stemness in breast cancer and glioblastoma spheroids in vitro,” *3 Biotech*, vol. 8, no. 9, p. 390, Sep. 2018, doi: 10.1007/s13205-018-1412-y.

[75] P. S. Nakod, Y. Kim, and S. S. Rao, “The Impact of Astrocytes and Endothelial Cells on Glioblastoma Stemness Marker Expression in Multicellular Spheroids,” *Cell Mol Bioeng*, vol. 14, no. 6, pp. 639–651, Dec. 2021, doi: 10.1007/s12195-021-00691-y.

[76] T. Morimoto *et al.*, “Evaluation of Comprehensive Gene Expression and NK Cell-Mediated Killing in Glioblastoma Cell Line-Derived Spheroids,” *Cancers (Basel)*, vol. 13, no. 19, p. 4896, Sep. 2021, doi: 10.3390/cancers13194896.

[77] P. Longati *et al.*, “3D pancreatic carcinoma spheroids induce a matrix-rich, chemoresistant phenotype offering a better model for drug testing.,” *BMC Cancer*, vol. 13, p. 95, Feb. 2013, doi: 10.1186/1471-2407-13-95.

[78] B. Huang *et al.*, “CCL2/CCR2 pathway mediates recruitment of myeloid suppressor cells to cancers.,” *Cancer Lett*, vol. 252, no. 1, pp. 86–92, Jul. 2007, doi: 10.1016/j.canlet.2006.12.012.

[79] C. Sarisozen, S. Dhokai, E. G. Tsikudo, E. Luther, I. M. Rachman, and V. P. Torchilin, “Nanomedicine based curcumin and doxorubicin combination treatment of glioblastoma with scFv-targeted micelles: In vitro evaluation on 2D and 3D tumor models,” *European Journal of Pharmaceutics and Biopharmaceutics*, vol. 108, pp. 54–67, Nov. 2016, doi: 10.1016/j.ejpb.2016.08.013.

[80] C. Sarisozen, A. H. Abouzeid, and V. P. Torchilin, “The effect of co-delivery of paclitaxel and curcumin by transferrin-targeted PEG-PE-based mixed micelles on resistant ovarian cancer in 3-D spheroids and in vivo tumors,” *European Journal of Pharmaceutics and Biopharmaceutics*, vol. 88, no. 2, pp. 539–550, Oct. 2014, doi: 10.1016/j.ejpb.2014.07.001.

[81] A. S. Nunes, A. S. Barros, E. C. Costa, A. F. Moreira, and I. J. Correia, "3D tumor spheroids as in vitro models to mimic in vivo human solid tumors resistance to therapeutic drugs," *Biotechnol Bioeng*, vol. 116, no. 1, pp. 206–226, Jan. 2019, doi: 10.1002/bit.26845.

[82] P. C. De Witt Hamer *et al.*, "The genomic profile of human malignant glioma is altered early in primary cell culture and preserved in spheroids," *Oncogene*, vol. 27, no. 14, pp. 2091–2096, Mar. 2008, doi: 10.1038/sj.onc.1210850.

[83] A. Kamatar, G. Gunay, and H. Acar, "Natural and synthetic biomaterials for engineering multicellular tumor spheroids," *Polymers*, vol. 12, no. 11. MDPI AG, pp. 1–23, Nov. 01, 2020. doi: 10.3390/polym12112506.

[84] J.-C. Kuo, "Focal adhesions function as a mechanosensor.," *Prog Mol Biol Transl Sci*, vol. 126, pp. 55–73, 2014, doi: 10.1016/B978-0-12-394624-9.00003-8.

[85] S. S. Rao, J. J. Lannutti, M. S. Viapiano, A. Sarkar, and J. O. Winter, "Toward 3D Biomimetic Models to Understand the Behavior of Glioblastoma Multiforme Cells," *Tissue Eng Part B Rev*, vol. 20, no. 4, pp. 314–327, Aug. 2014, doi: 10.1089/ten.teb.2013.0227.

[86] H. M. Micek, M. R. Visetsouk, K. S. Masters, and P. K. Kreeger, "Engineering the Extracellular Matrix to Model the Evolving Tumor Microenvironment," *iScience*, vol. 23, no. 11, p. 101742, Nov. 2020, doi: 10.1016/j.isci.2020.101742.

[87] I. M. El-Sherbiny and M. H. Yacoub, "Hydrogel scaffolds for tissue engineering: Progress and challenges," *Glob Cardiol Sci Pract*, vol. 2013, no. 3, p. 38, Sep. 2013, doi: 10.5339/gcsp.2013.38.

[88] F. Pampaloni, E. G. Reynaud, and E. H. K. Stelzer, "The third dimension bridges the gap between cell culture and live tissue," *Nat Rev Mol Cell Biol*, vol. 8, no. 10, pp. 839–845, Oct. 2007, doi: 10.1038/nrm2236.

[89] D. Lv *et al.*, "A three-dimensional collagen scaffold cell culture system for screening anti-glioma therapeutics," *Oncotarget*, vol. 7, no. 35, pp. 56904–56914, Aug. 2016, doi: 10.18632/oncotarget.10885.

[90] D. Zhu, P. Trinh, J. Li, G. A. Grant, and F. Yang, "Gradient hydrogels for screening stiffness effects on patient-derived glioblastoma xenograft cellfates in <scp>3D</scp>," *J Biomed Mater Res A*, vol. 109, no. 6, pp. 1027–1035, Jun. 2021, doi: 10.1002/jbm.a.37093.

[91] L. Hill, J. Bruns, and S. P. Zustiak, "Hydrogel matrix presence and composition influence drug responses of encapsulated glioblastoma spheroids," *Acta Biomater*, vol. 132, pp. 437–447, Sep. 2021, doi: 10.1016/j.actbio.2021.05.005.

[92] D. Caballero, S. Kaushik, V. M. Correlo, J. M. Oliveira, R. L. Reis, and S. C. Kundu, "Organ-on-chip models of cancer metastasis for future personalized medicine: From chip to the patient," *Biomaterials*, vol. 149, pp. 98–115, Dec. 2017, doi: 10.1016/j.biomaterials.2017.10.005.

[93] J. P. Straehla *et al.*, "A predictive microfluidic model of human glioblastoma to assess trafficking of blood–brain barrier-penetrant nanoparticles," *Proceedings of the National Academy of Sciences*, vol. 119, no. 23, Jun. 2022, doi: 10.1073/pnas.2118697119.

[94] X. Cai *et al.*, “Application of microfluidic devices for glioblastoma study: current status and future directions,” *Biomed Microdevices*, vol. 22, no. 3, p. 60, Sep. 2020, doi: 10.1007/s10544-020-00516-1.

[95] S. Seo, S. Nah, K. Lee, N. Choi, and H. N. Kim, “Triculture Model of In Vitro BBB and its Application to Study BBB-Associated Chemosensitivity and Drug Delivery in Glioblastoma,” *Adv Funct Mater*, vol. 32, no. 10, p. 2106860, Mar. 2022, doi: 10.1002/adfm.202106860.

[96] L. I. Kobylinska *et al.*, “Differential pro-apoptotic effects of synthetic 4-thiazolidinone derivative Les-3288, doxorubicin and temozolomide in human glioma U251 cells.,” *Croat Med J*, vol. 58, no. 2, pp. 150–159, Apr. 2017, doi: 10.3325/cmj.2017.58.150.

[97] D. Wu, Q. Chen, X. Chen, F. Han, Z. Chen, and Y. Wang, “The blood–brain barrier: structure, regulation, and drug delivery,” *Signal Transduct Target Ther*, vol. 8, no. 1, p. 217, May 2023, doi: 10.1038/s41392-023-01481-w.

[98] M. Farshbaf *et al.*, “Enhanced BBB and BBTB penetration and improved anti-glioma behavior of Bortezomib through dual-targeting nanostructured lipid carriers,” *Journal of Controlled Release*, vol. 345, pp. 371–384, May 2022, doi: 10.1016/j.jconrel.2022.03.019.

[99] C. Mattu *et al.*, “Alternating block copolymer-based nanoparticles as tools to modulate the loading of multiple chemotherapeutics and imaging probes,” *Acta Biomater*, vol. 80, pp. 341–351, Oct. 2018, doi: 10.1016/j.actbio.2018.09.021.

[100] D. Kalyane, N. Raval, R. Maheshwari, V. Tambe, K. Kalia, and R. K. Tekade, “Employment of enhanced permeability and retention effect (EPR): Nanoparticle-based precision tools for targeting of therapeutic and diagnostic agent in cancer,” *Materials Science and Engineering: C*, vol. 98, pp. 1252–1276, May 2019, doi: 10.1016/j.msec.2019.01.066.

[101] D. Hambardzumyan, D. H. Gutmann, and H. Kettenmann, “The role of microglia and macrophages in glioma maintenance and progression,” *Nat Neurosci*, vol. 19, no. 1, pp. 20–27, Jan. 2016, doi: 10.1038/nn.4185.

[102] S. J. Sundar, J. K. Hsieh, S. Manjila, J. D. Lathia, and A. Sloan, “The role of cancer stem cells in glioblastoma,” *Neurosurg Focus*, vol. 37, no. 6, p. E6, Dec. 2014, doi: 10.3171/2014.9.FOCUS14494.

[103] K. Kitamura *et al.*, “Human Immortalized Cell-Based Blood–Brain Barrier Spheroid Models Offer an Evaluation Tool for the Brain Penetration Properties of Macromolecules,” *Mol Pharm*, vol. 19, no. 8, pp. 2754–2764, Aug. 2022, doi: 10.1021/acs.molpharmaceut.2c00120.

[104] A. S. Abreu, E. M. Castanheira, M.-J. R. Queiroz, P. M. Ferreira, L. A. Vale-Silva, and E. Pinto, “Nanoliposomes for encapsulation and delivery of the potential antitumoral methyl 6-methoxy-3-(4-methoxyphenyl)-1H-indole-2-carboxylate,” *Nanoscale Res Lett*, vol. 6, no. 1, p. 482, Dec. 2011, doi: 10.1186/1556-276X-6-482.

[105] I. Pochard, J.-P. Boisvert, J. Persello, and A. Foissy, “Surface charge, effective charge and dispersion/aggregation properties of nanoparticles,” *Polym Int*, vol. 52, no. 4, pp. 619–624, Apr. 2003, doi: 10.1002/pi.1008.

[106] J. D. Clogston and A. K. Patri, “Zeta Potential Measurement,” 2011, pp. 63–70. doi: 10.1007/978-1-60327-198-1_6.

[107] S. Rani, R. K. Sahoo, K. T. Nakhate, Ajazuddin, and U. Gupta, “Biotinylated HPMA centered polymeric nanoparticles for Bortezomib delivery,” *Int J Pharm*, vol. 579, p. 119173, Apr. 2020, doi: 10.1016/j.ijpharm.2020.119173.

[108] D. M. Leite, B. Zvar Baskovic, P. Civita, C. Neto, M. Gumbleton, and G. J. Pilkington, “A human co-culture cell model incorporating microglia supports glioblastoma growth and migration, and confers resistance to cytotoxics,” *The FASEB Journal*, vol. 34, no. 1, pp. 1710–1727, Jan. 2020, doi: 10.1096/fj.201901858RR.

[109] H. Kang *et al.*, “Targeting Glioblastoma Stem Cells to Overcome Chemoresistance: An Overview of Current Therapeutic Strategies,” *Biomedicines*, vol. 10, no. 6, p. 1308, Jun. 2022, doi: 10.3390/biomedicines10061308.

[110] J.-W. E. Chen *et al.*, “Crosstalk between microglia and patient-derived glioblastoma cells inhibit invasion in a three-dimensional gelatin hydrogel model,” *J Neuroinflammation*, vol. 17, no. 1, p. 346, Dec. 2020, doi: 10.1186/s12974-020-02026-6.

[111] G. Stojkov, Z. Niyazov, F. Picchioni, and R. K. Bose, “Relationship between Structure and Rheology of Hydrogels for Various Applications,” *Gels*, vol. 7, no. 4, p. 255, Dec. 2021, doi: 10.3390/gels7040255.

[112] A. Buonfiglioli and D. Hambardzumyan, “Macrophages and microglia: the cerberus of glioblastoma,” *Acta Neuropathol Commun*, vol. 9, no. 1, p. 54, Mar. 2021, doi: 10.1186/s40478-021-01156-z.

[113] C. Brignole *et al.*, “Effect of Bortezomib on Human Neuroblastoma Cell Growth, Apoptosis, and Angiogenesis,” *JNCI: Journal of the National Cancer Institute*, vol. 98, no. 16, pp. 1142–1157, Aug. 2006, doi: 10.1093/jnci/djj309.

[114] S. J. Coniglio and J. E. Segall, “Review: Molecular mechanism of microglia stimulated glioblastoma invasion,” *Matrix Biology*, vol. 32, no. 7–8, pp. 372–380, Oct. 2013, doi: 10.1016/j.matbio.2013.07.008.

[115] C. Huang, P. J. Butler, S. Tong, H. S. Muddana, G. Bao, and S. Zhang, “Substrate Stiffness Regulates Cellular Uptake of Nanoparticles,” *Nano Lett*, vol. 13, no. 4, pp. 1611–1615, Apr. 2013, doi: 10.1021/nl400033h.

[116] I. R. Calori, S. R. Alves, H. Bi, and A. C. Tedesco, “Type-I Collagen/Collagenase Modulates the 3D Structure and Behavior of Glioblastoma Spheroid Models,” *ACS Appl Bio Mater*, vol. 5, no. 2, pp. 723–733, Feb. 2022, doi: 10.1021/acsabm.1c01138.

[117] B. Obermeier, R. Daneman, and R. M. Ransohoff, “Development, maintenance and disruption of the blood-brain barrier,” *Nat Med*, vol. 19, no. 12, pp. 1584–1596, Dec. 2013, doi: 10.1038/nm.3407.

[118] Z. Zhang, Q. Gan, J. Han, Q. Tao, W. Q. Qiu, and J. A. Madri, “CD31 as a probable responding and gate-keeping protein of the blood-brain barrier and the risk of Alzheimer’s disease,” *Journal of Cerebral Blood Flow & Metabolism*, vol. 43, no. 7, pp. 1027–1041, Jul. 2023, doi: 10.1177/0271678X231170041.

[119] B. Nico *et al.*, “Developmental expression of ZO-1 antigen in the mouse blood–brain barrier,” *Developmental Brain Research*, vol. 114, no. 2, pp. 161–169, May 1999, doi: 10.1016/S0165-3806(99)00008-5.

[120] J. Li and C. Sabliov, “PLA/PLGA nanoparticles for delivery of drugs across the blood-brain barrier,” *Nanotechnol Rev*, vol. 2, no. 3, pp. 241–257, Jun. 2013, doi: 10.1515/ntrev-2012-0084.